UNIVERSIDAD
POLITECNICA
DE VALENCIA

Design and Implementation of Photonic Metamaterials

Carlos García Meca

Supervisor: Alejandro J. Martínez Abiétar

Doctoral thesis

submitted for the degree of
Doctor of Philosophy in Telecommunication Engineering

Valencia, March 2012

Acknowledgements

Quiero dedicar mi más sincero agradecimiento a toda mi familia y amigos. En especial, a mis padres, mi hermana, mi tía Isabel María y mis abuelos Isabel y Pedro, quien siempre fue un gran entusiasta de la ciencia y me enseñó, entre otras cosas, a escribir mis primeras palabras. Todos ellos han marcado profundamente mi forma de ser, transmitiéndome unos valores y principios de los cuales me siento enormemente orgulloso y que espero me guíen durante el resto de mi vida.

Finalmente, gracias Reme por iluminar mi vida y por ayudarme siempre dentro y fuera de lo profesional. Eres puro arte.

Resumen

LOS METAMATERIALES son una nueva clase de materiales artificiales que pueden ser diseñados para poseer propiedades que serían difíciles o imposibles de encontrar en la naturaleza. Los metamateriales han posibilitado la aparición de un gran número de nuevos dispositivos fotónicos con asombrosas propiedades. Entre ellos, cabe destacar a los medios de índice negativo (NIMs), con los que es posible construir superlentes carentes del límite de resolución de las lentes convencionales, así como los dispositivos basados en óptica de transformación, una nueva teoría del electromagnetismo que permite conocer las propiedades que un medio debe tener para curvar o distorsionar el espacio electromagnético. Como consecuencia, ha sido posible crear dispositivos fascinantes, tales como capas de invisibilidad o agujeros negros ópticos. Debido a su importancia, en esta tesis nos hemos centrado en estas dos aplicaciones de los metamateriales.

En el caso de los medios de índice negativo, hemos estudiado cómo éstos pueden ser construidos a partir de estructuras de transmisión extraordinaria. Como resultado principal, se ha diseñado y verificado experimentalmente un novedoso metamaterial de altas prestaciones que presenta una elevada figura de mérito (sustancialmente mayor que las de trabajos previos) en el espectro visible. La estructura también presenta independencia de polarización y propiedades homogéneas para incidencia normal. Esta demostración corresponde al primer NIM experimental con bajas pérdidas en el régimen visible y también al primero formado por varias celdas unidad en la dirección de propagación, un paso importante hacia NIMs homogéneos en esta banda. Este trabajo ha sido reconocido como uno de los últimos hitos en metamateriales ópticos tridimensionales. Además, otros autores han demostrado que las propiedades de nuestra estructura pueden ser empleadas para controlar la velocidad de propagación (subluminal y superluminal) de pulsos laser de femtosegundos o para conseguir conmutación óptica con velocidades del orden de terabits por segundo.

En otra línea, hemos introducido el concepto de seguridad óptica basado en magnetismo artificial fuerte en este rango espectral. Esta exótica propiedad podría actuar como una firma óptica exclusiva que puede ser identificada fácilmente a partir de medidas adecuadas, y reproducible solamente con las técnicas de fabricación más avanzadas, añadiendo así un mayor nivel de seguridad y reduciendo enormemente la posibilidad de falsificación.

Además, hemos diseñado estructuras con respuestas magnéticas excepcionalmente elevadas en este rango, que encajan perfectamente con el perfíl de etiqueta de seguridad deseado. A diferencia de la mayoría de aplicaciones basadas en metamateriales, la seguridad óptica podría llegar a ser una aplicación real y alcanzar el mercado a corto plazo, ya que las técnicas de fabricación requeridas son comparativamente menos exigentes.

En cuanto a la óptica de transformación, hemos trabajado en el desarrollo y aplicación de metodologías de diseño que simplifiquen los parámetros constitutivos requeridos para la implementación de "medios de transformación", y que por tanto faciliten las etapas de diseño y fabricación de los metamateriales requeridos para sintetizar dispositivos basados en óptica de transformación. En este sentido, hemos seguido dos enfoques distintos. El primero ha consistido en la minimización de la anisotropía que aparece al realizar una transmutación de singularidades en ciertos elementos ópticos. Para ello nos hemos basado en la idea de transmutación parcial, la cual suprime la necesidad de utilizar elementos resonantes para su implementación. Esto podría convertir en realidad dispositivos de alto impacto, como capas de invisibilidad de gran ancho de banda, que de otra forma serían muy difíciles de conseguir. Por otro lado, hemos aplicado el concepto de mapeo quasi-conforme para conseguir diseñar dispositivos tecnológicamente realizables, tales como compresores ópticos isotrópicos y elementos capaces de conseguir diagramas de radiación complejos a partir de una fuente omnidireccional de forma sencilla.

Finalmente, hemos estudiado en profundidad algunos aspectos teóricos de la óptica de transformación. Dicho estudio nos ha permitido desarrollar dispositivos de gran interés, que podrían encontrar aplicación en procesado de alta velocidad y redes de comunicaciones. Entre ellos encontramos acopladores ultracompactos para guías nanofotónicas de alto índice, híperlentes planas sin reflexiones, acopladores para guías metálicas con diferente sección transversal y dispositivos capaces de acoplar luz a plasmones superficiales confinados en superficies metálicas sin estructurar, con anchos de banda angulares considerablemente mayores que los de acopladores convencionales.

Resum

ELS METAMATERIALS són una nova classe de materials artificials que poden ser dissenyats per a posseir propietats que serien difícils o impossibles de trobar en la naturalesa. Els meta-materiales han portat amb si un gran nombre de nous dispositius amb sorprenents propietats. Entre ells, cal destacar als medis d'índex negatiu (NIMs), amb els que és possible construir su-perlents faltats del límit de resolució de les lents convencionals, així com els dispositius basats en òptica de transformació, una nova teoria de l'electromagnetisme que permet conéixer les propietats que un medi ha de tindre per a corbar o distorsionar l'espai electromagnètic. Com a conseqüència, ha sigut possible crear dispositius fascinants, tals com capes d'invisibilitat o forats negres òptics. A causa de la seua importància, en esta tesi ens hem centrat en estes dos aplicacions dels metamaterials.

En el cas dels medis d'índex negatiu, hem estudiat com estos poden ser construïts a partir d'estructures de transmissió extraordinària. Com resultat principal, s'ha dissenyat i verificat experimentalment un nou metamaterial d'altes prestacions que presenta una elevada figura de mèrit (substancialment major que les de treballs previs) en l'espectre visible. L'estructura també presenta independència de polarització i propietats homogènies per a incidència nor-mal. Esta demostració correspon al primer NIM experimental amb baixes pèrdues en el règim visible i també al primer format per diverses cel·les unitat en la direcció de propagació, un pas important cap a NIMs homogenis en esta banda. Este treball ha sigut reconegut com unes de les últimes fites en metamaterials òptics tridimensionals. A més, altres autors han demostrat que les propietats de la nostra estructura poden ser empleades per a controlar la velocitat de propagació (subluminal i superluminal) de polsos làser de femtosegons o per a aconseguir commutació óptica amb velocitats de l'orde de terabits per segon.

En una altra línia, hem introduït el concepte de seguretat óptica basat en magnetisme artificial fort a freqüències òptiques. Esta exòtica propietat podria actuar com una firma òptica exclusiva que pot ser identificada fàcilment a partir de les mesures adequades, i reproduïble només amb les tècniques de fabricació més avançades, afegint per tant un major nivell de seguretat i reduint enormement la possibilitat de falsificació. A més, hem proposat estructures adequades per a este propòsit amb respostes magnètiques excepcionalment elevades en este rang, que encaixen perfectament amb el perfil d'etiqueta de seguretat desitjat.

A diferència de la majoria d'aplicacions basades en metamaterials, la seguretat òptica podria arribar a ser una aplicació real i abastar el mercat a curt termini, ja que les tècniques de fabricació requerides són comparativament menys exigents.

Quant a l'òptica de transformació, hem treballat en el desenrotllament i aplicació de metodologies de disseny que simplifiquen els paràmetres constitutius requerits per a la implementació de "medis de transformació", i que per tant faciliten les etapes de disseny i fabricació dels metamaterials requerits per a sintetitzar dispositius basats en òptica de transformació. En este sentit, hem seguit dos enfocaments distints. El primer consistix en la minimització de l'anisotropia que resulta de la transmutació de singularitats d'elements òptics. Per a això ens hem basat en la idea de transmutació parcial, la qual suprimix la necessitat d'utilitzar elements ressonants per a la seua implementació. Açò podria fer realitat dispositius d'alt impacte, com a capes d'invisibilitat de gran ample de banda, que d'una altra forma serien molt difícils d'aconseguir. D'altra banda, hem aplicat el concepte de mapatge quasi-conforme en el disseny de dispositius realitzables, tals com compressors óptics isótrops i dispositius capaços d'aconseguir diagrames de radiació complexos a partir d'una font omnidireccional de forma senzilla.

Finalment, hem estudiat en profunditat alguns aspectes teòrics de l'òptica de transformació. El citat estudi ens ha permés desenrotllar dispositius de gran interés que podrien trobar aplicació en processat d'alta velocitat i xàrcia de comunicacions. Estos inclouen acobladors ultracompactes per a guies nanofotòniques d'alt índex, hiperlentes planes sense reflexions, acobladors per a guies metàl·liques amb diferent secció transversal i dispositius capaços d'adaptar llum a plasmons superficials confinats en superfícies metàl·liques sense estructurar, amb amples de banda angulars considerablement majors que els dels acobladors convencionals.

Abstract

METAMATERIALS are a new class of artificial materials that can be engineered to possess properties that would be difficult or even impossible to find in nature. Metamaterials have brought about the advent of a great number of new photonic devices with amazing properties. Two of the most important ones are negative index media (NIMs), with which it is possible to build superlenses whose resolution is not limited by diffraction unlike in conventional lenses, and the devices based on transformation optics, a new theory within electromagnetism that allows us to know the properties that a medium should have in order to curve or distort electromagnetic space. As a consequence, it has been possible to create astonishing devices such as invisibility cloaks and optical black holes. Due to their importance, in this work we have focused on these two applications of metamaterials.

In the case of negative index media, we have studied how these can be built upon extraordinary transmission structures. As a main outcome, a novel multilayer high-performance NIM metamaterial exhibiting a high figure of merit (significantly larger than those of previous works) in the visible spectrum has been designed and experimentally verified. The structure also presents polarization independence and homogeneous properties for normal incidence. This demonstration entails the first experimental low-loss NIM in the visible regime and also the first one made up of several unit cells along the propagation direction, an important step towards homogeneous NIMs in this band. This work has been recognized as one of the latest milestones in three-dimensional optical metamaterials. Moreover, it has been shown by other authors that the properties of this structure can be employed to control the propagation velocity (subluminal and superluminal) of a femtosecond laser pulse or to achieve subpicosecond optical switching.

Along other line, we have introduced the concept of optical security based on strong artificial magnetism at optical frequencies. This exotic property could act as an exclusive optical fingerprint that can be easily identified from proper measurements and only reproducible with the most advanced nanofabrication techniques, thus adding a higher level of security and enormously reducing the possibility of counterfeiting. Suitable structures displaying unusually high magnetic responses in this regime have been proposed as well.

Unlike the majority of applications based on metamaterials, optical security could become a real application and reach the market in the short-term, since the required fabrication techniques would be comparatively less demanding.

Concerning transformation optics, we have worked on the development and application of design methodologies that simplify the constitutive parameters required for the implementation of transformation media, and thus facilitate the design and fabrication stages of the metamaterials needed to synthesize transformation-optics-based devices. In this sense, we have followed two different approaches. The first consists on the minimization of the anisotropy resulting from the transmutation of singularities of optical elements based on the idea of partial transmutation, which eliminates the need for resonant elements in their implementation. This could turn into reality interesting devices such as broadband invisibility cloaks, which otherwise would be difficult to realize. On the other hand, we have applied the concept of quasi-conformal mapping to design realizable devices, such as isotropic optical squeezers and radiation-pattern-shaping devices that allow us to achieve complex patterns in a simple way.

Finally, we have studied in depth some aspects of the theory of transformation optics and developed interesting devices from it, which could find application in the field of high-speed processing and networking. These include ultra-short perfect couplers for high-index nanophotonic waveguides, completely flat reflectionless hyperlenses, couplers for metallic waveguides with different cross-section and devices that couple free-space light to surface plasmon polaritons along non-patterned metallic surfaces with angular bandwidths considerably higher than those of conventional couplers.

Contents

Introduction and objectives

METAMATERIALS are a relatively new class of man-made electromagnetic materials (the concept was later extended to other fields of physics) that appeared approximately a decade ago. As opposed to photonic crystals,[1] which are based on the phenomenon of diffraction and whose crystalline structure has a periodicity comparable to the wavelength of light, metamaterials can be regarded as effective media characterized by specific electric permittivity and permeability constants (the constitutive parameters), since their lattice constant is much smaller than the wavelength. A huge advantage of these artificially-structured composites is that, in addition to their chemical composition, they owe their properties to the shape and dimensions of their constituent elements. As a consequence, they can be engineered to possess properties that would be difficult or even impossible to find in nature. This is the reason why they have been termed metamaterials. These meta-media have brought about a myriad of new devices with amazing properties and are shaping up as a new paradigm in the design of electromagnetic structures.

The development and impact of metamaterials have been enormous in the last few years. Good evidence of this is the huge amount of published scientific articles related to metamaterials. To a large extent, this is due to the following two scientific findings:

- The discovery in 2000 of the resolving power of negative-refractive-index lenses,[2] whose resolution is not limited by diffraction unlike in classical lenses. The so-called *superlenses* were rated as one of the breakthroughs of the year 2003 by the journal *Science*.[3] The discovery is due to sir John B. Pendry,

whose paper on the superlens had been cited around 4000 times by the time this thesis was written.[2]

- The development of a new theory within electromagnetism known as transformation optics.[4,5] This beautiful geometric reinterpretation of Maxwell's equations provides a way to know the properties that a medium should have in order curve or distort the space *seen* by light, allowing us to create astonishing devices such as invisibility cloaks and to realize experimental gravity analogs such as the event horizon of a black/white hole or an optical attractor.[6,7,8] Transformation optics, along with metamaterials, was the only topic of physics and engineering included by *Science* in its list of "insights of the decade" corresponding to the first decade of the third millennium.[9]

  Both negative index media (NIMs) and the devices designed via transformation optics require for their implementation exotic materials with constitutive parameters that are usually not found in nature. Although metamaterials provide a solution, it is often a challenge to achieve structures with the required properties. In this sense, the work of this thesis has been aimed at eliminating some of these difficulties in two different ways

- Designing and implementing novel metamaterials with which to synthesize NIMs in the visible spectrum with improved properties such as low-loss, polarization independence, and homogeneous behavior. Due to the superlensing ability of NIMs, achieving structures with this properties would be essential for applications in many fields such as microscopy, microelectronics, bio- and nano-technology. At the same time, these objectives pose some of the biggest challenges in this field.

- By developing and applying design methodologies that simplify the constitutive parameters required for the implementation of transformation media, and thus facilitate the design and fabrication stages of the metamaterials needed to synthesize transformation-optics-based devices.

  Finally, we have studied in depth some aspects of the theory of transformation optics and developed interesting devices

from it, which could find application in the field of high-speed processing and networking.

The thesis is organized as a collection of papers so that we only briefly mention in the main text the chief results or ideas developed in each paper. Nonetheless, the necessary background is introduced as needed, linking it with the work contained in each paper. The sections or subsections in which we directly talk about the original work of a paper are usually tagged as "our contribution". The work has been divided into four chapters. The first one is about metamaterials, where the main concepts are introduced. The core of the work is developed in chapters 2 and 3. Chapter 2 deals with negative index media and strong magnetism in the visible spectrum, and chapter 3 describes our work on transformation optics. Lastly, we draw out some conclusions and outline future perspectives in chapter 4. The complete list of the papers that form the basis of the thesis is given in the subsection "Main contributions" of the section "Peer-reviewed publications". All these papers are included as sections, except PAPER7 and PAPER8. The reason for this is that the work of PAPER7 is presented here in a somewhat different manner and that the content of PAPER8 has been distributed amongst sections 3.4 and 3.6 to fit better the structure of the thesis.

Fundamentals of metamaterials

THE TERM METAMATERIAL was coined by Rodger M. Walser in 1999, which he later defined as "macroscopic composites having a synthetic, three-dimensional, periodic cellular architecture designed to produce an optimized combination, not available in nature, of two or more responses to specific excitation". This original definition has been refined and modified depending on the context during the last decade.[10] Let us examine in depth the idea behind the metamaterial concept.

As is well known, the fundamental electromagnetic fields **E** (electric field strength) and **B** (magnetic induction) are able to alter the charge distribution of a medium and induce currents in it. Such alterations act as new sources that, in turn, generate additional electromagnetic fields. This electromagnetic response of a medium to an external excitation depends on the kind of its constitutive atoms and on how these atoms are bound, *i.e.*, its chemistry. Although complex, it is possible to model these field-matter interactions in a relatively simple fashion by performing a microscopic average of the fields and defining two new auxiliary fields, namely **D** (electric displacement) and **H** (magnetic field strength). As a result, all medium properties are condensed into two constants known as the constitutive parameters: the electric permittivity ε and the magnetic permeability μ (a more general case will be considered later). The averaging process gives rise to the so-called macroscopic Maxwell's equa-

(a)

(b)

(c)

(d)

(e)
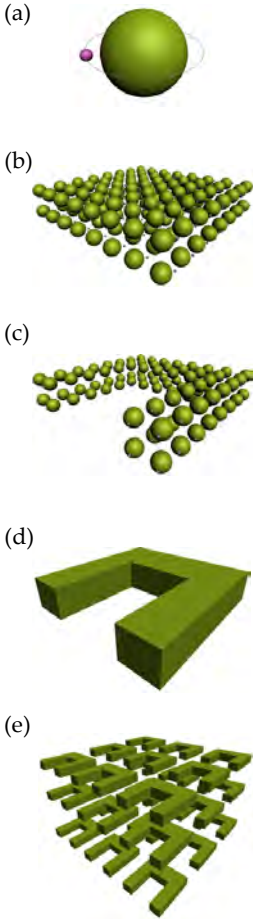
Figure 1.1: (a) Atom. (b) Medium made up of multiple atoms that can be characterized by a set of parameters ε_1 and μ_1. (c) Medium in (b) after structuring. (d) Meta-atom: the structure in (c) can be regarded as the constitutive atom of a meta-medium. (e) Meta-medium that can be characterized by parameters ε_m and μ_m, which depend on the geometry of the meta-atom and on ε_1 and μ_1.

[1] In general, if the meta-atom is made up of n different materials, ε_m and μ_m depend on all of their constitutive parameters ε_1, μ_1, ε_2, μ_2, ..., ε_n and μ_n.

tions[11], which in MKS units read

$$\text{FARADAY'S LAW} \quad \nabla \times \mathbf{E} + \frac{\partial \mathbf{B}}{\partial t} = 0 \qquad \nabla \cdot \mathbf{B} = 0 \quad \text{GAUSS'S LAW}$$

(1.1)

$$\text{AMPERE'S LAW} \quad \nabla \times \mathbf{H} - \frac{\partial \mathbf{D}}{\partial t} = \mathbf{J} \qquad \nabla \cdot \mathbf{D} = \rho \quad \text{GAUSS'S LAW}$$

(1.2)

where ρ is the free charge density and $\mathbf{J}$ is the free current density (symbols in bold represent vector quantities, whereas symbols in italics represent scalar quantities). Eqs. (1.1) represent the source-free (homogeneous) equations and Eqs. (1.2) the source (inhomogeneous) equations of the electromagnetic field.

In order to build optical devices, we can combine several materials with different properties (permittivity and permeability) that determine the functionality of the desired device. However, the range of permittivity and permeability values found in natural media are limited and, as a consequence, so are the devices that we can construct with them. Since we cannot create new elements to add to the periodic table, how could we expand the available range of properties, and thus open the door for new devices and functionalities? Metamaterials can provide the solution.

The idea behind metamaterials lies on using natural media to create artificial atoms (*meta-atoms*) upon which to build new materials exhibiting tailor-made properties, resulting from a second averaging level. Such meta-atoms will be made up of a certain number of atoms of some natural substance. This number will be large enough that the structured natural substance can be characterized by its permittivity ε_1 and permeability μ_1, after the conventional averaging process (first averaging level). At the same time, the size of the meta-atom should be small enough (typically one order of magnitude smaller than the wavelength) that a second averaging process is possible. This way, a medium composed of a periodic array of these meta-atoms can be characterized by a new set of parameters ε_m and μ_m, after the second averaging of the already macroscopic fields propagating through this artificial *meta-medium* or metamaterial. Obviously, ε_m and μ_m will depend on the specific geometry of the meta-atom, as well as on ε_1 and μ_1.[1] The great potential of metamaterials comes from the new degree of freedom provided

by this dependence on the geometry of the meta-atom, which allows us to synthesize permittivity and permeability values that do not exist in nature. Let us see how these concepts can be used to produce artificial dielectric and magnetic materials.

1.1 Metamaterials as effective media

In the classical homogenization process, it is customary to define the following quantities [11]

- Polarization (**P**): expresses the density of electric dipole moments. The electric dipolar moment of two point charges $+q$ and $-q$ separated by a directed distance **d** pointing from $+q$ to $-q$ is $\mathbf{p} = q\mathbf{d}$.

- Magnetization (**M**): expresses the density of magnetic dipole moments. The magnetic dipole moment of a planar closed current loop with vector area **S** carrying a total electric current I is $\mathbf{m} = I\mathbf{S}$.

The auxiliary fields **D** and **H** are defined in terms of the polarization and magnetization through the so-called *constitutive relations*, which account for the response of the medium bound charges and currents to the applied fields [2]

$$\mathbf{D} = \overbrace{\varepsilon_0 \mathbf{E} + \mathbf{P}_E}^{\varepsilon_0 \varepsilon \mathbf{E}} + \overbrace{\mathbf{P}_H}^{-ic_0^{-1}\zeta\mathbf{H}}, \tag{1.3}$$

$$\mathbf{B} = \underbrace{\mu_0 \mathbf{H} + \mu_0 \mathbf{M}_H}_{\mu_0 \mu \mathbf{H}} + \underbrace{\mathbf{M}_E}_{ic_0^{-1}\zeta\mathbf{E}}, \tag{1.4}$$

All the fields appearing in Eqs. (1.3)-(1.4) are volume-averaged quantities. These same equations can be used for a second time to calculate the constitutive parameters of a metamaterial, in which case we will be averaging again the already averaged fields. Note that we have split the polarization and magnetization into two terms related to their physical origin. The most common situation is that in which an electric field induces electric dipoles in the medium giving rise to a polarization $\mathbf{P}_E$ and the magnetic field induces magnetic dipoles giving rise to a magnetization $\mathbf{M}_H$. However, some substances exhibit a more complex behavior in which the electric field can generate a magnetization $\mathbf{M}_E$, while the magnetic field is able to produce a polarization $\mathbf{P}_H$. This cross behavior is known as bianisotropy.

[2] $c_0 = (\varepsilon_0 \mu_0)^{-1/2}$ is the speed of light in vacuum

The bianisotropy factor ξ measures the degree of bianisotropy. In general, the properties of the material depend on the direction of the fields, in which case ε, μ and ξ are tensors.

Case of study: the split ring resonator

Probably, the most widely-used meta-atom for the creation of artificial magnetism is the split ring resonator (SRR).[12] There exist a number of variants of this structure with different properties.[13,14] Here we will study its simplest form, a metallic ring with a slit [see Figure 1.2(a)], as an example of how the constitutive parameters of a metamaterial can be obtained. For this purpose, we will follow the lines of Refs.[15,16] We will calculate the response of the structure when illuminated by an electromagnetic field polarized as in Figure 1.2(a). Consequently, we are considering the following part of the constitutive relations

$$D_x = \varepsilon_0 \varepsilon E_x - ic_0^{-1}\xi H_y \qquad (1.5)$$

$$B_y = ic_0^{-1}\xi E_x + \mu_0 \mu H_y. \qquad (1.6)$$
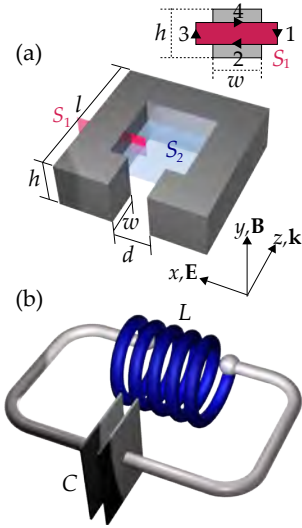
Figure 1.2: SRR and equivalent circuit.

Then, the constitutive parameters appearing in the previous relations are only valid for this polarization of the incident field. We can think of the SRR as an RLC circuit, where the metallic ring (ideally without the slit) can be modeled as an inductor, the slit itself as a parallel-plate capacitor, and the ohmic and radiation losses as a distributed resistor [see Figure 1.2(b)]. The (self)inductance of a circuit is defined as $L = \Phi/I$, where I is the total electric current flowing through the circuit and $\Phi = \iint_S \mathbf{B} \cdot d\mathbf{S}$ is the magnetic flux passing through the surface S enclosed by the circuit. In the case of the SRR, $S = S_2$. Assuming that $\mathbf{B}$ is constant along S_2 and perpendicular to it, $\Phi = BS_2 \approx Bl^2$ (we denote by A the magnitude of a vector field $\mathbf{A}$). On the other hand, if we apply the integral form of Ampère's law, *i.e.*, $\oint_C \mathbf{H} \cdot d\mathbf{l} = \iint_S (\mathbf{J} + \frac{\partial \mathbf{D}}{\partial \mathbf{t}}) \cdot d\mathbf{S}$ to surface S_1, we obtain that $H = I/h$. Note that we have neglected the displacement current (Ohmic current dominates) and we have assumed that $\mathbf{B}$ vanishes along paths 2-4. Combining these two results we find that the inductance of the SRR is $L = \mu_0 l^2/h$. The capacitance of a parallel plate capacitor equals the dielectric

constant of the spacer times the area of a plate divided by the separating distance. Thus, for the SRR we have $C = \varepsilon_0 wh/d$. An incident magnetic field H induces a current I. Both are related by the circuital version of Faraday's law

$$\underbrace{V_L}_{L\frac{dI}{dt}} + \underbrace{V_C}_{\frac{1}{C}\int I\,dt} + \underbrace{V_R}_{RI} = -\iint_{S_2} \frac{\partial \mathbf{B}}{\partial t} \cdot d\mathbf{S}, \tag{1.7}$$

Assuming a time-harmonic variation of the fields,[3] Eq. (1.7) becomes $-i\omega\,LI + i(C\omega)^{-1}I + RI = i\omega\mu_0\,HS_2$, yielding:

$$I = \frac{\mu_0\omega^2 l^2}{L\left(\omega_{LC}^2 - \omega^2 - i\gamma\omega\right)}H, \quad \text{with} \quad \omega_{LC} = \frac{1}{\sqrt{LC}}, \quad \gamma = \frac{R}{L}. \tag{1.8}$$

The incident magnetic field induces a magnetic moment $\mathbf{m} = I\mathbf{S_2}$ in each SRR, where $\mathbf{S_2} = S_2\mathbf{z}$. Thus, if the SRRs are periodically arranged with periodicities a_x, a_y and a_z in each of the principal directions, the magnetization due to $\mathbf{H}$ is

$$\mathbf{M}_H = \frac{I\mathbf{S}_2}{a_x a_y a_z} = \frac{F\omega^2}{\omega_{LC}^2 - \omega^2 - i\gamma\omega}\mathbf{H} \quad \text{with} \quad F = \frac{l^2 h}{a_x a_y a_z} \tag{1.9}$$

The incident magnetic field also induces an electric moment $\mathbf{p}$ in each SRR, since charges of different sign accumulate at opposite sides of the slit. Since $q = \int I\,dt$, the polarization induced by H is

$$\mathbf{P}_H = \frac{\mathbf{d}\int I\,dt}{a_x a_y a_z} = \frac{iF\omega\,H}{l^2\left(\omega_{LC}^2 - \omega^2 - i\gamma\omega\right)}\mathbf{d} \tag{1.10}$$

On the other hand, the electric field produces a voltage drop Ed so that

$$V_L + V_C + V_R = Ed. \tag{1.11}$$

Following the same procedure as before, we find that the current, magnetization and polarization induced by the incident

electric field are

$$I = \frac{-id\omega}{L\left(\omega_{LC}^2 - \omega^2 - i\gamma\omega\right)} E \tag{1.12}$$

$$\mathbf{M}_E = \frac{-iF\omega}{\mu_0 l^2 \left(\omega_{LC}^2 - \omega^2 - i\gamma\omega\right)} \mathbf{E} \tag{1.13}$$

$$\mathbf{P}_E = \frac{Fd^2}{\mu_0 l^4 \left(\omega_{LC}^2 - \omega^2 - i\gamma\omega\right)} \mathbf{E} \tag{1.14}$$

From Eqs. (1.9)-(1.10) and (1.13)-(1.14) we deduce the constitutive parameters of the studied SRR

$$\varepsilon = 1 + \frac{c_0^2 d^2 F}{l^4 \left(\omega_{LC}^2 - \omega^2 - i\gamma\omega\right)} \tag{1.15}$$

$$\mu = 1 + \frac{F\omega^2}{\omega_{LC}^2 - \omega^2 - i\gamma\omega} \tag{1.16}$$

$$\xi = \frac{-dc_0 F\omega}{l^2 \left(\omega_{LC}^2 - \omega^2 - i\gamma\omega\right)} \tag{1.17}$$

Retrieval of metamaterials effective parameters

Due to the complexity of many structures, it is not always feasible to determine analytically their effective parameters like we did with the SRR. Some methods enable us to obtain the effective parameters from the total fields in the structure, which can be numerically calculated.[17,18] However, we need a different method to obtain the effective parameters of experimental metamaterials. It has been shown that it is possible to obtain a set of effective constitutive parameters from the structure transmission and reflection coefficients — or equivalently the so-called *S* parameters — for normal incidence, if both amplitude and phase are known. This procedure, known as the Nicolson-Ross-Weir (NRW) method,[19,20] is based on the inversion of the Fresnel-Airy expression for the reflection and transmission of plane waves in layers of continuous media. The use of this method to obtain metamaterial effective parameters was first described in Ref. 21 and has been applied to many different metamaterials employing computational or even experimental results although phase measurements in reflection and transmission are difficult to realize at optical frequencies.

Since first used in 2002, limitations and drawbacks of the NRW me-thod have been studied by several authors. One of

these limitations is that it is assumed that impinging light is a plane wave perpendicular to the metamaterial. Thus, this procedure only provides the tangential components of the effective parameter tensors in the case of anisotropic media. Although extensions of the retrieval method to bianisotropic composites and oblique incidence have been reported,[22,23] for the majority of the proposed optical metamaterials the retrieved parameters depend on the incident angle, as it has been pointed out by several authors.[23,24] Spatial dispersion is mainly responsible for this angular dependence, which can be detected from the fact that the equi-frequency surfaces have not an ellipsoidal or hyperbolical shape. In order to be considered as global bulk effective parameters, a unique set of these parameters should describe the behavior of the medium and even the wave reflection and transmission at the interface for all possible angles. In this case, the retrieved effective parameters are called global or characteristic material parameters,[23,24] like those attributed to natural media. Otherwise, the retrieved parameters are called wave or just effective material parameters and a different set is required for each spatial direction so that the parameters retrieved at normal incidence do not provide information on the transmission and reflection properties of the medium at any other angle of incidence. Nonetheless, these effective parameters can provide useful information about the artificial medium to which they are related. Moreover, even wave parameters are meaningless if high-order Bloch modes are not negligible.[25] The presence of high-order Bloch modes becomes apparent when the effective parameters depend on the number of metamaterial layers in the propagation direction. Thus, it is a requirement that the retrieved parameters are independent of this number (at least from a certain value).

We would like to stress that our main goal is not to obtain an isotropic medium that can be described by global bulk characteristic material parameters. In fact it has been pointed out that trying to achieve a metamaterial that can be described by a unique set of characteristic parameters for the whole spatial spectrum is not a realistic task and that it could be reasonable to assign characteristic material parameters describing the medium only in a certain angular interval.[26] However, in order to be effective parameters, they do need to be independent of the num-

ber of metamaterial layers, which could be even one. Since bianisotropy will be present in some of the structures that we will study, we need an algorithm that includes the possibility of a bianisotropic behavior, as the one described in Ref. 16. However, that algorithm assumes that the metamaterial whose properties we want to retrieve is surrounded by semi-infinite media. Nonetheless, in some cases we will consider different situations. Thus, we propose a modified version of the method in Ref. 16 that allows us to work in a more general situation. To this end, we consider the problem depicted in Figure 1.3, where we focus our attention on the two media adjacent to the unknown metamaterial (which we assume to exhibit no bianisotropy). As they could be part of a multilayer structure, both a progressive and a regressive wave can be propagating in each of them. The problem we want to solve can be modeled by Eqs. (1.5)-(1.6), which have two plane-wave eigensolutions $\mathbf{E}_\pm \exp\left(\pm ik_z z - i\omega t\right)$ and $\mathbf{H}_\pm \exp\left(\pm ik_z z - i\omega t\right)$ with

Figure 1.3: A metamaterial with unknown characteristic impedances $z_\pm$ and refractive index n is surrounded by multilayer structures. The left and right adjacent media have characteristic impedances z_1 and z_2. Orange and blue arrows refer to incidence from the left and from the right, respectively. Progressive and regressive waves propagating in each medium are shown.

$$k_z^2 = \omega^2 \mu_0 \varepsilon_0 \overbrace{\left(\varepsilon\mu - \xi^2\right)}^{n^2},\qquad(1.18)$$

$$z_+ = \frac{1}{Z_0}\frac{E_+}{H_+} = \mu\left(n - i\xi\right)^{-1},\qquad(1.19)$$

$$z_- = \frac{1}{Z_0}\frac{E_-}{H_-} = \mu\left(-n - i\xi\right)^{-1},\qquad(1.20)$$

where $Z_0 = \left(\mu_0/\varepsilon_0\right)^{1/2}$. Our goal is to obtain the characteristic impedances $z_\pm$ and the refractive index n from $r_\pm$, $t_\pm$ and $p_\pm$ (see Figure 1.3), which we are supposed to know from either simulation or experiment. By forcing the continuity of the tangential fields at the boundaries of the metamaterial, we find the equation giving rise to the two possible solutions for $z_\pm$:

$$az_\pm^2 + bz_\pm + c = 0,\qquad(1.21)$$

with

$$a = \left(t_+ - p_+\right)\left(t_- - p_-\right) - \left(1 - r_+\right)\left(1 - r_-\right),$$
$$b = \left(z_1 - z_2\right)\left(1 + t_+ t_- - p_+ p_- - r_+ r_-\right)$$
$$\quad + \left(z_1 + z_2\right)\left(r_+ - r_- + t_+ p_- - p_+ t_-\right),$$
$$c = z_1 z_2\left[\left(1 + r_+\right)\left(1 + r_-\right) - \left(t_+ + p_+\right)\left(t_- + p_-\right)\right],$$

For a passive medium, $\text{Re}(z_+)$ and $\text{Re}(-z_-)$ must be positive. The solution for n can be obtained from the relation

$$2\cos(nk_0 d) = \frac{\frac{z_+}{z_1} - 1 - r_+ \left(1 + \frac{z_+}{z_1}\right)}{\frac{z_+}{z_2}(t_+ - p_+) - t_+ - p_+} + \frac{1 - \frac{z_-}{z_1} + r_+ \left(1 + \frac{z_-}{z_1}\right)}{\frac{z_-}{z_2}(p_+ - t_+) + t_+ + p_+}$$

(1.22)

Finally, the metamaterial constitutive parameters are calculated by inverting the expressions for n and $z_\pm$ given by Eqs. (1.18)-(1.20)

$$\xi = i\frac{z_- + z_+}{z_- - z_+}n, \tag{1.23}$$

$$\varepsilon = (n + i\xi)/z_+, \tag{1.24}$$

$$\mu = (n - i\xi)/z_+. \tag{1.25}$$

If we have a multilayer structure at one or both sides of the metamaterial and we only know the fields at the input and output of the system, we can easily obtain $r_\pm$, $t_\pm$ and $p_\pm$ by forcing the continuity of tangential fields at each boundary, for instance by using a transfer matrix method. The most complex structure that we will consider is shown in Figure 1.4, where the metamaterial is placed over a semi-infinite substrate and there is a layer of thickness d_c between the metamaterial and the input medium. It is assumed that we know the denormalized S parameters relating incident, reflected and transmitted fields as in Figure 1.4.[4] In this case, it can be shown that $p_\pm$, $r_\pm$, $t_\pm$, and the S parameters satisfy the following expressions:

$$r_+ = \frac{1 + S_{11} - \frac{z_c}{z_1}(1 - S_{11})}{1 + S_{11} + \frac{z_c}{z_1}(1 - S_{11})}e^{-2ik_0 n_c d_c} \tag{1.26}$$

$$t_+ = \frac{2S_{21}}{1 + S_{11} + (1 - S_{11})\frac{z_c}{z_1}}e^{-ik_0 n_c d_c} \tag{1.27}$$

$$p_+ = 0 \tag{1.28}$$

$$r_- = S_{22} \tag{1.29}$$

$$t_- = \frac{1}{2}\left(1 + \frac{z_c}{z_1}\right)S_{12}e^{-ik_0 n_c d_c} \tag{1.30}$$

$$p_- = \frac{1}{2}\left(1 - \frac{z_c}{z_1}\right)S_{12}e^{ik_0 n_c d_c} \tag{1.31}$$

To calculate the metamaterial constitutive parameters we first use Eqs. (1.26)-(1.31), and then substitute the results into Eqs.

Input z_{in}	Cover n_c, z_c	M e t a m a t e r i a l	Output z_{out}
E_i	E_{int}		$S_{21}E_i$
$S_{11}E_i$	$r_+ E_{int}$		$p_+ E_{int}=0$
$S_{12}E_i$	$t_- E_i$		E_i
	$p_- E_i$		$S_{22}E_i$
	d_c	d	
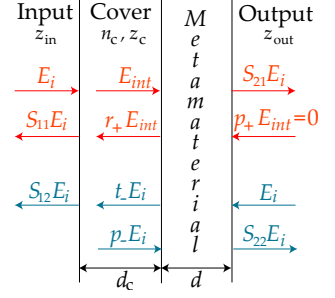
Figure 1.4: Retrieval of constitutive parameters of a metamaterial embedded in a multilayer structure. The metamaterial is placed over a semi-infinite substrate (output medium). There is an upper layer (cover) of thickness d_c between the metamaterial and the semi-infinite input medium.

[4] In microwave engineering, the scattering parameters are defined as $\bar{S}_{ji} = b_j/a_i$, where $b_j = A_j^{out}/\sqrt{z_j}$ and $a_i = A_i^{in}/\sqrt{z_i}$ are the input and output waves at ports j and i normalized to the characteristic impedance of the corresponding port. Thus, the denormalized S parameters defined in Figure 1.4 are related to those defined in microwave engineering by

$$\begin{aligned} S_{11} &= \bar{S}_{11} \\ S_{12} &= \bar{S}_{12}\sqrt{z_{in}/z_{out}} \\ S_{21} &= \bar{S}_{21}\sqrt{z_{out}/z_{in}} \\ S_{22} &= \bar{S}_{22} \end{aligned}$$

(1.21)-(1.22). The ambiguities inherent to Eq. (1.22) as well as other tricky aspects of the retrieval method[21,27] were taken into account in our numerical implementation of the algorithm.

1.2 Artificial dielectrics

The first effective medium theories of composites of macroscopic materials started to be developed more than a century ago. One of the oldest and most popular ones is Maxwell-Garnett's formula, which provides the effective permittivity of homogeneous spheres diluted into an isotropic environment as a function of the permittivity of both media and the spheres filling fraction.[28] Of special interest to us are artificial negative-permittivity materials as a means to obtain NIMs. This kind of media is much easier to achieve than artificial magnetic structures, since many natural materials exhibit a negative permittivity in a certain spectral range. In fact, most metals present a negative permittivity at frequencies below the so-called plasma frequency, which usually lies in the UV part of the spectrum. As a consequence, tailor-made negative permittivities can be readily obtained by using metallic meta-atoms. Artificial magnetism is considerably more difficult to attain, specially at optical frequencies, where natural media display no magnetic response. The majority of negative-permeability metamaterials also use metallic inclusions to obtain resonant magnetic responses. Clearly, metals play a crucial role in the creation of NIMs and it is very important to understand their effective properties. The Drude model describes very accurately the behavior of metals up to visible wavelengths. Moreover, one of the most influential works on artificial negative-permittivity materials[29] — although arguably not the first[30] — uses concepts of this model. Next, we describe both.

Drude model for metals

The electron cloud of an atom is bound to the positive nucleus by an attractive force that keeps it in an equilibrium configuration. For small displacements $\mathbf{x}$, this restoring force approximately has a linear dependence on $\mathbf{x}$. Natural media are formed by a high number of polarizable atoms periodically arranged

with a lattice constant much smaller than the wavelength. An incident electric field acts as a driving force that makes each atom behave as a forced oscillator. In addition, there exists a damping force proportional to the velocity. Applying Newton's second law to this system we obtain

$$q_e \mathbf{E} - k\mathbf{x} - m_e \gamma \frac{d\mathbf{x}}{dt} = m_e \frac{d^2 \mathbf{x}}{dt^2}, \qquad (1.32)$$

where q_e and m_e are the electron charge and mass, and k is a constant. Again, under the time-harmonic assumption this equation becomes

$$\mathbf{x} = \frac{q_e}{m_e \left(\omega_0^2 - \omega^2 - i\gamma\omega \right)} \mathbf{E} \qquad \text{with} \qquad \omega_0^2 = \frac{k}{m_e}. \qquad (1.33)$$

If N is the density of electrons, the polarization induced by $\mathbf{E}$ is $\mathbf{P} = Nq_e\mathbf{x}$. Therefore, such a medium can be characterized by a permittivity

$$\varepsilon = 1 + \frac{\omega_p^2}{\omega_0^2 - \omega^2 - i\gamma\omega} \qquad \text{with} \qquad \omega_p^2 = \frac{Nq_e^2}{\varepsilon_0 m_e}. \qquad (1.34)$$

Metal	$\omega_p (rad/s)$	$\gamma (rad/s)$
Au	$1.37 \cdot 10^{16}$	$4.00 \cdot 10^{13}$
Ag	$1.37 \cdot 10^{16}$	$2.73 \cdot 10^{13}$
Cu	$1.12 \cdot 10^{16}$	$1.38 \cdot 10^{13}$
Al	$2.24 \cdot 10^{16}$	$1.24 \cdot 10^{14}$

Table 1.1: Values of ω_p and γ for common metals.[31,32]

In the free-electron model of metals, there is no restoring force ($\omega_0 = 0$) and the plasma frequency ω_p is the frequency at which the real part of ε becomes positive. Typical values for common metals are given in table 1.1.

Diluted plasma

Here we briefly describe the utilization of thin metal wires for achieving a medium with tailored negative permittivity.[29]

The wires are supposed to have a radius r and to be distributed along three orthogonal directions with periodicity a (see Figure 1.5). Consider for simplicity that the electric field is directed along one of the principal directions. The *active* wires will be those whose axis is parallel to that direction. If the electron density of the metal is N, the wire medium has an effective density $N_{\text{eff}} = N\pi r^2/a^2$. There is an additional effect due to the structure self-inductance against which any restoring force must work, apart from the inertial mass accounted by Drude's model. This auto-inductance can be represented by an effective electron mass[5] $m_{\text{eff}} = \mu_0 r^2 q_e^2 N \ln(a/r)/2$.[29] We can obtain the effective permittivity of the diluted plasma by inserting N_{eff}

Figure 1.5: Diluted plasma.

[5] The introduction of an effective mass may lead to some inconsistencies.[33]

and m_{eff} into Eq. (1.34), which is that of a metal with an effective plasma frequency:

$$\omega^2_{p\,\text{eff}} = \frac{2\pi\,c^2}{a^2\ln(a/r)} \tag{1.35}$$

As an example, for Al wires with $r = 1\ \mu$m and $a = 5$ mm, we get $\omega_{p\,\text{eff}} \approx 8.2 GHz$, which is considerably smaller than that of bulk Al (see Table 1.1). Wire media have been extensively studied in the last years.[34,35,36,37]

1.3   Artificial magnetism

Apart from the SRR, a variety of structures have been proposed with the aim of obtaining media displaying an effective permeability different from unity. Like in the SRR, magnetic responses are typically achieved by means of metallic structures in which resonant electric currents are induced by the magnetic field of an incident wave. Above the resonance frequency, these currents are out of phase with respect to the driving incident wave and generate a magnetic field that opposes the incident one. If the resonance is strong enough, this diamagnetic behavior leads to a negative permeability. Although initial work was focused on the microwave range, much attention has been put in extending this sought after property to optical wavelengths.[38,39,40] This effort is justified by the fact that it is in the visible regime where we can make the most of important metamaterial applications in which a magnetic response is required, *e.g.*, cloaking. During this thesis, we were particularly interested in negative permeability at visible frequencies for two reasons:

- It is an essential ingredient for low-loss NIMs in this part of the spectrum — and in any other one — as we will see below.

- It could form the basis of a new approach to optical security.

Both points are developed in next chapter. The first approach towards negative optical magnetism was to take advantage of the scaling properties of Maxwell's equations[1] and scale down the meta-atom size to increase the resonance frequency at which the magnetic resonance occurred. Unfortunately, there exist limits that prevent us from increasing the resonance frequency to

an arbitrary high value, since metals stop behaving as perfect conductors in the optical range.[13] Up to date, a number of structures have been proposed to solve this problem. In Table 1.2 we list the most important ones (to our knowledge). Only a few of them have reached the experimental stage, namely, parallel pairs of metallic strips and its complementary structure: the so-called fishnet metamaterial[41,42], which has provided the best results to date.

Metamaterial	λ_{min} (nm) with $\mu<0$	Polar. indep.	Observations
4-cut SRR[13]	600	Yes	Very weak response in the visible
Nano-sphere circular array[43,44,45]	430	Yes	μ=-1.5 (450 nm). Can exhibit $n<0$
Parallel pairs of silver strips[46,47,48]	550	No	μ=-1.7 (725 nm)*
Experimental 1st order fishnet[49−52]	735	No	μ hardly negative without gain*
Cut thick nano-strips[PAPER5]	425	Yes	μ=-5 (470 nm). Can exhibit $n<0$
Densely packed nano-spheres[53]	760	Yes	μ=-0.5 (760 nm)
Theoretical 1st order fishnet[54]	–	No	μ=-2.5 (789 nm). Can exhibit $n<0$
Nano-hoops[PAPER6]	475	No	μ=-5
Coaxials[PAPERb4, 55]	450	Yes	μ=-1 Can exhibit $n<0$
2nd order fishnet[PAPER2−3]	–	No	μ=-2.5 (789 nm). Can exhibit $n<0$*

Table 1.2: State of the art in metamaterials with magnetic response in the visible spectrum. Experimental designs are denoted by an asterisk.

Negative index media

We start this chapter by describing the basics of negative index media. For simplicity, we will restrict ourselves to isotropic materials — there is a natural extension to more general media. If we take the curl of Faraday's law, substitute the result in Ampère's law and use the vector identity $\nabla \times (\nabla \times \mathbf{A}) = \nabla(\nabla \cdot \mathbf{A}) - \nabla^2 \mathbf{A}$, we obtain the so-called wave equation:[1]

$$\nabla^2 \mathbf{E} - \mu_0 \varepsilon_0 \mu \varepsilon \frac{\partial^2 \mathbf{E}}{\partial t^2} = 0 \qquad (2.1)$$

Assuming a harmonically varying field, the solution to Eq. (2.1) is a linear combination of terms of the form

$$\mathbf{E} = \mathbf{E}_0 \, e^{i(\mathbf{k} \cdot \mathbf{r} - \omega t)}, \qquad (2.2)$$

where $\mathbf{E}_0$ is a constant. This corresponds to a monochromatic wave with angular frequency ω propagating with a phase velocity $\mathbf{v}_p = \frac{\omega}{k}\hat{k}$ (which can be determined by demanding the exponential phase to be constant and taking the derivative with respect to time). Therefore, this wave propagates towards the direction given by $\mathbf{k}$ (ω is always positive) at a speed $c = \omega/k$. The vector $\mathbf{k} = k\hat{k}$ is known as the wavevector and its magnitude k as the wavenumber. Introducing the solution given by Eq. (2.2) in Eq. (2.1) we obtain the well-known dispersion relation[56]:

$$k^2 = \omega^2 \mu_0 \varepsilon_0 \mu \varepsilon \Rightarrow c^2 = \frac{\omega^2}{k^2} = \frac{1}{\mu_0 \varepsilon_0 \mu \varepsilon} = \frac{c_0^2}{\mu \varepsilon} = \frac{c_0^2}{n^2}, \qquad (2.3)$$

c_0 being the phase velocity in vacuum. This equation links the angular frequency ω with the wavenumber k. We have defined the medium refractive index n as

$$n^2 = \varepsilon \mu. \qquad (2.4)$$

[1] We consider here that propagation takes place in a linear, isotropic, homogeneous and non-dispersive medium. Otherwise, the wave equation has a more complex form than that given by Eq. (2.1).

Thus, the refractive index is the ratio between the speed of light in vacuum c_0 and the speed of light in the medium c. In general, ε and μ are complex numbers (in the frequency domain) whose imaginary parts account for the losses. To simplify the following reasoning, we will assume that losses are negligible so that the constitutive parameters are real. As a consequence, it is obvious from Eq. (2.3) that a simultaneous change in the sign of ε and μ has no effect in the dispersion relation. This fact can be interpreted in several ways. One of them could be to admit that there is no physical difference between a substance with negative or positive constitutive parameters, as long as they both have the same sign. It might also be possible that simultaneously negative ε and μ violate some physical law and that a material with such properties cannot exist. Finally, there is a possibility that such a material could exist and that its properties are different from those of a material with the same constitutive parameters but of opposite sign. In 1968, the Russian scientist Victor Veselago addressed this problem proving that the correct option corresponds to this last possibility.[57] His work remained as a mere theoretical curiosity until more than 30 years later, when several experiments corroborated his arguments.[58,59] In fact, Eq. (2.4) indicates that

$$n = \pm\sqrt{\varepsilon\mu}. \tag{2.5}$$

Of the two solutions, traditionally the positive-sign one has been chosen, but this is not always correct. Let us analyze the properties of a monochromatic wave propagating through a medium with negative ε and μ to justify this statement. Regardless of the sign, the equation to solve is still Eq. (2.1), whose solution is given by Eq. (2.2). The magnetic field can be calculated by substituting Eq. (2.2) in Faraday's law, yielding

$$\mathbf{H} = \frac{\hat{k}}{z} \times \mathbf{E}, \tag{2.6}$$

where we have defined the characteristic impedance of the medium as

$$z = \frac{\mu_0\mu}{n} = \sqrt{\frac{\mu_0\mu}{\varepsilon_0\varepsilon}}. \tag{2.7}$$

It is evident from Eqs. (2.4)-(2.7) that z and n univocally determine the electromagnetic behavior of a continuous medium, in
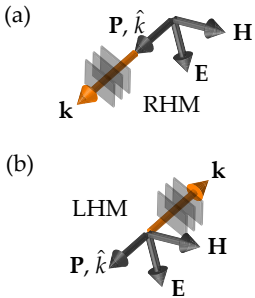
Figure 2.1: ($\mathbf{E}$, $\mathbf{H}$, $\mathbf{k}$) triplet and Poynting vector $\mathbf{P}$ in (a) RHM and (b) LHM.

the same way as ε and μ do. Substituting Eqs. (2.2) and (2.6) into Faraday's and Ampère's laws, we find that

$$\mathbf{k} \times \mathbf{E} = \omega\mu_0\mu\mathbf{H}, \tag{2.8}$$

$$\mathbf{k} \times \mathbf{H} = -\omega\varepsilon_0\varepsilon\mathbf{E}. \tag{2.9}$$

Continuing with the lossless-medium assumption,[2] the previous relations indicate that if ε and μ are both positive, (**E**, **H**, **k**) form a right-handed triplet, whereas if they are both negative the triplet is left-handed (see Fig 2.1). It is for this reason that this kind of media have been termed left-handed media (LHMs), as opposed to right-handed media (RHMs). The direction of energy flow is given by Poynting's vector

$$\mathbf{P} = \mathbf{E} \times \mathbf{H}, \tag{2.10}$$

which always has the same direction relative to the fields, regardless of the sign of n. This direction points away from the source and is given by $\hat{k}$, as reflected in Eqs. (2.6)-(2.9). Moreover, in low-loss media — and in general in most media — the velocity of energy is given by the group velocity v_g.[61] Since ω is always positive and $\hat{k}$ is the propagation direction, it is clear from Eq. (2.3) and Fig 2.1 that k is positive for RHMs and negative for LHMs. Therefore, the previous expression indicates that, defining the positive direction as that of v_g (**P** in general), v_p will be positive for RHMs and negative for LHMs. In addition, since n expresses the ratio between the speed of light in vacuum and in the medium, we must write the wavenumber as

$$k = \frac{\omega}{c_0}n. \tag{2.11}$$

This argument allows us to solve the indetermination in the sign of Eq. (2.5). If v_p is negative in a medium, n must be negative and vice versa. This way, the definition of the wavenumber as $k = k_0 n$ is consistent (k_0 is the wavenumber in vacuum). For this reason, LHMs are also known as NIMs (negative index media). Finally, if ε and μ are of different sign, n will be purely imaginary resulting in an evanescent wave. Note that a simultaneous change in the sign of ε and μ does not change the value of z, since n and μ would still have the same sign [see Eq. (2.7)]. It is worth mentioning that for a dissipative medium ($\varepsilon = \varepsilon' + i\varepsilon''$, $\mu = \mu' + i\mu''$) to be a NIM, having simultaneously

[2] The same argument is valid for a lossy medium, since it would only imply attenuation of the fields and would not affect the phase.[60]

negative real parts of the permittivity and the permeability is a sufficient but not necessary condition. The strictly necessary condition is given by[62]

$$\varepsilon'\mu'' + \varepsilon''\mu' < 0 \qquad (2.12)$$

Consequently, we could achieve a negative index in a medium with $\mu' < 0$ and high polarization loss, even if the permittivity has a positive real part. However, this high loss will usually invalidate the practical use of such a medium.

2.1   Properties of negative index media

NEGATIVE INDEX MEDIA present a series of properties that sometimes give rise to counterintuitive physical phenomena, as they do not occur in natural materials. Next, we describe the most important ones, putting special emphasis on those that are closely related to this work.

Negative refraction

In this section we will analyze the reflection and refraction of electromagnetic waves at the interface between an LHM and an RHM. The boundary conditions at the interface between two media as derived from Maxwell's equations are

$$\hat{n} \cdot (\mathbf{D_2} - \mathbf{D_1}) = \sigma_e, \qquad (2.13)$$
$$\hat{n} \cdot (\mathbf{B_2} - \mathbf{B_1}) = \sigma_m, \qquad (2.14)$$
$$\hat{n} \times (\mathbf{E_2} - \mathbf{E_1}) = -\mathbf{M_s}, \qquad (2.15)$$
$$\hat{n} \times (\mathbf{H_2} - \mathbf{H_1}) = \mathbf{J_s}, \qquad (2.16)$$

where $\hat{n}$ is the unit vector normal to the interface that points from medium 1 to medium 2, σ_e and σ_m are the electric and (fictitious) magnetic surface charge density on the boundary, and $\mathbf{J}_s$ and $\mathbf{M}_s$ are the electric and (fictitious) magnetic surface current density. Clearly, these conditions hold irrespective of the sign of the refractive indices of the intervening media, as long as we use the correct signs for the permittivity and permeability. Let us consider that medium 1 is RH and medium 2 is LH or vice versa and that both media can be modeled as dielectrics
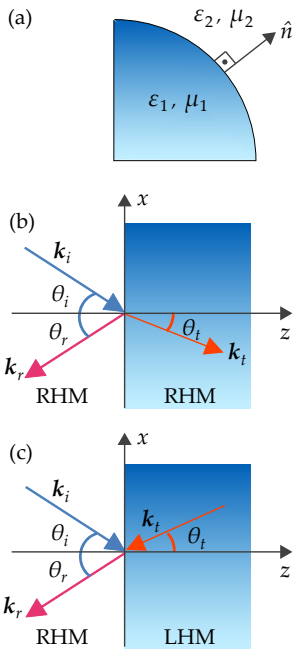
Figure 2.2: Negative refraction

(surface charges and currents vanish). According to Eqs. (2.15)-(2.16) and setting $z = 0$ at the boundary

$$\mathbf{E}_{i\parallel}e^{i\overbrace{(k_{i_x}x + k_{i_y}y)}^{\mathbf{k}_{i\parallel}}} + \mathbf{E}_{r\parallel}e^{i\overbrace{(k_{r_x}x + k_{r_y}y)}^{\mathbf{k}_{r\parallel}}} = \mathbf{E}_{t\parallel}e^{i\overbrace{(k_{t_x}x + k_{t_y}y)}^{\mathbf{k}_{t\parallel}}} \quad (2.17)$$

This must be true for all points on the interface so that $\mathbf{k}_{i\parallel} = \mathbf{k}_{r\parallel} = \mathbf{k}_{t\parallel}$, which is the phase-matching condition [3] and implies that the three wavevectors must lie in the same plane. Assuming that this is the x-z plane, the transverse component of any wavevector can be expressed as $\mathbf{k}_{a\parallel} = k_a \sin\theta_a$. From this last equality, the phase-matching condition and the fact that $k_i = k_r = k_1 = \omega\, n_1/c_0$ and $k_t = k_2 = \omega\, n_2/c_0$ [see Eq. (2.11)] we obtain Snell's laws of reflection and refraction

[3] by $\parallel$ and $\perp$ we mean tangential and normal component, respectively.

$$\begin{aligned} \theta_r &= \theta_i, & (2.18) \\ n_1 \sin\theta_i &= n_2 \sin\theta_t, & (2.19) \end{aligned}$$

regardless of the handedness of both media. The most important consequence of Eq. (2.19) is that when both media have refractive indices of opposite sign, the angle of refraction θ_t is negative (see Figure 2.2). Moreover, since the transmitted wave moves away from the interface (energy propagation) and n_2 is negative, $\mathbf{k}_{2\perp}$ must be directed towards the interface, *i.e.*, the normal component of the wavevectors at the interface of both media are antiparallel.

Focusing properties of NIMs

One of the consequences of negative refraction is the double-focus effect of a negative-index slab (index n_L) embedded in a RHM with index n_R (see Figure 2.3). Light rays coming from a point source at symmetric angles with respect to the normal meet at the same point (Focus 1) inside this lens. After exiting the slab, they meet again at a second point (Focus 2). Simple trigonometric considerations allow us to calculate the distance s as a function of the source separation from the lens l

Figure 2.3: Double focusing property of NIMs

$$s = l\,\frac{\tan\theta_R}{\tan\theta_L} \quad (2.20)$$

Snell's law gives us the value of the angle θ_L

$$\theta_L = \left| \arcsin \left(\frac{n_R}{n_L} \sin \theta_R \right) \right| \tag{2.21}$$

Since s depends on θ_L, which in turn depends on θ_R, we will have a different focal distance for each angle of incidence. This results in spherical aberration, as the image of a point is a circle. The only way to circumvent this problem is to use $n_L = -n_R$, which implies that $\theta_L = \theta_R$. In this case, $s = l$ and $t = d - l$. We must stress that this is not a lens in the classical sense, as it lacks an optical axis, *i.e.*, it is not able to focus parallel rays (source far away from the lens).

Reverse Goos-Hänchen effect

When a linearly polarized electromagnetic wave undergoes total internal reflection, it is slightly shifted along the normal direction. At the interface between two RHMs, $d > 0$. However, $d < 0$ at the interface between a RHM and a LHM (see Figure 2.4).[63] Recently, it has been shown that the inverse Goos-Hänchen effect could be used to stop light in an optical waveguide based on total internal reflection in which the core medium has a negative refractive index.[64] A straightforward application is the construction of optical memories, as well as the whole set of applications associated to slow-wave phenomena.

Other properties

Some other interesting properties of NIMs are the reversal of the Doppler effect and the Vavilov-Čerenkov radiation, the exchange in the behavior of concave and convex lenses,[60] or even the possibility of turning the Casimir force from attraction to repulsion and achieving quantum levitation.[65]

2.2   Applications

Throughout the short history of metamaterials — the only known means of building NIMs — scientists have found numerous applications of negative-index media.[66] Among them we find the construction of sub-wavelength optical waveguides[67], the design of low-weight antennas and reflectors,[68] and the improve-

(a)

$d > 0$

(b)

$d < 0$

Figure 2.4: Goos-Hänchen effect at the interface between (a) two right-handed media and (b) a left-handed medium and a right-handed medium.

ment of the magnetic resonance imaging technique.[69] Notwith-standing, there is one application that stands out from the rest and that we describe next.

Superlens

UNDOUBTEDLY, the most relevant application of NIMs is the possibility of building a so-called superlens.[2] It is well-known that the resolution of conventional lenses is limited by diffraction. This fact can be easily understood by using the angular-spectrum decomposition of the fields[70], with which we can express any field distribution $\mathbf{A}(x, y, z)$ as [4]

$$\mathbf{A}\left(x, y, z\right) = \int\limits_{-\infty}^{\infty} \int\limits_{-\infty}^{\infty} \hat{\mathbf{A}}\left(k_x, k_y, z\right) e^{ik_x x} e^{ik_y y} dk_x dk_y, \qquad (2.22)$$
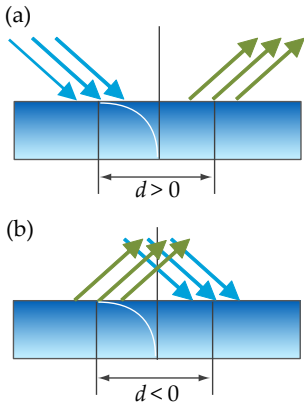
$$\hat{\mathbf{A}}\left(k_x, k_y, z\right) = \int\limits_{-\infty}^{\infty} \int\limits_{-\infty}^{\infty} \mathbf{A}\left(x, y, z\right) e^{-ik_x x} e^{-ik_y y} dx dy. \qquad (2.23)$$

Eq. (2.23) is the two-dimensional Fourier transform with respect to the spatial variables x and y. Thus, $k_x = 2\pi f_x$ and $k_y = 2\pi f_y$ are the angular spatial frequencies in each direction, with f_x and f_y being the spatial frequencies. On the other hand, if we assume that the fields are in the plane $z = 0$, Eq. (2.22) expresses the field as an infinite sum of plane waves of the form

$$\hat{\mathbf{A}}\left(k_x, k_y, 0\right) e^{i\left(k_x x + k_y y + k_z 0\right)}, \qquad (2.24)$$

which is known as the angular spectrum of $\mathbf{A}$. In addition, $\mathbf{A}$ must satisfy the wave equation Eq.(2.1), which becomes the Helmholtz equation for a time-harmonic variation of the fields

$$\nabla^2 \mathbf{A} + k^2 \mathbf{A} = 0. \qquad (2.25)$$

Upon substitution of Eq. (2.22) into Eq. (2.25) we find that the following equation must be fulfilled

$$\left(\frac{\partial^2}{\partial z^2} + \overbrace{k^2 - k_x^2 - k_y^2}^{k_z^2}\right) \hat{\mathbf{A}}\left(k_x, k_y, z\right) = 0 \qquad (2.26)$$

whose solution is given by

$$\hat{\mathbf{A}}\left(k_x, k_y, z\right) = \hat{\mathbf{A}}\left(k_x, k_y, 0\right) e^{ik_z z} \qquad (2.27)$$

[4] $\mathbf{A}$ may represent either the electric field $\mathbf{E}$ or the magnetic field $\mathbf{H}$.
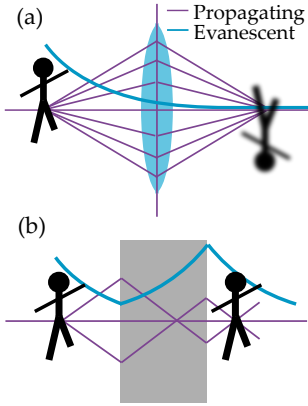
Figure 2.5: Imaging with two different kind of lenses (a) Conventional lens. Propagating waves are perfectly restored, while the information carried by evanescent waves is lost. The image is an inverted version of the object, like the images formed on our retina (it is our brain that put things in order). (b) Superlens (NIM slab). The image preserves the object orientation and no information is lost, that is, propagating and evanescent waves are restored.

[5] The coefficients for the **H** field and TM polarization are

$$t_{TM} = \frac{2\varepsilon_2 k_{z1}}{\varepsilon_2 k_{z1} + \varepsilon_1 k_{z2}}$$

$$r_{TM} = \frac{\varepsilon_2 k_{z1} - \varepsilon_1 k_{z2}}{\varepsilon_2 k_{z1} + \varepsilon_1 k_{z2}}$$

Note that, given a certain polarization, the coefficients are not the same for **E** and **H**, since both fields are related by the characteristic impedance, which is different in each medium (1 and 2).

Therefore, the effect of propagation over a distance z can be obtained by propagating each component of the angular spectrum that distance. Remarkably, the components of $\mathbf{A}(x, y, 0)$ with a spatial periodicity sma-ller than the wavelength λ have an associated plane wave with an imaginary propagation constant $k_z = 2\pi(1/\lambda^2 - f_x^2 - f_y^2)^{1/2}$, which is actually evanescent in the z direction. This is the reason why the finer details of an object (smaller than the wavelength) cannot be resolved by a far-field lens. Plane waves carrying the bulk features of the object propagate through space reaching the lens, while evanescent waves carrying the finer features exponentially decay as we move away from the source. Classical lenses are able to correct the phase delay that each angular-spectrum component accumulates with propagation, but cannot restore the amplitude of evanescent waves, which either do not reach the lens or are dramatically attenuated when they reach the focal point.

As seen above, a NIM slab also acts as a lens for rays. The big difference between conventional lenses and the NIM slab is that, in addition to restoring the phase of propagating waves, a medium with $n = \varepsilon = \mu = -1$ restores the amplitude of evanescent waves, which reach the focus with the same amplitude they had in the object plane. As a result, we obtain a perfect image reconstruction. This is the reason why this kind of lens has been termed *perfect lens* or superlens — there exists no perfect lens in practice. This apparent amplification of evanescent waves by a passive device does not violate energy conservation, as these waves do not carry energy. The amplification phenomenon is linked to the excitation of surface waves at the interface between the lens and the surrounding medium, known as surface plasmon polaritons (SPPs)[71,72] — see next section. Mathematically, the evanescent-wave amplification of a NIM slab of thickness d ($\varepsilon_N = \mu_N = -1$) embedded in air ($\varepsilon_a = \mu_a = 1$), can be explained by calculating the transmission coefficient of the whole system. For instance, for TE polarization, the Fresnel transmission and reflection coefficients for the **E** field when passing from a certain "medium 1" to other "medium 2" are [5]

$$t_{TE} = \frac{2\mu_2 k_{z1}}{\mu_2 k_{z1} + \mu_1 k_{z2}} \qquad r_{TE} = \frac{\mu_2 k_{z1} - \mu_1 k_{z2}}{\mu_2 k_{z1} + \mu_1 k_{z2}} \tag{2.28}$$

We denote the coefficients from air to the NIM by t and r, in

which case the subscript "1" has to be replaced by "a" and the subscript "2" has to be replaced by "N" in Eq. (2.28), while the coefficients from the NIM to air are denoted by t' and r', in which case the roles of the subscripts are interchanged. We have seen that for propagating waves, $k_{z,N} = -k_{z,a}$. However, for evanescent waves causality implies that $k_{z,N} = k_{z,a} = i(k_x^2 + k_y^2 - \varepsilon\mu\omega^2/c_0^2)^{-1/2}$, as both must decay in the direction of propagation. By summing the multiple scattering events, we can calculate the total transmission coefficient through both surfaces of the NIM slab:

$$T_{TE} = tt'e^{ik_{z,N}d} + tt'r'^2e^{3ik_{z,N}d} + tt'r'^4e^{5ik_{z,N}d} + \cdots = \frac{tt'e^{ik_{z,N}d}}{1 - r'^2e^{2ik_{z,N}d}} \tag{2.29}$$

By substituting the specific values of our system air-NIM-air in Eq. (2.29), we arrive at

$$\lim_{\substack{\varepsilon\to-1\\\mu\to-1}} T_{TE} = \lim_{\substack{\varepsilon\to-1\\\mu\to-1}} \frac{2\mu_N k_{z,a}}{\mu_N k_{z,a} + \mu_a k_{z,N}} \frac{2\mu_a k_{z,N}}{\mu_a k_{z,N} + \mu_N k_{z,a}} \frac{e^{ik_{z,N}d}}{1 - \left(\frac{\mu_a k_{z,N} - \mu_N k_{z,a}}{\mu_a k_{z,N} + \mu_N k_{z,a}}\right)^2 e^{2ik_{z,N}d}} = e^{-ik_{z,a}d},$$

$$\tag{2.30}$$

which means that evanescent waves are enhanced by the NIM slab [see Figure 2.5].[6] The first experimental superlens was fabricated and tested in 2005.[73] It consisted of a thin metallic layer and exploited the fact that electric and magnetic fields are not coupled in the quasi-static limit, in which only a negative permittivity is required to implement a near-field superlens.[2] For this reason, a simple Ag layer suffices to achieve sub-wavelength resolution. In this specific experiment a resolution of the order of $\lambda/6$ was attained. Evolution of superlenses gave rise to another very interesting kind of lens: the *hyperlens*. In brief, a hyperlens transforms evanescent components into propagating ones by magnifying the near field pattern, which can then be treated with conventional optics.[74,75] This way the resolution of our far-field system is improved by the magnification factor. Transformation optics has led to alternative hyperlens designs as we will see in next chapter.

[6] The same result is obtained for TM polarization.

2.3   Surface plasmon polaritons and extraordinary transmission

Since surface plasmon polaritons and extraordinary optical transmission (EOT) play a significant role in the underlying physics of the structures that we have designed with the aim of obtaining NIMs (see next section), we briefly describe both phenomena in this section. SPPs are hybrid electron-photon excitations that are trapped at the interface between a dielectric (positive-permittivity medium) and a conductor (negative-permittivity medium).[7] While SPPs can propagate along the conductor surface, they are evanescently confined in the perpendicular direction.[71,72,76] This property of SPPs allows us to concentrate electromagnetic fields at the nanoscale by using subwavelength metallic structures. A recent branch of optics known as plasmonics exploits this unparalleled light-concentration ability of metals for a wide range of applications.[72,77,78] These include the miniaturization of photonic circuits, modulators and photodetectors, the enhancement of non-linear phenomena, the realization of extremely sensitive biosensors, and the improvement of the efficiency of photovoltaic cells.

[7] Theoretically, SPPs could also exist at the interface between two media with permeabilities of opposite sign.

Case of study: SPPs at a planar interface

The best way to understand the physical nature of SPPs is by analyzing a simple mathematical example. To this end, we study here the geometry depicted in Figure 2.6, consisting of two semi-infinite spaces with permittivities ε_1 and ε_2 connected by a planar interface.

Figure 2.6: Excitation of an SPP at a planar interface
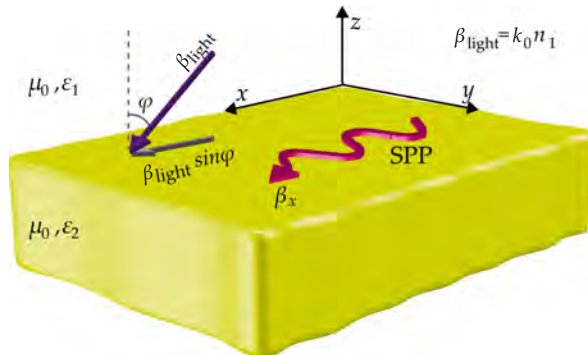
Given the symmetry of the problem, the field can only depend on the z-coordinate and a propagation term in the x-direction (we choose this propagation direction without loss of generality), since we seek a solution propagating along the interface of both media. Hence, the field will be of the form $\mathbf{E}(x, y, z) = \mathbf{E}(z)e^{i\beta_x x}$. In this case, the SPP wavevector is denoted by $\boldsymbol{\beta}$. It is possible to express the solutions to this system as a combination of TM (only E_x, E_z, and H_y are different from zero) and TE modes (only E_y, H_x, and H_z are different from zero). By inserting the previous expression of the field in Faraday's and Ampère's laws we arrive at the following relations for the fields

$$TM: \quad E_x = -i\frac{1}{\omega\varepsilon_0\varepsilon}\frac{\partial H_y}{\partial z}, \qquad E_z = -\frac{\beta_x}{\omega\varepsilon_0\varepsilon}H_y \qquad (2.31)$$

$$TE: \quad H_x = i\frac{1}{\omega\mu_0}\frac{\partial E_y}{\partial z}, \qquad H_z = \frac{\beta_x}{\omega\mu_0}E_y. \qquad (2.32)$$

For TM modes, the solutions of propagating waves confined to the interface — the ones we are looking for — have the form

$$H_y = A_1 e^{i\beta_x x}e^{|\beta_{z1}|z}, \qquad E_x = -iA_1\frac{|\beta_{z1}|}{\omega\varepsilon_0\varepsilon_1}e^{i\beta_x x}e^{|\beta_{z1}|z}, \qquad E_z = -A_1\frac{\beta_x}{\omega\varepsilon_0\varepsilon_1}e^{i\beta_x x}e^{|\beta_{z1}|z} \qquad (z < 0)$$
$$(2.33)$$

$$H_y = A_2 e^{i\beta_x x}e^{-|\beta_{z2}|z}, \qquad E_x = iA_2\frac{|\beta_{z2}|}{\omega\varepsilon_0\varepsilon_2}e^{i\beta_x x}e^{-|\beta_{z2}|z}, \qquad E_z = -A_2\frac{\beta_x}{\omega\varepsilon_0\varepsilon_2}e^{i\beta_x x}e^{-|\beta_{z2}|z} \quad (z > 0)$$
$$(2.34)$$

Finally, applying continuity of tangential components at the interface ($z = 0$) requires that $A_1 = A_2$ and $|\beta_{z2}|\varepsilon_1 = -|\beta_{z1}|\varepsilon_2$, which implies that ε_1 and ε_2 must be of opposite sign. Moreover, bearing in mind that H_y further has to fulfill the wave equation Eq. (2.25), it is demanded that

$$\beta_{z1}^2 = k_0^2\varepsilon_1 - \beta_x^2, \qquad \beta_{z2}^2 = k_0^2\varepsilon_2 - \beta_x^2 \qquad (2.35)$$

Combining the previous expressions with the equality $|\beta_{z2}|\varepsilon_1 = -|\beta_{z1}|\varepsilon_2$, we arrive at the dispersion relation of SPPs for TM modes

$$\beta_x = k_0\sqrt{\frac{\varepsilon_1\varepsilon_2}{\varepsilon_1 + \varepsilon_2}} \qquad (2.36)$$

Proceeding similarly for TE waves, we reach the condition $A_1(\beta_{z1} + \beta_{z2}) = 0$, which is only possible if $A_1 = A_2 = 0$. Therefore, there is no non-trivial solution for TE modes.
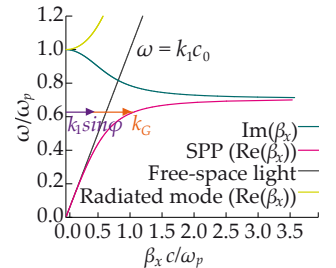
Figure 2.7: SPP dispersion relation.

In Figure 2.7 we have represented Eq. (2.36) for the case in which $\varepsilon_1 = 1$ and ε_2 is given by a low-loss Drude model. It is possible to express Eq. (2.35) in medium 1 as the equation of a circle, *i.e.*, $\beta_{z1}^2 + \beta_x^2 = k_0^2 \varepsilon_1 = k_1^2$. The values of β_x lying outside the circle are associated to an imaginary β_{z1} and thus correspond to evanescent solutions in the z-direction that are confined to the surface: this is the SPP. In contrast, values inside the circle are radiated modes. There exists a region in which β_x is purely imaginary, which represents a prohibited band. The wavenumber of free-space light in medium 1 is $\beta_{light} = k_1$. Therefore, the real part of β_x lying to the right of the light line ($\omega = k_1 c_0$) corresponds to the SPP, while the part lying to the left corresponds to a radiated mode. The projection along the interface of the momentum $\beta_{light} \sin \phi$ of photons impinging at an angle ϕ to the surface normal is always smaller than the SPP propagation constant β_x, even at grazing incidence, prohibiting phase-matching between the incoming light and SPPs. Hence, SPPs in an ideal semi-infinite medium are nonradiative in nature, *i.e.*, cannot decay by emitting a photon and, conversely, light incident on an ideal surface cannot excite SPPs. Thus, special phase-matching techniques to enhance the momentum of incident light such as grating or prism coupling are required for their excitation. For instance, this mismatch in wave vector can be overcome by periodically patterning the metal surface with grooves or holes with lattice constant a. For the simple case of a one-dimensional grating, phase-matching takes place whenever the condition $\beta_x = \beta_{light} \sin \phi \pm n k_G$ is fulfilled, where $k_G = 2\pi/a$ is the reciprocal vector of the grating, and $n \in \mathbb{N}$. The reverse process also takes place, and so SPPs propagating along a surface modulated with a grating can couple to light and thus radiate. These coupling and decoupling mechanisms play a key role in the onset of extraordinary optical transmission, an astonishing experimental result related to anomalous light transmission through sub-wavelength aperture arrays drilled in optically thick metallic films that was unveiled by T. Ebbesen and coworkers in 1998.[79]

According to Bethe's theory, the transmission efficiency (normalized to the aperture area) of a single hole milled in an infinitely thin perfect conductor scales as $(r/\lambda)^4$, where r is the hole radius and λ the incoming light wavelength.[80] Therefore,

we would expect very low transmission efficiencies in subwavelength apertures due to the poor coupling of subwavelength holes to radiative electromagnetic modes. However, subwavelength aperture arrays exhibit transmission efficiencies that exceed unity at wavelengths at which the incoming radiation can only tunnel through the apertures in the transmission process. This effect has been attributed to the excitation of SPPs at the input metal surface thanks to the periodicity of the grating. The energy collected by the SPP is able to evanescently tunnel through the holes and excite SPPs at the output metallic surface, which is finally reradiated to free space.

2.4   Our contribution (I): Towards low-loss NIMs in the visible

As mentioned in the introduction, it would be very important to have at our disposal NIMs operating in the visible range, where we can take full advantage of their properties. For instance, the superior imaging ability of NIMs would be essential for visible microscopy, with applications in microelectronics, bio- and nano-technology. However, at the time of beginning this thesis, experimental results in this regard were not promising due to the bad performance in terms of losses of the fabricated NIMs that were designed to exhibit a negative index in the visible spectrum, as can be seen in Table 2 of PAPER3, which shows the state of the art in NIMs at visible wavelengths. The maximum FOM[8] achieved in those experiments was around 0.7, which is associated with high losses. Other desired features such as multilayer homogeneous structures or polarization independence were not attained either.

In this sense, our contribution starts from the study of the relation between the phenomenon of extraordinary transmission and negative-index media, which was motivated by the similarity between the structures supporting each effect. This analysis (performed in PAPER1) gave as a deeper general knowledge concerning the design of NIMs in which — in our view — EOT plays a role and, in particular, about the so-called fishnet structure,[41,42] one of the most promising NIMs due to its superior performance in several aspects and different frequency regimes.[81,82] As a result of this study, we realized that it is pos-

[8] The figure of merit (FOM) is a standard loss measure defined as FOM = $|n'/n''|$, where $n = n' + in''$ is the refractive index. Low losses are usually attributed to values above 3[81]

sible to exploit certain aspects of the fishnet that had been overlooked so far, which enabled us to design a multilayer (showing homogeneous behavior in the propagation direction), polarization-independent, and loss-loss NIM (FOM higher than 4) in the visible spectrum. The main results are included in PAPER2. Our work in this field concludes with an experimental verification of this theoretical proposal that is described in PAPER3. In addition, a similar experiment performed at millimeter waves allowed us to verify the backward-wave nature of the first two propagation bands of the above-mentioned structure from direct phase measurements, which are very difficult to perform in the visible range (PAPER4).

2.5

PAPER 1. NEGATIVE REFRACTIVE INDEX METAMATERIALS AIDED BY EXTRAORDINARY OPTICAL TRANSMISSION

Negative refractive index metamaterials aided by extraordinary optical transmission

C. García-Meca, [*] **R. Ortuño, F. J. Rodríguez-Fortuño, J. Martí, and A. Martínez**

Nanophotonics Technology Center, Universidad Politécnica de Valencia, Camino de Vera s/n
46022, Valencia, Spain
[*]*cargarm2@ntc.upv.es*

ABSTRACT

We study under which conditions extraordinary optical transmission (EOT) structures can be used to build negative refractive index media. As a result, we present a metamaterial with superimposed EOT and negative index at visible wavelengths. The tailoring process starting from a simple hole array until achieving the negative index is detailed. We also discuss the so-called fishnet metamaterial (previously linked to EOT) under the same prism. Using the ideas put forward in this work, other structures with negative index could be engineered in the optical or visible spectrum.

1. Introduction

Nowadays, periodic sub-wavelength particle and hole arrays constitute a wide research field within nanophotonics [1]. Two of the most sought after phenomena based on these structures are extraordinary optical transmission (EOT) and negative refraction. The former arises from the coupling from incident light to Surface Plasmon Polaritons (SPPs) in a drilled metallic sheet, where light undergoes an enhanced transmission, higher than that predicted for a single hole in a perfect conductor [2]. The second effect, negative refraction, is directly related to metamaterials, which gain their properties from their shape rather than from their composition and provide a way to attain optical negative refractive index media (NIM) [3,4]. Usually, both phenomena have been treated separately except for some few cases in which the NIM behavior of the known fishnet structure was linked to EOT [5,6]. In this work, we generalize the relation between EOT and NIMs showing that sometimes it is desirable to have the former in order to achieve the latter. From now on and for the sake of brevity, we will refer to this phenomenon as NEOT (Negative refractive index Extraordinary Optical Transmission).

2. Theoretical remarks

Let us begin with some considerations on EOT so as to motivate our exposition. First, in order to unify criterions, we will consider (as usual) that EOT takes place when the normalized transmission T_n exceeds unity, being T_n defined as $T_n = (P_{out}/P_{in})(A_{ucell}/A_{hole}) = T(A_{ucell}/A_{hole})$, where A_{ucell} is the area of the unit cell, A_{hole} is the area of a single hole and P_{in}

and P_{out} are, respectively, the input and output electromagnetic power. On the other hand, there exist a number of structures that lead to the EOT phenomenon. They mainly differ in the shape of the holes and the type and thickness of the metal that constitutes the film in which they are pierced. However, if we regard an EOT structure as a homogeneous medium, we can model it with effective electric permittivity $\varepsilon = \varepsilon' + i\varepsilon''$ and magnetic permeability $\mu = \mu' + i\mu''$, whatever features it may have. We will limit ourselves to study normal incidence with the impinging wave oriented as in Figs.1 and 3. Thus, despite the tensorial character of ε and μ, the retrieval of their relevant components for that direction can be considered as a scalar problem. Simple EOT structures (made up of one metal layer) normally act as a dilute metal and exhibit a weak magnetic response. This means that their permittivity is negative at frequencies below that of the first EOT peak (and possibly below other EOT peaks) and that their permeability is small and positive (unless otherwise stated, when talking about permittivity, permeability, impedance or refractive index we refer to their real part). For instance, in the structures analyzed below, μ' is between 0.5 and 0.8 from DC to beyond the first EOT peak frequency. Nonetheless, when the transmission T (not normalized) is close to one, as it usually happens in EOT peaks, the equivalent medium must be impedance-matched to air, *i.e.*, the real part of its equivalent characteristic impedance $z = z' + iz''$ has to be $z' = \mathrm{Re}\{(\mu/\varepsilon)^{1/2}\} \approx 1$. As a consequence, the resonances with high T tend to present positive values of ε' similar to those of μ' (provided that ε'' and μ'' are negligible). In other words, the metal film, which has a highly negative ε' in bulk, exhibits positive ε' frequency regions when drilled, where the transmission is enhanced. In order to achieve a low-loss NIM, it is necessary to have $\varepsilon' < 0$ and $\mu' < 0$ [7]. Owing to the continuity of the constitutive parameters, ε' takes small negative values and crosses zero at frequencies right below the resonance because it is negative at lower frequencies as we mentioned above. Hence, we already have the first condition ($\varepsilon' < 0$) below the EOT peak spectral location. We are interested in this moderately negative ε' region with the aim of obtaining an impedance-matched NIM band, since the negative values of μ' that can be typically achievable artificially are small, especially in the visible regime. Finally, if we could insert a magnetic resonance in this region with μ' taking negative values, we would fulfill the second condition. Our argument can be summarized as follows: pick an EOT structure and modify it in order to introduce a magnetic resonance at a frequency slightly lower than that of the EOT peak, where ε' is still negative. Of course, this modification must not significantly alter the electric response of the medium in the working region. *A priori*, it may seem complex to do this, but next, we present a couple examples.

3. NEOT structures

Consider a simple array of cylindrical holes pierced in a metal film as starting point, with periodicities $a_x = 500$ nm, $a_y = 330$ nm, a hole radius $r = 110$ nm, and a film thickness $t = 130$ nm [Fig. 1(a)]. To obtain the transmission T and reflection R spectra of this structure, we simulate a unit cell with periodic conditions along the dimensions normal to propagation.

All numerical calculations are performed using commercial software (CST MICROWAVE STUDIO). Due to its low loss in the range of interest, we choose silver to be the film metal. The plasma frequency for silver is ω_p = 1.37×10^{16} s^{-1}. In general, the collision frequency ω_c is highly influenced by the structure geometry and roughness [8]. Nevertheless, in order to be able to compare our results with previous works, we will assume that ω_c = 8.5×10^{13} s^{-1}. This value of ω_c is more than twice as higher as that in bulk [9]. The effective index of refraction $n = n' + in''$ and impedance of the medium are retrieved from the calculated T and R using the conventional extraction method [10]. Then, ε and μ are obtained as $n = (\varepsilon\mu)^{1/2}$ and $z = (\mu/\varepsilon)^{1/2}$.

(a)　　　　　　　　　　　　　　(b)
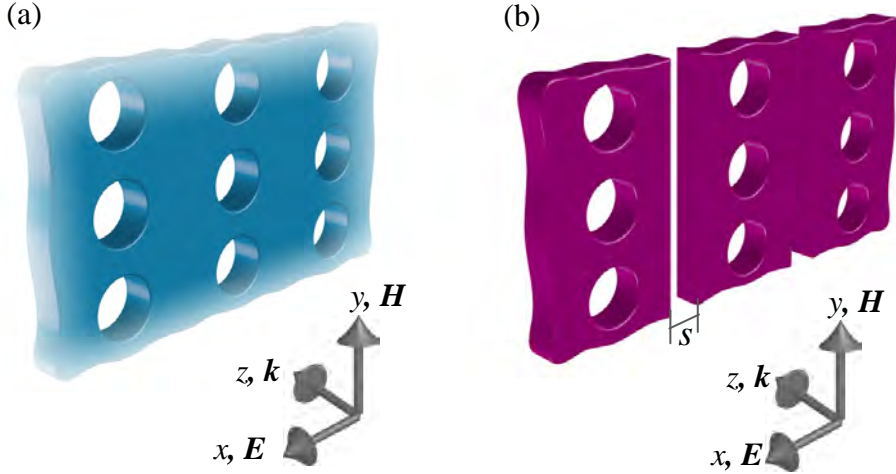
Fig. 1. (a) Silver periodic hole array exhibiting EOT. (b) NEOT structure resulting from adding slits to the structure in (a).

The normalized transmission spectra T_n of the above-mentioned hole array is depicted in Fig. 2(a), where we see two EOT peaks. They can be identified with the even and odd modes of the first plasmonic resonance, which splits into two, due to the coupling between the SPPs excited at both metal-air interfaces of the silver sheet [11]. In Fig. 2(b), it can be seen that z' is near unity where the transmission reaches its maximum, as mentioned before. In addition, the permittivity takes small negative values at frequencies lower than those at which the two resonances are located, mainly near the first one [blue line in Fig. 2(c)], whose maximum transmission is T = 0.95. This is the situation that we were searching for. The next step is to introduce magnetic activity at wavelengths slightly higher than that of the resonance. To this end, we propose a modification of the structure in Fig. 1(a) that consists of adding slits in the manner shown in Fig. 1(b). The reason is that it exhibits a magnetic resonance owing to the anti-symmetric mode induced by the incident H field, which generates currents flowing in opposite directions at both sides of the slits, similar to those of the metamaterial studied in [12]. These currents have a resonant nature and are going to give rise to a negative μ'

band at frequencies higher than the resonance frequency. Carefully choosing the slit width s, this magnetic resonance including a negative μ' region appears right below the spectral position at which the first EOT peak takes place, where ε' is still negative.
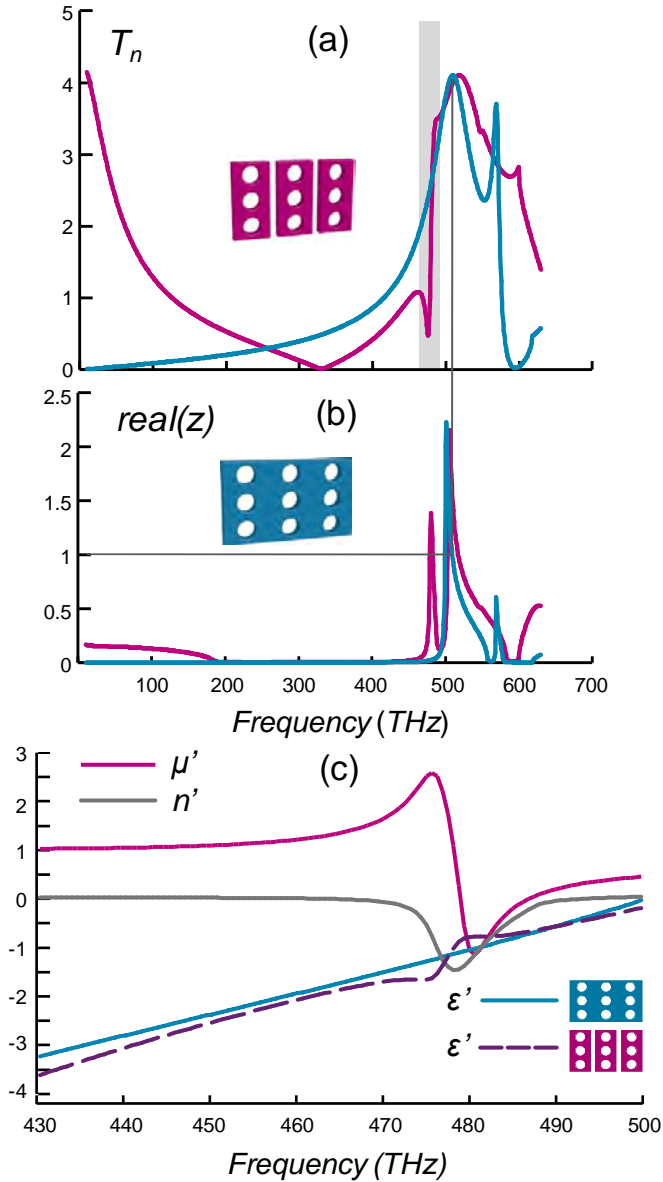
Fig. 2. (a) Normalized transmission of the structures depicted in Fig. 1(a) (blue) and Fig. 1(b) (magenta). (b) Real part of z for both structures (correspondence by color). (c) Comparison of effective ε' for the hole array with (dashed purple) and without slits (solid blue). Retrieved μ' (magenta) and n' (grey) of the hole array with slits [NEOT structure in Fig 1(b)].

In this case $s = 30$ nm and all other dimensions (a_x, a_y, t and r) are the same as before. The addition of the slits strongly modifies the hole array DC response. This is because the slits support a TEM mode without cutoff frequency and allow for a large transmission at high wavelengths. However, the values of T and R are very similar to those obtained before the modification in the region of interest [see Fig. 2(a)]. Even more important is the fact that the permittivities of the EOT and NEOT media are very similar within this band [see Fig. 2(c)]. The extracted part of μ' for the NEOT structure, together with its index of refraction are also shown in Fig. 2(c). We can see that the slits create a negative index band exhibiting EOT as expected. Note that if we had inserted the magnetic resonance at lower frequencies, the impedance mismatch would have reduced the transmitted power, since ε' would have been much more negative than μ'. That is why it is better to place the magnetic resonance close to the EOT one. As usual, we can model the losses through the figure of merit (FOM), defined as FOM = $|n'/n''|$.
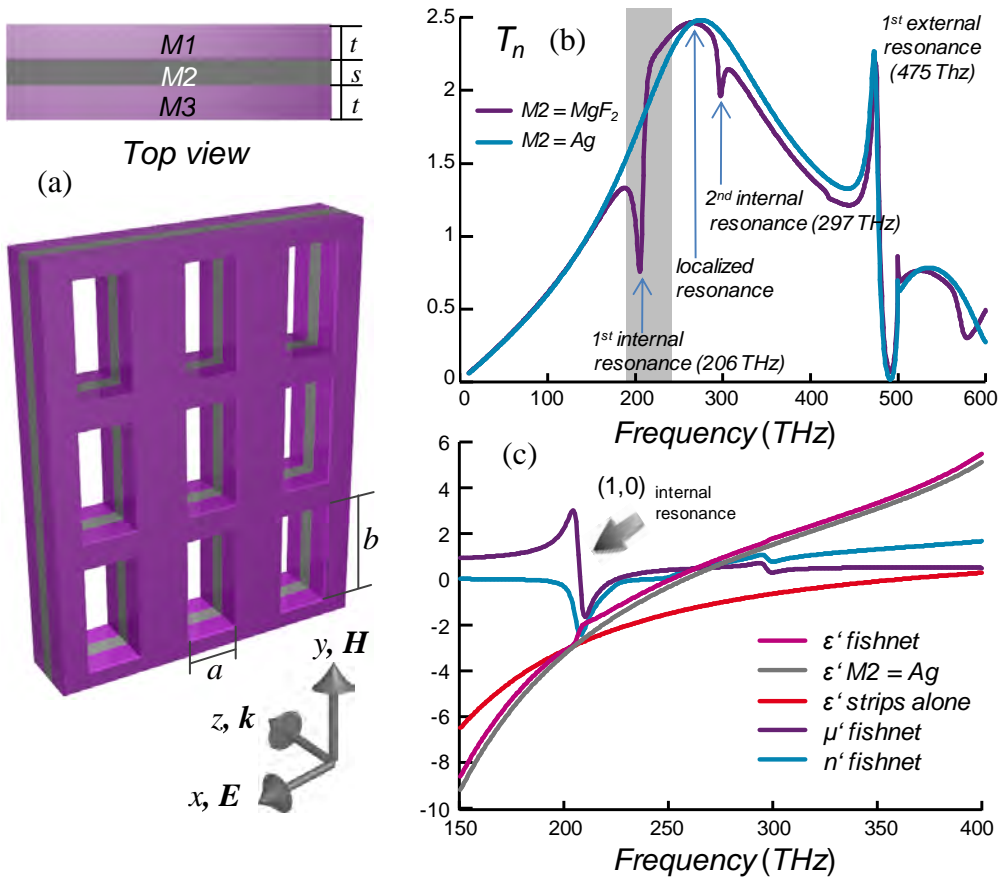
Fig. 3. (a) 3-layer metamaterial. (b) Normalized transmission with M2 = MgF$_2$ (purple) and M2 = Ag (blue). NEOT region in grey. (c) Fishnet ε' (magenta). ε' of structure in (a) with M2 = Ag and fishnet dimensions (grey) and with b=600 nm, *i.e.*, only horizontal strips (red). Fishnet μ' (purple) and n' (blue).

In this case, the FOM is approximately 2.5, which is quite good for this part of the spectrum. Moreover, it could be better, since ω_c might be lower in practice. For instance, the FOM is around 6 when $\omega_c = 4\times10^{13}$ s^{-1}, a value somewhat higher than the one that can be found in [9]. Further optimization of this structure could also improve its figure of merit.

The structure that we have just studied is not the only NEOT medium. For instance, the fishnet structure is also a very good example of the ideas presented in section 2. Basically, this metamaterial is a rectangular hole array perforated in a metal-dielectric-metal 3-layer structure [Fig. 3(a)]. To analyze it, we can take for instance the dimensions and materials employed in [13], which give a negative n' at telecommunication wavelengths: t = 45 nm, s = 30 nm, a = 284 nm, b = 500 nm, and a lattice constant $l_x = l_y = l =$ 600 nm. The material M1 is silver and M2 is MgF$_2$, whose refractive index is n = 1.38. It was only very recently that the true mechanisms giving rise to the negative refractive index of the fishnet structure were elucidated [6] and, as in the previous example, it is possible to show that its NIM behaviour can be derived from a simple EOT structure, resulting from replacing MgF$_2$ by Ag. Thus, this time the starting point is the rectangular hole array of Fig. 3(a) with M1 and M2 being silver. Its normalized transmission is shown in Fig. 3(b). Again we have two EOT peaks. The high frequency one, next to Wood's anomaly, corresponds to the first external SPP resonance and plays no role in achieving a negative n'. The other one, centred at 274 THz, is a localized resonance which occurs at the cutoff frequency of the holes [6]. This will be the high T peak that we demanded in the previous section. Figure 3(c) shows ε' for this hole array. There is almost no difference with the permittivity of the fishnet metamaterial. This fact indicates that the electric response arises from the interaction of the field with the holes and the external surfaces rather than just from the strips parallel to E. The value of ε' generated by these strips alone is also depicted in Fig. 3(c). Again, we will focus on the small negative ε' spectral region next to the peak maximum. Obviously, the modification for this structure so as to introduce a magnetic resonance is the insertion of a dielectric layer inside the silver film (making M2 to be MgF$_2$), that results in a milled MIM (metal-insulator-metal) structure. The electromagnetic modes supported by MIM composites (without holes) have already been studied and it is well-known that internal or gap SPPs appear at the inner metal-dielectric interfaces [14]. In [6,14] it is shown that similar modes are also excited in the fishnet metamaterial. Since the parallel momentum must be conserved, light can couple to internal SPPs when $k_{SPP} = k_0 \sin\theta + iG_x + jG_y$, with $G_x = G_y = 2\pi/l$. For this fishnet configuration and normal incidence ($\theta = 0$), three internal SPP resonances are excited within the frequency range of Fig. 3(b), corresponding to (i,j) equal to (1,0), (1,1) and (2,0) at 206, 297 and 422 THz, respectively. The (2,0) resonance is hardly excited and can roughly be seen in Fig. 3. The (1,0) internal resonance originates currents flowing in opposite directions at each of the Ag layers, generating a negative μ' band in the target negative ε' region. As we mentioned, the insertion of the dielectric does not affect the electric response and consequently a negative n' band appears. This is how a NIM is

created from our simple hole array exhibiting EOT. Note that in the case of the structure in Fig. 1(b) we did not employ the localized resonance associated with the cutoff frequency of the holes, which is out of the considered spectral region, but an SPP based resonance. This gives a general character to the ideas described in section 2, where we just demand the existence of a high transmission peak regardless of its physical nature. It is irrelevant whether the peak comes from a Fabry-Perot, shape or SPP resonance as long as its transmission (not normalized) is close to one (and the transmission is small at lower frequencies in such a way that ε' is negative, which is usually the case when dealing with metallic composites). The generation of the magnetic activity by introducing slits also differs from the way it is achieved in the fishnet. As seen, there exist several possibilities for building NEOTs playing with different kinds of EOT peaks and magnetic resonances. This point of view offers a wider perspective when it comes to obtain a NIM with the aid of extraordinary transmission structures. For instance, we could have designed the fishnet in order to use the SPP resonance instead of the localized one, other magnetic resonance source, or any combination that one could think of. The shaded regions in Figs. 2 and 3 correspond to the spectral range where EOT and the negative index occur simultaneously, that is, the NEOT region. Although usually unnoticed, the existence of EOT in the fishnet thanks to the above-mentioned localized resonance is very important in order to achieve a low reflectivity. Otherwise, the equivalent plasma frequency of this structure, and thus the impedance mismatch, would be much higher.

4. Conclusions

In summary, we have shown that EOT structures allow for the creation of negative refractive index composites by taking advantage of high transmission peaks, as long as it is possible to modify the structure in order to create magnetic activity at frequencies slightly lower than those of the peaks. This is the case of the fishnet metamaterial, in which a magnetic resonance exhibiting negative permeability is generated in the proximity of a high T localized resonance. In addition, we have presented a structure with superimposed extraordinary transmission and negative index of refraction at visible frequencies. Although based on the same ideas, the physical origin of EOT and the magnetic activity in the proposed structure is different from the fishnet one, supporting the generality of the described procedure, which opens up the way for building new NEOT structures at optical wavelengths.

Acknowledgements

References

1. F.J. García de Abajo, "Colloquium: Light scattering by particle and hole arrays," Rev. Mod. Phys. **79**, 1267-1290 (2007).
2. C. Genet and T.W. Ebbesen, "Light in tiny holes," Nature **445**, 39-46 (2007).
3. V. M. Shalaev, "Optical negative-index metamaterials," Nature Photonics **1**, 41-48 (2006).
4. C. M. Soukoulis, S. Linden, and M. Wegener, "Negative refractive index at optical wavelengths," Science **315**, 47-49 (2007).
5. M. Beruete, M. Sorolla, M. Navarro-Cía, F. Falcone, I. Campillo, and V. Lomakin, "Extraordinary transmission and left-handed propagation in miniaturized stacks of doubly periodic subwavelength hole arrays," Opt. Express **15**, 1107-1114 (2007).
6. A. Mary, S. G. Rodrigo, F. J. García-Vidal, and L. Martín-Moreno, "Theory of negative-refractive-index response of double-fishnet structures," Phys. Rev. Lett. **101**, 103902 (2008).
7. R. A. Depine and A. Lakhtakia, "A new condition to identify isotropic dielectric-magnetic materials displaying negative phase velocity," Microwave Opt. Technol. Lett. **41**, 315-316 (2004).
8. V. P. Drachev, U. K. Chettiar, A. V. Kildishev, Y. Hsiao-Kuan, W. Cai, and V. M. Shalaev, "The Ag dielectric function in plasmonic metamaterials," Opt. Express **16**, 1186-1195 (2008).
9. P. B. Johnson and R. W. Christy, "Optical constants of the noble metals," Phys. Rev. B **6**, 4370-4379 (1972).
10. X. Chen, T. M. Grzegorczyk, B. Wu, J. Pacheco, Jr., and J. A. Kong, "Robust method to retrieve the constitutive effective parameters of metamaterials," Phys. Rev. E **70**, 016608-016614 (2004).
11. L. Martín-Moreno, F. J. García-Vidal, H. J. Lezec, K. M. Pellerin, T. Thio, J. B. Pendry, and T. W. Ebbesen, "Theory of Extraordinary Optical Transmission through Subwavelength Hole Arrays," Phys. Rev. Lett. **86**, 1114 (2001).
12. C. García-Meca, R. Ortuño, R. Salvador, A. Martínez, and J. Martí, "Low-loss single-layer metamaterial with negative index of refraction at visible wavelengths," Opt. Express **15**, 9320-9325 (2007).
13. G. Dolling, C. Enkrich, M. Wegener, C. M. Soukoulis, and S. Linden, "Low-loss negative-index metamaterial at telecommunication wavelengths," Opt. Lett. **31**, 1800-1802 (2006).
14. R. Ortuño, C. García-Meca, F.J. Rodríguez-Fortuño, J. Martí, and A. Martínez, "Role of surface plasmon polaritons on optical transmission through double layer metallic hole arrays," Phys. Rev. B (to be published).

2.6

PAPER2. DOUBLE-NEGATIVE POLARIZATION-INDEPENDENT FISHNET METAMATERIAL IN THE VISIBLE SPECTRUM

Double-negative polarization-independent fishnet metamaterial in the visible spectrum

C. García-Meca, [*] **R. Ortuño, F. J. Rodríguez-Fortuño, J. Martí, and A. Martínez**

Nanophotonics Technology Center, Universidad Politécnica de Valencia, Camino de Vera s/n
46022, Valencia, Spain
[*]*cargarm2@ntc.upv.es*

ABSTRACT

We show that a second-order magnetic resonance present in the fishnet metamaterial can be enhanced so as to achieve simultaneous negative permittivity and permeability in the visible range. The double negative behavior leads to reduced losses in this particular fishnet metamaterial. We also study the stacking of several functional layers, verifying the convergence of the refractive index.

Over the past decade, metamaterials have awakened a great interest thanks to their potential to expand the range of electromagnetic properties found in natural media. One of these properties is negative refraction, which was first experimentally demonstrated in microwave frequencies [1]. Since then, much effort has been put in extending negative refraction to the visible spectrum [2]. The so-called fishnet metamaterial (FMM) is a strong candidate for attaining a negative refractive index n ($n = n' + in''$) in this range. In fact, negative refraction was recently observed in a ten-functional-layer FMM design at telecommunication wavelengths [3]. To our knowledge, the only fishnet designs operating in the visible exhibited a negative n' band around 780 nm, in the limit with the IR spectrum [4,5]. The main drawback in this case was that μ' did not reach negative values and, consequently, the negative n' came from the existence of high losses ($\varepsilon = \varepsilon' + i\varepsilon''$ and $\mu = \mu' + i\mu''$ are the medium permittivity and permeability). Thus the question remains whether it is possible to engineer the FMM in order to achieve a metamaterial with simultaneous negative ε' and μ' at such high frequencies, with the subsequent loss decrease (in [5] $\varepsilon'<0$ and $\mu'<0$ occurred at 813 nm). In this Letter, we show a way to reach this goal by using a second magnetic resonance present in the FMM, different from the one that is usually exploited.

In Fig. 1 we show an FMM illustration. It consists of $2N+1$ alternating metal (m) and dielectric (d) stacked hole arrays resulting in N functional metamaterial layers (N=1 corresponds to m-d-m, N=2 to m-d-m-d-m,...). Here we have considered rectangular holes, although other shapes could be valid as well. Regarding the structure materials, silver has been the chosen metal owing to its low loss in the visible range, since we aim to work

in this part of the spectrum. In addition, we have considered a dielectric permittivity $\varepsilon_d =$ 2.4, such as the one of some solidifiable photopolymers [6].
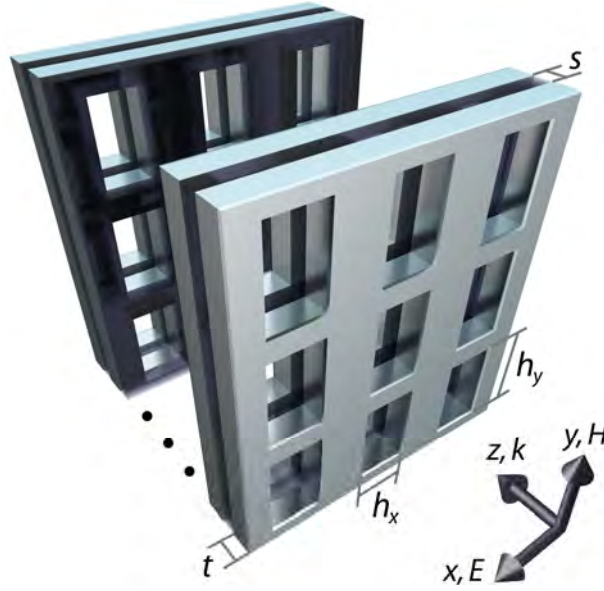
Fig. 1. Multilayer FMM. The metal and dielectric thicknesses are t and s. The periodicities in x and y are a_x and a_y.

To obtain the FMM electromagnetic response, commercial software (CST Microwave Studio) has been used, utilizing the Drude model for silver with $\omega_p = 1.37 \times 10^{16}$ s^{-1} and $\omega_c = 8.5 \times 10^{13}$ s^{-1}. We have restricted ourselves to normal plane wave incidence. To retrieve the effective parameters [7], the sum of the widths of each layer has been taken as the cell size a_z in the z direction, to be consistent with the $N > 1$ general case.

Usually, the FMM magnetic response is ascribed to the excitation of a virtual current loop between the strips parallel to the incident magnetic field H. If these currents are strong enough, they can counteract the mentioned incident H field and give rise to a resonance exhibiting negative μ'. The strategy followed in other works with the purpose of attaining a negative n' in the visible spectrum was to push this resonance to higher frequencies by miniaturizing the FMM dimensions [4]. Unfortunately, the strength of this magnetic resonance at visible frequencies was quite low and the negative μ' band disappeared. Nevertheless, a negative n' was achieved due to the high loss at the resonance (strictly, the condition to obtain a negative n' is: $\varepsilon''\mu'+\mu''\varepsilon'<0$ [8]). Indeed, the losses, which are usually estimated through the figure of merit (FOM = $|n'/n''|$), were quite high in this case, with a low FOM = 0.5. Despite the fact that the addition of more metamaterial layers has proven to enhance the magnetic resonance strength [3] (it can even reach negative values), in this case the FOM obtained for the multilayer

configuration hardly exceeds unity. Recently, it was shown that the above-mentioned current loop is generated by an internal or gap surface-plasmon polariton (SPP) mode flowing through the inner metal-dielectric interfaces of the structure [9,10]. Impinging light can couple to this SPP mode through the holes when the parallel momentum provided by the periodicity equals that of the SPPs. Therefore, there exists not only one internal resonance but several of them [10] that could be potentially excited at the frequencies that meet the condition $k_{spp} = k_0 \sin\phi + iG_x + jG_y$, with $G_x = 2\pi/a_x$ and $G_y = 2\pi/a_y$ (for normal incidence, $\phi = 0$). In fact, it can be shown that by enlarging h_x, the resonance corresponding to $(i,j) = (1,0)$ becomes weaker and weaker, and the opposite happens to the $(1,1)$ resonance, which increases its strength reaching negative μ', since it also generates antiparallel currents that oppose the **H** field at certain wavelengths. It could be natural to use this second magnetic resonance to achieve a negative μ' band in the visible spectrum, since it occurs at higher frequencies than the first one. In Fig. 2 we can see how the two first magnetic resonances change when varying h_x for the dimensions of a FMM design originally operating at telecommunication frequencies [11].
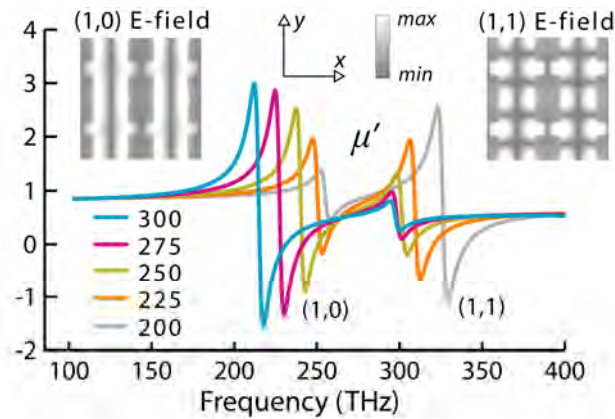
Fig. 2. Evolution of μ' as a function of h_x for an FMM with $N = 1$, $s = 30$ nm, $t = 45$ nm, $a_x = a_y = 600$ nm, $a_z = 120$ nm, $h_y = 500$ nm and, exceptionally, $\varepsilon_d = 1.9$ as in [4]. Legend, h_x in nm. Insets, $|E|$ in the gap.

As mentioned before, the higher the h_x is, the stronger the second magnetic resonance is. This feature of the FMM is also advantageous in the sense that it allows us to make the structure polarization independent, demanding that $h_x = h_y = h$, as this hole aspect ratio is enough to enhance the $(1,1)$ magnetic resonance sufficiently. Figure 2 insets show the **E** field profiles between metals. Clearly the $(1,0)$ mode has no variation in y while the $(1,1)$ mode presents two nodes per period as corresponds to their pure gap-SPP counterparts [10]. On the other hand, the structure's ε' is mainly governed by the interaction of the field with the external metallic surfaces, so it is controlled through the holes size and periodicity. Basically, the equivalent plasma frequency of the medium is dominated by

the cutoff wavelength of the holes λ_c, since at this wavelength, at which a high transmission localized resonance takes place, ε' is slightly higher than zero. Taking all these things into account, what we should do is to place λ_c in the desired visible spectral region and the (1,1) resonance at wavelengths right above λ_c, where ε' is going to be negative [12]. To this end, we can first determine the hole size of a one-metal-layer hole array for a certain target λ_c [13]. We do not need to consider the three-layer fishnet structure yet, because its electric response is very similar to that of the one-metal-layer hole array [12]. For instance, $h = 225$ nm gives $\lambda_c = 535$ nm. Next, we need to choose the proper thickness of the silver and dielectric layers to locate the second magnetic resonance at a wavelength somewhat higher than λ_c. Both the internal and external SPP modes appearing in the FMM are very similar to those of the same structure without holes, *i.e.*, three alternating metal-insulator-metal (MIM) sheets surrounded by air. The modes supported by MIM sheets have analytical expressions and, to a first approximation, they can be used to model the FMM [10,14]. In Fig. 3 we have depicted the SPP modes dispersion relation of a MIM structure with $t = 36$ nm and $s = 32$ nm. Recalling the coupling condition from light to SPPs, we find that for a periodicity of $a_x = a_y = 360$ nm, the (1,0) and (1,1) resonances associated with the internal SPP mode are excited at 332 and 458 THz, respectively.
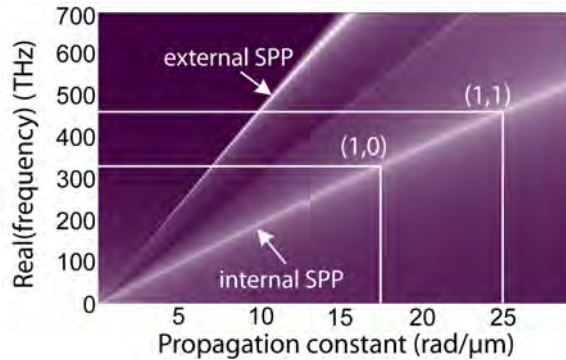
Fig. 3. SPP dispersion relation of a MIM structure with $t = 36$ nm and $s = 32$ nm.

Numerical simulations reveal that they really appear at 350 and 450 THz (857 and 667 nm), in good agreement with the simplified model predictions. In Fig. 4 we show the extracted ε', μ' and n', the FOM, and the absorption $A = 1-T^2-R^2$ (the inset shows the transmission T and reflection R spectra) of an FMM with the previous dimensions, where we can clearly observe the two magnetic resonances. Negative values of ε' and μ' are achieved around 660 nm (red light) and consequently a negative n'. Even though the (1,1) mode occurs at a frequency 100 THz higher, at the FOM maximum A is the same for both modes. In addition, the (1,1) mode FOM is three times the (1,0) one, supporting that, for the polarization independent configuration, the (1,1) mode is more adequate to obtain a low loss optical medium with $n' < 0$.
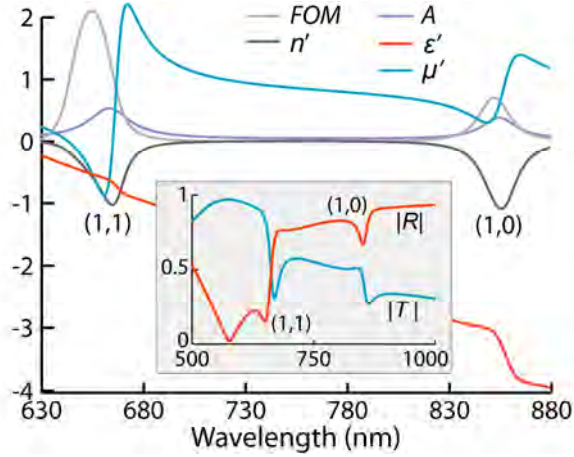
Fig. 4. *A*, FOM, ε', μ' and n' for an FMM with $N = 1$, s = 32 nm, $t = 36$ nm, $a_x = a_y = 360$ nm, $a_z = 400$ nm, and $h = 225$ nm. Inset, corresponding T and R.

Although it is worth studying one metamaterial layer as a starting point because it usually gives an approximate idea of the bulk properties and simplifies the problem, it is necessary to consider the effect of stacking several functional layers whose mutual interaction could influence the effective metamaterial behavior. The chief effect when stacking multiple FMM layers is the blue-shift undergone by the magnetic resonances, while its electric response is hardly altered. This must be taken into account when designing multilayer structures, since the frequency of the negative μ' band generated by the (1,1) resonance could surpass the metamaterial effective plasma frequency, losing the negative n'. In other words, the magnetic resonances of the initial one-layer design must be lowered in frequency. According to the MIM structure dispersion relation, this can be done, for example, by reducing the metal or dielectric layers thickness or by increasing the dielectric permittivity. In Fig. 5 we depict the evolution of n' as a function of N for an FMM configuration designed with these considerations in mind. The convergence to a final value within the visible spectrum is observed. The FOM for the $N = 9$ case is also depicted. It reaches a maximum value of 4.2, which is quite high for the visible range. Following the previous steps, the metamaterial can be engineered to present negative n' in other visible spectral regions. Note that the one-layer resonances split into N in the multilayer configuration [6]. The new resonances not present in the one-layer structure are weaker and have higher losses. Some of them exhibit an electric behavior and others a magnetic one, explaining, without entering into the details, the low FOM $n' > 0$ and $n' < 0$ peaks in Fig. 5, respectively.
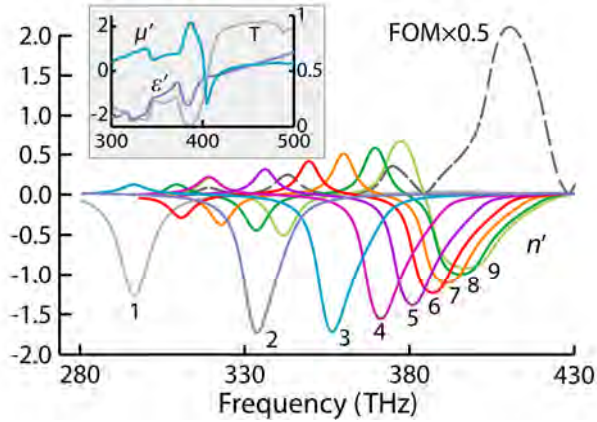
Fig. 5. Evolution of n' as a function of N for an FMM with $s = 10$ nm, $t = 25$ nm, $a_x = a_y = 400$ nm and $h = 275$ nm. FOM×0.5 for the $N = 9$ case (dashed curve). Inset, T (right axis), ε', and μ' (left axis).

In conclusion, we have presented an alternative route to achieve a medium with simultaneous negative ε' and μ' in the visible spectrum. This route exploits the existence of a second magnetic resonance in a modified FMM. The proposed structure is independent of polarization and exhibits a high FOM thanks to its double negative nature. Finally, the stacking of multiple layers has been studied, observing the convergence of n' with increasing N.

Acknowledgements

References

1. R. A. Shelby, D. R. Smith, and S. Schultz, "Experimental Verification of a Negative Index of Refraction," Science **292**, 77-99 (2001).
2. C. M. Soukoulis, S. Linden, and M. Wegener, "Negative refractive index at optical wavelengths," Science **315**, 47-49 (2007).
3. J. Valentine, S. Zhang, T. Zentgraf, E. Ulin-Avila, D. A. Genov, G. Bartal, and X. Zhang, "Three-dimensional optical metamaterial with a negative refractive index," Nature **455**, 376-379 (2008).
4. G. Dolling, M. Wegener, C. M. Soukoulis, S. Linden, "Negative-index metamaterial at 780 nm wavelength," Opt. Lett. **32**, 53-55 (2007).
5. U. K. Chettiar, A. V. Kildishev, H. Yuan, W. Cai, S. Xiao, V. P. Drachev, and V. M. Shalaev, "Dual-band negative index metamaterial: double negative at 813 nm and single negative at 772 nm," Opt. Lett. **32**, 1671-1673 (2007).

6. N. Liu, L. Fu, S. Kaiser, H. Schweizer, and H. Giessen, "Plasmonic building blocks for magnetic molecules in three-dimensional optical metamaterials," Adv. Mater. **20**, 3859-3865 (2008).
7. X. Chen, T. M. Grzegorczyk, B. Wu, J. Pacheco, Jr., and J. A. Kong, "Robust method to retrieve the constitutive effective parameters of metamaterials," Phys. Rev. E **70**, 016608-016614 (2004).
8. R. A. Depine and A. Lakhtakia, "A new condition to identify isotropic dielectric-magnetic materials displaying negative phase velocity," Microwave Opt. Technol. Lett. **41**, 315-316 (2004).
9. A. Mary, S. G. Rodrigo, F. J. García-Vidal, and L. Martín-Moreno, "Theory of negative-refractive-index response of double-fishnet structures," Phys. Rev. Lett. **101**, 103902 (2008).
10. R. Ortuño, C. García-Meca, F.J. Rodríguez-Fortuño, J. Martí, and A. Martínez, "Role of surface plasmon polaritons on optical transmission through double layer metallic hole arrays," Phys. Rev. B **79**, 075425 (2009).
11. G. Dolling, C. Enrich, M. Wegener, C. M. Soukoulis, and S. Linden, "Low-loss negative-index metamaterial at telecommunication wavelengths," Opt. Lett. **31**, 1800-1802 (2006).
12. C. García-Meca, R. Ortuño, F.J. Rodríguez-Fortuño, J. Martí, and A. Martínez, "Negative refractive index metamaterials aided by extraordinary optical transmission", Opt. Express, to be published.
13. R. Gordon and A. Brolo, "Increased cut-off wavelength for a subwavelength hole in a real metal," Opt. Express **13**, 1933-1938 (2005).
14. E. N. Economou, "Surface plasmons in thin films," Phys. Rev. **182**, 539-554 (1969).

2.7

PAPER3. LOW-LOSS MULTILAYERED METAMATERIAL EXHIBITING A NEGATIVE INDEX OF REFRACTION AT VISIBLE WAVELENGTHS

Low-loss multilayered metamaterial exhibiting a negative index of refraction at visible wavelengths

Carlos García-Meca,[1]* Juan Hurtado,[1] Javier Martí,[1] Alejandro Martínez,[1] Wayne Dickson,[2] and Anatoly V. Zayats[2]

[1]Nanophotonics Technology Center, Universidad Politécnica de Valencia, Camino de Vera s/n 46022, Valencia, Spain
[2]Nano-optics and Near-field Spectroscopy Laboratory, Department of Physics, King's College London, Strand, London WC2R 2LS, United Kingdom
[*]cargarm2@ntc.upv.es

ABSTRACT

We experimentally demonstrate a low-loss multilayered metamaterial exhibiting a double-negative refractive index in the visible spectral range. To this end, we exploit a second-order magnetic resonance of the so-called fishnet structure. The low-loss nature of the employed magnetic resonance, together with the effect of the interacting adjacent layers, results in a figure of merit as high as 3.34. A wide spectral range of negative index is achieved, covering the wavelength region between 620 and 806 nm with only two different designs.

Optical media with a negative index of refraction are theoretically allowed by Maxwell's laws of electromagnetism [1]. Although not found in natural materials, negative refraction index has been successfully designed using artificial nanostructured materials termed metamaterials [2]. The interest in negative index media (NIM) lies in the importance of their exceptional properties, such as the possibility of superlensing or light storing [3,4]. Metamaterials exhibiting a negative index of refraction have been experimentally demonstrated in several ranges of the electromagnetic spectrum [2, 5]. However, it is in the visible regime where we can take full advantage of NIM properties. For instance, the superior imaging ability of NIMs would be essential for visible microscopy, with applications in microelectronics, bio- and nano-technology.

The desired features for a NIM are low-loss and isotropy. This last property includes by itself some other features such as polarization independence and negative-index behavior in the three spatial directions. The strict condition to obtain a negative real part of the refractive index $n = n' + in''$ is $\varepsilon''\mu' + \mu''\varepsilon' < 0$ [6], where the permittivity and permeability are $\varepsilon = \varepsilon' + i\varepsilon''$ and $\mu = \mu' + i\mu''$, respectively. Therefore, a NIM having negative ε' and μ', called double-negative NIM, is required if low losses are demanded. Up to now, only in a few experiments in have negative index metamaterials been

demonstrated in the visible spectrum, and none of the above features have been attained [7-9]. Although a large part of the visible spectrum has been covered by the nanofabricated NIMs (wavelengths from 580 nm to 780 nm), the current challenge is to improve the above-mentioned aspect in order to make these metamaterials suitable for practical applications.

In this work, we have fabricated multilayer NIMs that exhibit double-negative behaviour at visible wavelengths while presenting low-loss and polarization independent optical properties at normal incidence. This has been achieved by exploiting properties of a second-order magnetic resonance of the so-called fishnet structure, in contrast to previous works that used first-order magnetic resonances, both related to gap surface plasmon polariton (SPP) Bloch modes. Moreover, the fabricated metamaterial is the first experimental NIM in the visible regime made up of multiple unit cells along the propagation direction, an important step towards bulk NIMs in this band.

The recent experimental demonstrations of NIMs in the visible range are based on different variations of the so-called fishnet metamaterial [7-9] (see Fig. 1), which consists of $2N + 1$ alternating metal (m) and dielectric (d) stacked hole arrays resulting in N metamaterial unit cells in the propagation direction ($N = 1$ corresponds to m–d–m, $N = 2$ to m–d–m–d–m, . . .). This structure can be described by an effective permittivity governed by the cut-off frequency of the waveguide mode supported by the holes despite wavelength-scale nanostructuring [10,11]. The negative index of this structure arises from the combination of this effective negative permittivity with the permeability resonance resulting from the excitation of a gap SPP in the metal-dielectric-metal multilayer [10-12].
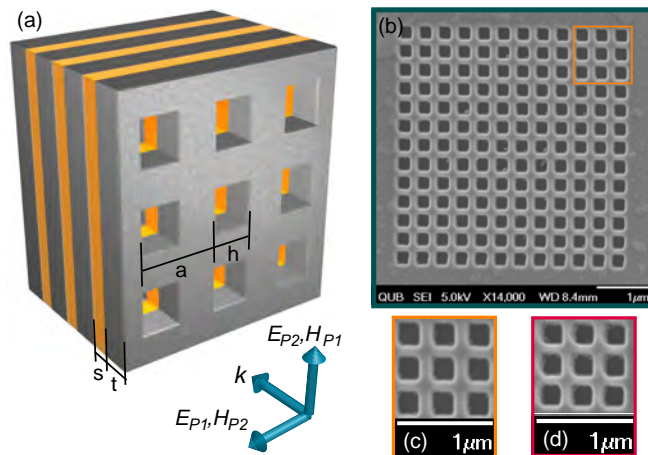
Fig. 1 (a) Schematic of a fishnet metamaterial made up of three unit cells in the propagation direction. The overall number of layers is 7 (4 metal layers and 3 dielectric layers). (b) Top-view SEM image of the fabricated 3-unit-cell fishnet structure 3 (see Table 1). (c) Detail of image in (b). (d) Detail of the fabricated 3-unit-cell fishnet structure 4.

Since the multilayered structure is periodically patterned and forms a plasmonic crystal, its SPP Bloch modes can be excited at certain frequencies when diffraction of light on the periodic structure contributes towards matching the wave vectors of SPP and photons [13-15]. In all recent experimental realizations, the fishnet negative index is a consequence of the excitation of the first-order SPP Bloch mode along the Γ-X direction of the Brillouin zone of the square lattice crystal. The main drawback of this approach is the high loss due to the weak nature of this resonance in the employed configurations. For instance, in experiments [7-9], the maximum figure of merit (FOM), which is a standard loss measure defined as FOM = $|n'/n''|$, is 0.5, 0.7, and 0.3, respectively, implying large absorption losses. Theoretical analysis reveals that the use of SPP Bloch modes in the Γ-M direction of the Brillouin zone (the so-called second order magnetic resonance) makes attainable a strong permeability resonance with an associated negative permeability within the negative permittivity region [16]. In the overlapping band, the structure exhibits a double-negative refractive index with low loss. One of the fundamental advantages of this structure is that the square lattice structure leads to polarization insensitive optical properties at normal incidence. Although there are ways to improve the loss aspect in fishnet structures based on the first-order SPP resonance [17], it has been shown that, for a polarization independent configuration, the FOM associated with the second-order resonance is noticeably higher than that of the first-order one. Thus, the use of the second-order resonance is more adequate if our goal is to achieve low-loss and polarization independence simultaneously. It is worth mentioning that polarization independence has not been attained in previous experiments, either due to the geometry of the employed structures (based on non-square holes or lattices) or to fabrication limitations.

Another issue is the transition from two-dimensional to bulk metamaterial behavior in this geometry. It is known that the constitutive parameters of the fishnet metamaterial change with increasing number of functional layers, until they stabilize for a certain N [16,18]. Moreover, the addition of more layers in this metamaterial also enhances the FOM [16,18,19]. Thus, the fabrication of a multiple-functional-layer fishnet metamaterial is highly desirable. Given the previous considerations, we designed several seven-layer ($N = 3$) fishnet structures with the second order magnetic resonance in the visible spectral range. Structures with a single functional layer were investigated for comparison (see Table 1).

Structure	N	Ag layers	HSQ layers	t (nm)	s (nm)	h (nm)	a (nm)
1	1	2	2	35	30	250	400
2	1	2	2	35	30	220	365
3	3	4	4	35	15	250	400
4	3	4	4	35	15	220	350

Table 1. Geometrical parameters of the fabricated structures.

It is worth stressing that only single-layer fishnet structures with negative index in the visible spectrum had been fabricated until now. The designed structures with several sets of parameters (Table 1) were fabricated as follows. Soda lime glass (refractive index of 1.51) was used as a bulk substrate. Silver layers of thickness t were deposited by e-beam evaporation at 2.5 Å·s⁻¹. Spin-on resist FOX-12 (provided by Dow Corning) based on hydrogen silsesquioxane (HSQ) was used as the inter-layer dielectric. The resist was diluted in methyl isobutyl ketone in a ratio of 1:6 and spinned at 6000 rpm with an acceleration of 3000 rpm·s⁻¹. It was annealed after deposition to remove solvents and densify the film. The resulting refractive index of the dielectric layers (thickness s) in the considered spectral range was 1.41. An additional HSQ layer of the same thickness was deposited on top of the outer silver layer to avoid environmental effects. Thus, the one- and three-unit-cell structures were made up of four and eight layers, respectively. To create the periodic pattern of square holes, focused ion beam milling was used due to its ability to achieve high aspect ratio geometries. Geometrical patterns were designed on a pixel by pixel basis, with each point represented by its spatial coordinate (specifying ion-beam position) and an associated dwell time controlling the milling duration. Initially, depth calibration was performed using atomic force microscope characterization of structures fabricated with a range of milling times. Lateral dimensions were adjusted using scanning electron microscope (SEM) data to ensure ion-beam tail effects were incorporated in the final designs.
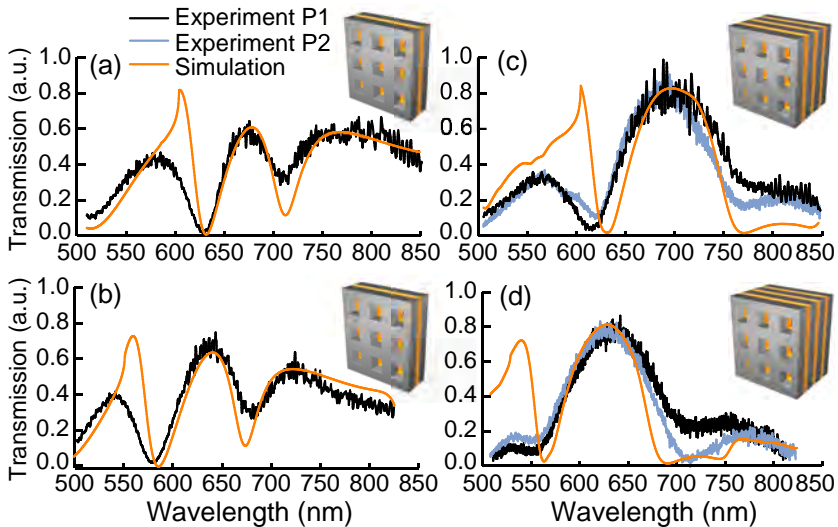
Fig. 2. Normal incidence zero-order measured and simulated transmission spectra of different fabricated metamaterials: (a) structure 1 (see Table 1), (b) structure 2, (c) structure 3, and (d) structure 4. Polarization of the incident light with respect to the crystal lattice is shown in Fig. 1.

The ion current used for all fabrication was maintained at a maximum of 10 pA, ensuring the smallest focused spot size, at an accelerating voltage of 30 kV. Top-view SEM images of some of the fabricated structures are shown in Fig. 1. Experimental and simulated spectra of the fabricated metamaterials are presented in Fig. 2. Numerical modelling was performed with CST Microwave Studio. In the simulations, silver was characterized by a Drude-Lorentz model including a term accounting for inter-band transitions [20]. The adjustable parameters α (chosen such that the collision frequency γ_c = 8.5×10^13 s^{-1}) and β were set to match experimental data. Note that, due to the inter-band transitions term, the losses ascribed to Ag are somewhat higher than in previous works. The optical transmission spectra were measured using a fibre-coupled spectrometer with a liquid-nitrogen-cooled CCD and *W*-halogen white-light source. The normal incidence transmission spectra are the same (within fabrication tolerances) for the two orthogonal polarizations of the incident light along the main axes of the crystal lattice, which confirms the polarization independence at normal incidence. A good agreement between the simulations and the measurements is observed, verifying the reliability of the numerical results, from which the effective metamaterial parameters can be extracted. Discrepancies at short wavelengths below Wood's anomaly (dips around 600 nm) are due to the fact that only zero-order transmission is captured in the measurements, while total transmission is calculated in the simulations, including high-order diffraction beams. A generalized version of the retrieval algorithm described in [21] was used to account for the bianisotropy introduced by the substrate and top HSQ layer.
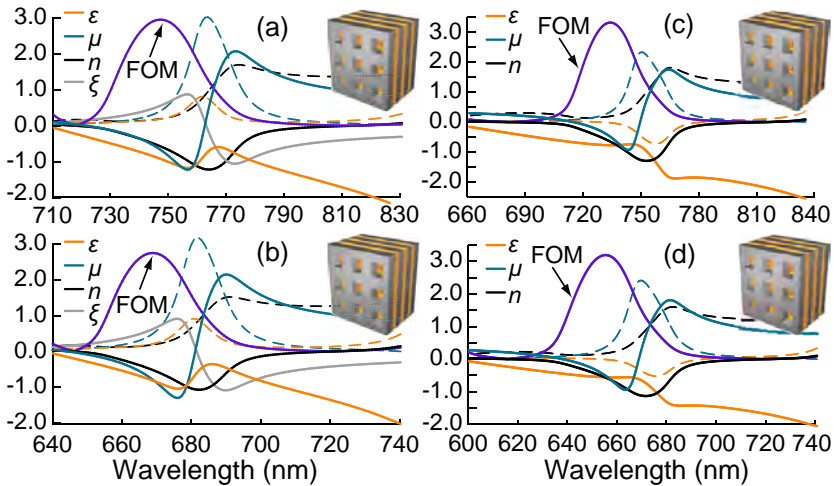
Fig. 3. FOM and real (solid) and imaginary (dashed) parts of the fabricated structures effective parameters with [(a) structure 3 and (b) structure 4] and without [(c) structure 3 and (d) structure 4] the substrate and top HSQ layer. $\xi = \xi' + i\,\xi''$ is the bianisotropy parameter

The retrieved parameters of the fabricated structures with $N = 3$ are shown in Fig. 3, where we also depict the retrieved parameters for the free-standing case to allow for comparison with previous works where bianisotropy was not considered (note that the fabricated structures were optimized for the free-standing case). Results are very similar in both cases. The main features of all the fabricated metamaterials are summarized in Table 2 together with the data for the other experimentally made metamaterials for the free-standing case.

Reference	N	min(n')	max(FOM)	$n < 0$ bands	Polarization independent	Double-negative
[7]	1	-0.6 (780 nm)	0.5 (780 nm)	~750-800 nm	No	No
[8]	1	-1 (776 nm)	0.7 (772 nm)	753-810 nm	No	No
[9]	1	-0.25 (580 nm)	0.3 (580 nm)	567-602 nm	No	No
This work (1)	1	-0.68 (690 nm)	1.9 (678 nm)	656-712 nm	Yes	Yes
This work (2)	1	-0.66 (650 nm)	1.75 (642 nm)	620-672 nm	Yes	Yes
This work (3)	3	-1.3 (752 nm)	3.34 (734 nm)	694-806 nm	Yes	Yes
This work (4)	3	-1.13 (670 nm)	3.19 (655 nm)	620-713 nm	Yes	Yes

Table 2. Main features of fabricated metamaterials in comparison with previous experiments. Numbers in parenthesis in column 1 refer to the corresponding structure in Table 1. The polarization independence column refers only to the case of normal incidence.

As can be seen, a high FOM with a maximum value of 1.9 is observed in the 1-functional-layer structures. The spectral ranges covered by the NIM region in these metamaterials span 656-712 nm (structure 1) and 620-672 nm (structure 2). A further improvement of the figure of merit is achieved with the 3-functional-layer structure, reaching values as high as 3.34. In this case, the NIM spectral ranges are 693-806 (structure 3) and 620-713 nm (structure 4). A minimum negative index of -1.3 is achieved (structure 3), with a FOM = 2.73 at the wavelength at which $n = -1$. It is worth mentioning that the ratio of the free space wavelength to the size of the unit cell along the propagation direction goes from 12.4 to 15.6. It has been shown that the zeroth-order Bloch mode dominates propagation inside a fishnet structure so that it can be considered as homogeneous [22]. An indicator of this property is the convergence of the refractive index with increasing N, which has been verified for the fishnet configuration used here at $N \sim 8$ [16]. Nevertheless, the optical properties of the fabricated structures have been optimized for their specific number of unit cells.

The angular dependence of the optical properties of the fabricated metamaterials has also been studied. The transmission dispersion measurements were performed in the angular range of 0º-30º, showing a very good agreement between simulations and experiment (Fig. 4). The main physical phenomena involved in the creation of the double-negative band can be observed in the dispersion plot. On one side, the wide transmission

band around 1.86 eV (667 nm) can be identified with the localized resonance occurring at the cut-off frequency of the waveguide mode supported by the holes (see also Fig. 2). This mode controls the effective permittivity of the metamaterial [11]. On the other side, the forbidden band observed approximately at 1.75 eV (708 nm), corresponds to the SPP in the Γ-*M* direction of the Brillouin zone, which is responsible for the permeability resonance. Remarkably, the SPP Bloch modes corresponding to this resonance exhibit weak dispersion, in contrast to the highly dispersive SPP modes supported by unstructured metal-dielectric-metal multilayers or previous typical fishnet configurations. This may be ascribed to the large size of the apertures compared to the unit cell size and the hybridization of the SPP mode with the above-mentioned localized resonance [10]. The flatness of the SPP band responsible for the magnetic resonance suggests the possibility to achieve nearly angle-independent NIM properties in a considerable angular range.
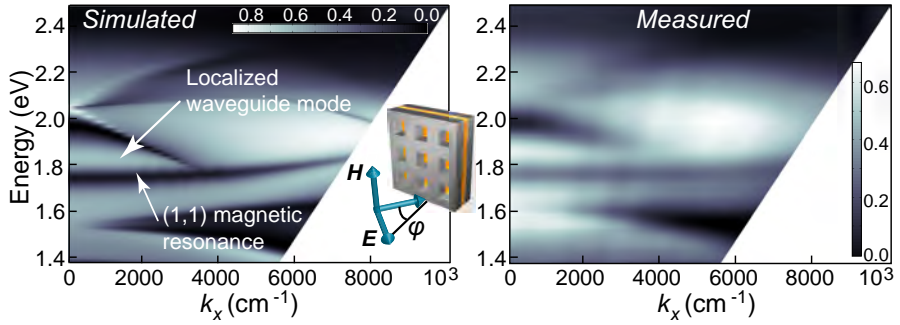
Fig. 4. Simulated and measured transmission dispersion of structure 1 as a function of transverse wave vector and photon energy. The incident light is *p* polarized with respect the plane of incidence. The response is similar for *s* polarized light (not shown).

It is worth mentioning that by using an active optical medium as the dielectric layer and under optical pumping conditions it becomes feasible to overcome losses and even achieve gain in a fishnet metamaterial [23]. In this sense, our metamaterial is merely passive and its performance could be much improved by making use of an active optical medium in the wavelength region at which the negative index behavior is obtained.

In conclusion, we have experimentally characterized multilayer fishnet metamaterials with simultaneously negative permittivity and permeability in the visible regime. This entails an important step towards homogeneous NIMs in this spectral range. The metamaterial exhibits low losses and polarization independence at normal incidence. In addition, it has been found that the gap-SPP Bloch modes determining the permeability resonance display weak dispersion. Further refinement of the fabrication process is expected to extend the negative-index band towards shorter wavelengths.

Acknowledgements

References

1. V. G. Veselago, Sov. Phys. Uspekhi **10**, 509 (1968).
2. R. A. Shelby, D. R. Smith, and S. Schultz, Science **292**, 77 (2001).
3. J. B. Pendry, Phys. Rev. Lett**. 85**, 3966 (2000).
4. K. L. Tsakmakidis, A. D. Boardman, and O. Hess, Nature **50**, 397 (2007).
5. C. M. Soukoulis, S. Linden, and M. Wegener, Science **315**, 47 (2007).
6. R. A. Depine and A. Lakhtakia, Microwave Opt. Technol. Lett. **41**, 315 (2004).
7. G. Dolling, M. Wegener, C. M. Soukoulis, and S. Linden, Opt. Lett. **32**, 53 (2007).
8. U. K. Chettiar et al., Opt. Lett. **32**, 1671 (2007).
9. S. Xiao et al., Opt. Lett. **34**, 3478 (2009).
10. A. Mary et al., Phys. Rev. Lett. **101**, 103902 (2008).
11. C. García-Meca et al., Opt. Express **17**, 6026 (2009).
12. R. Ortuño et al., Phys. Rev. B **79**, 075425 (2009).
13. A. V. Zayats, I. I. Smolyaninov, and A. A. Maradudin, Phys. Rep. **408**, 131 (2005).
14. W. Dickson, G. A. Wurtz, P. R. Evans, R. J. Pollard, and A. V. Zayats, Nano Lett. **8**, 281 (2008).
15. A. Minovich *et al.,* Phys. Rev. B **81**, 115109 (2010).
16. C. García-Meca et al., Opt. Lett. **34**, 1603 (2009).
17. J. F. Zhou, T. Koschny, and C. M. Soukoulis, Opt. Express **16**, 11147 (2008).
18. S. Zhang et al., Opt. Express **14**, 6778 (2006).
19. J. Valentine et al., Nature **455**, 376 (2008).
20. V. P. Drachev et al., Opt. Express **16**, 1186 (2008).
21. C. E. Kriegler et al., IEEE J. Sel. Top. Quantum Electron. **16**, 367 (2010).
22. C. Rockstuhl et al., Phys. Rev. B **77**, 035126 (2008)
23. S. Xiao et al., Nature **466**, 735 (2010).

2.8

PAPER4. DUAL-BAND DOUBLE-NEGATIVE-INDEX FISHNET METAMATERIAL AT MILLIMETER-WAVES

Dual-band double-negative-index fishnet metamaterial at millimeter-waves

Miguel Navarro-Cía,[1,2,*] Carlos García-Meca,[3] Miguel Beruete,[2] Alejandro Martínez,[3] and Mario Sorolla[2]

[1]Experimental Solid State Group, Imperial College London, London SW7 2AZ, UK
[2]Millimeter and Terahertz Waves Laboratory, Universidad Pública de Navarra, 31006 Pamplona, Spain
[3]Nanophotonics Technology Center, Universidad Politécnica de Valencia, 46022 Valencia, Spain
[*] m.navarro@imperial.ac.uk

ABSTRACT

An effective negative refractive index (NRI) is demonstrated and experimentally verified for the first two propagation bands of a fishnet-like metamaterial at millimeter-wave frequencies. The dual-band NRI behavior is achieved by engineering the diffraction order (± 1, ± 1) associated with the internal mode supported between holey layers to correspond with the second propagation band. In addition to the experimental interferometric technique that accounts for the handedness of the propagation, numerical results are given to predict the dual-band effective NRI and to confirm dual-band negative refraction for a prism composed of the proposed metamaterial.

Metamaterials (mmts) [1] hold promise for both basic science and technology due to their linked new physics such as NRI [2] or perfect lensing [3]. Within the past years, an unexpected theoretical and experimental development has helped to strengthen the evidence that the effective NRI observed in fishnet mtms (stacked hole arrays) [4,5] has a strong connection with extraordinary transmission phenomenon [5-7]. Fishnet mtms, first reported at infrared frequencies [4,8], have been widely studied in parallel at microwaves-to-terahertz where they have been termed extraordinary transmission mtms [5,9] (because of the aforementioned connection), and infrared-to-visible frequencies [10-13] because they substantially outperform other mtms. Most of the existing studies have ultimately confirmed that the general underlying physics relies primarily on diffraction orders of complex surface waves [14-19] that can be either external or internal (Floquet-Bloch guided mode of the waveguide formed by pairs of holey metals) complex surface waves [11, 12, 15, 18-20]. Indeed, this interpretation allowed some authors of this Letter to engineer the (± 1, ± 1) diffraction order of the internal mode to become the second propagation band of the fishnet mtm [11,12,18], achieving effective NRI for the first two propagation bands [the first one associated to the (0, ± 1) diffraction order of the internal mode]. Notice that in [19], no dual-band double-negative-index behavior is displayed under normal incidence for the first two propagation modes.

Recently, several authors of this Letter reported an experimental verification of the above-mentioned fishnet resonance (±1, ±1) at visible wavelengths [18]. In this spectral range, only amplitude measurements are usually carried out due to the difficulty of capturing the phase response. Here, we demonstrate experimentally at millimeter-waves the backward-wave nature of the aforementioned lowest propagation bands from the phase response of the fishnet structure as a function of the number of unit cells in the propagation direction. Moreover, this work reinforces the view that the phenomenon is not limited to a particular class of complex surface wave such as surface plasmon polaritons, but to the whole framework of complex surface waves.

The sketch of the fishnet mtm under study can be seen in Fig. 1, together with the fabricated prototype. The unit cell parameters are: in-plane periodicities $d_x = d_y = d = 2.5$ mm, stack periodicity $d_z = 0.525$ mm ($\approx 0.13\lambda_0$ and $0.19\lambda_0$ for the first and second propagation band, respectively), hole diameter $a = 1.1$ mm, metal thickness $t = 0.035$ mm, and dielectric permittivity of the dielectric spacing $\varepsilon_r = 2.43 - j0.022$. We define a single functional layer (FL) as metal-dielectric-metal, whereas successive functional layers consist of $2N + 1$ alternating metal and dielectric stacked hole arrays with $N = 2, 3$, etc. (for instance, two FLs comprise metal-dielectric-metal-dielectric-metal) [11].
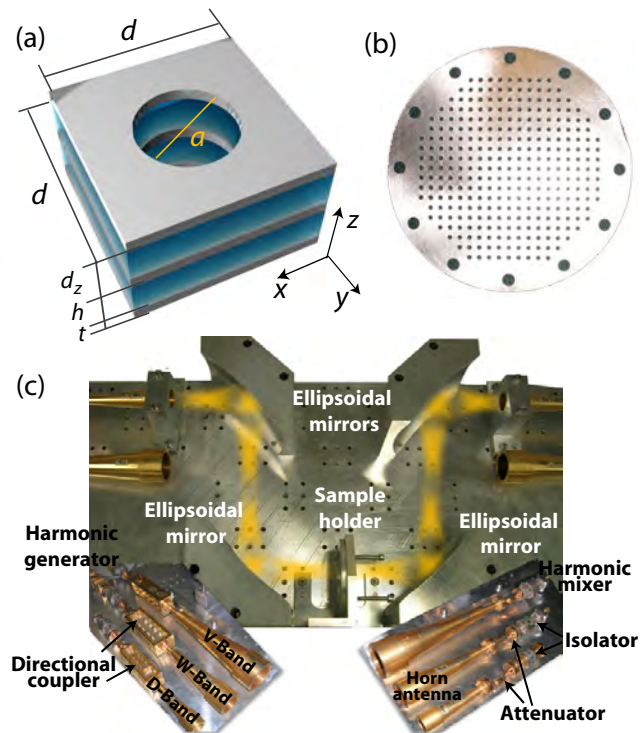
Fig. 1 (a) Geometrical dimensions of the considered fishnet structure (picture of two unit cells). (b) Fabricated prototype. (c) Experimental setup.

The dependence of the retrieved effective index of refraction n_z [21] as a function of the number of FLs is displayed in Fig. 2(a). It should be noted that physically meaningful material parameters are linear response functions that must be independent of the applied electric field, and independent of the geometrical size and shape of a medium sample [22]. Therefore, the effective index of refraction assigned to this finite (in number of metal layers) mesoscopic stack by this procedure should be interpreted with some precautions [23]. For comparison purposes, we calculated the dispersion diagram of the ideal infinite structure through an Eigen-mode analysis. The first two propagation bands are plotted in Fig. 2(b), where we can observe their backward nature. The effective n_z derived from the dispersion diagram ($n_z = \mathrm{sgn}(\partial\omega/\partial k_z)k_z c_0/\omega$, where $\omega = 2\pi f$ is the angular frequency and c_0 the speed of light in vacuum) is also plotted in Fig. 2(a), which is in excellent agreement with the retrieved n_z corresponding to the finite structure. Note that losses are not taken into account in the Eigen-mode analysis. As a consequence, the low-frequency part of each band in Fig. 2(a) is a forbidden region in the dispersion diagram, since at these frequencies propagation is dominated by losses.
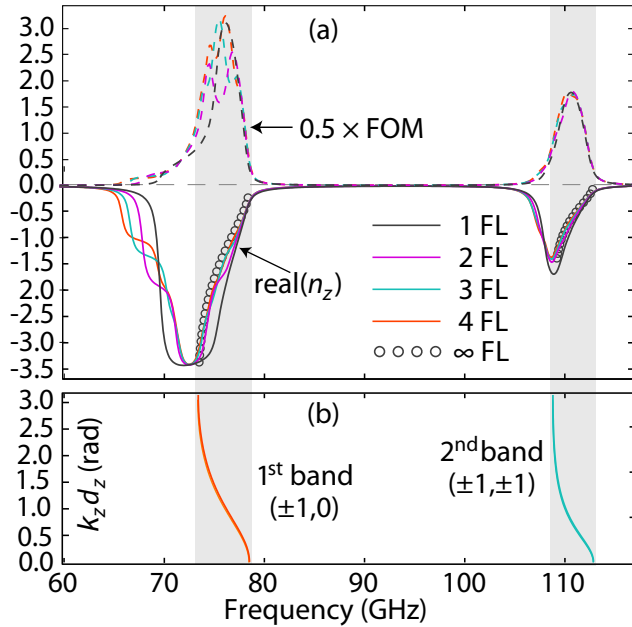
Fig. 2. (a) Retrieved effective refractive index for different number of FLs. Solid and dashed lines represent the real part of n_z and the figure of merit, FOM = $|\mathrm{Re}(n_z)/\mathrm{Im}(n_z)|$, respectively. The circles correspond to the index derived from the dispersion diagram. (b) Dispersion diagram.

The internal modes responsible for these two bands can be clearly identified by inspection of the electric field E distribution at the corresponding frequencies. In Fig. 3(a) we depict the E-field intensity in a xy plane halfway between two metal plates for the one FL case. The field patterns are unequivocally those of the first and second diffraction

orders of the internal mode. Moreover, the plots of *E* in the *yz* plane crossing the center of the holes confirm that the fields are concentrated between metals at these frequencies.
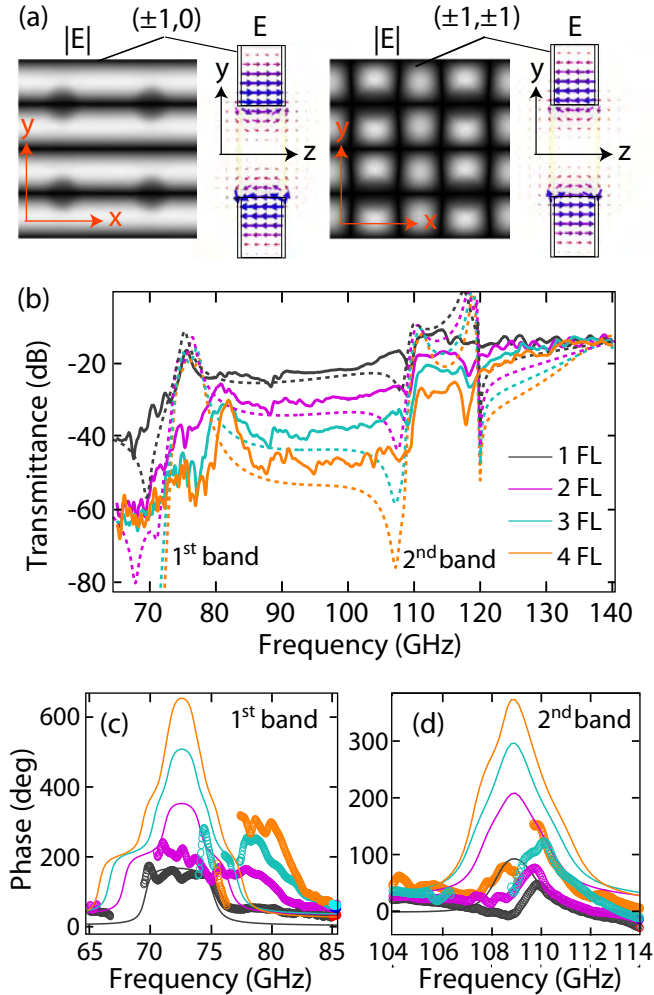
Fig. 3. (a) Electric field at the center frequency of both bands at two different two-dimensional cuts. The incident wave is polarized with the *E*-field along the *y*-axis. (b) Measured (solid lines) and simulated (dashed lines) transmission spectra. (c) First and (d) second band measured (circles) and simulated (solid lines) phase response on transmission.

To provide an even more solid verification, the effective negative refractive behavior was examined experimentally. The stack shown in Fig. 1(b) was fabricated using ARLON CUCLAD 250 LX and a laser-based printed circuit board production. For the experimental characterization, an AB-Millimetre™ vector network analyzer and a quasi-optical bench were used. Figures 3(b)-3(d) shows the complex experimental data's magnitude and phase response. In agreement with the numerical calculations, two

prominent bands come up within the *W*-band of the millimeter-waves. The first one associated to the (0, ±1) internal mode, whereas the second linked to the (±1, ±1) internal mode. The band spectral positions of the measurements coincide with the numerical calculations, except for a slight frequency increase of the first band, which can be safely ascribed to non-perfect assembly of the FLs. The growth of the stack is performed by screwing (at the framework) additional metal-dielectric slabs or FLs which likely leaves small air gaps between stacked layers. This may cause a slight reduction of the effective dielectric permittivity of the interspacing. It is noteworthy that losses experienced by the second band are lower than those experienced by the first band. Qualitatively, it can be argued that the holes are more subwavelength for the first band and thus narrower peaks are expected, which are more susceptible to losses. Alternatively, the Drude response of the permittivity together with the double Lorentz model for the permeability can explain the insertion losses from an impedance mismatch perspective. Assuming that both Lorentz responses have identical strength, the effective electric permittivity may not reach negative values low enough to be similar to the effective magnetic permeability. However, at the second resonance it reaches lower values that may balance the effective magnetic permeability, achieving thus impedance matching. Indeed, according to the retrieval method, the maximum wave impedance of four FLs is 0.075 and 0.17 for the first and second band, respectively. Therefore, the Fresnel reflection losses are higher at the first band, justifying the higher measured insertion losses in this band.

In order to assign a backward- or forward-wave propagation direction from the experimental data one should inspect the phase response [see Figs. 3(c) and 3(d)]. For backward-wave/forward-wave propagation, the phase response increases/decreases with the number of FLs because of the $\exp(-jk_z\Delta l)$ dependence of the transmission, where Δl the length of the stack, and k_z is the wave-number in the stack. In the case of effective NRI mtms $k_z < 0$, and thus the dependence is $\exp(+j|k_z|\Delta l)$. With this description in mind, the response of the phase shown in Figs. 3(c) and 3(d) is clearly in accordance with backward-waves propagation, that is, effective negative n_z. The simulated phase response in transmission is also included in Figs. 3(c) and 3(d) and exhibits the same tendency as the measured results. Note that the phase response for very low values of transmittance, where the measurement of phase is challenging, has been removed from the plot to avoid misinterpretation.

As a final check, we simulate a prism based on the fishnet mtm. To simplify the numerical effort, the simulations deal with a two-dimensional prism. This allows us to confirm straightforwardly the negative refraction associated with the first two propagation bands. From the numerical results shown in Fig. 4, it can be seen that the proposed fishnet mtm supports one-dimensional effective negative refraction in both bands since the outgoing beam deflects towards the normal.
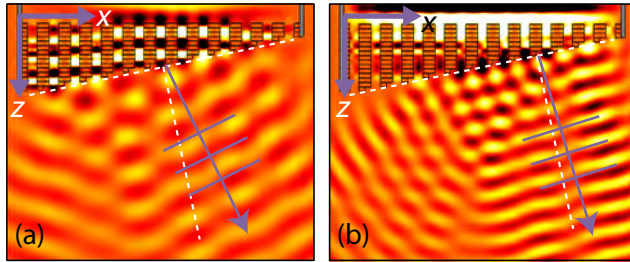
Fig. 4. Refraction in a fishnet mtm prism for (a) the first and (b) the second band. The interface and its normal are plotted in dashed line and the power flow direction with a purple arrow.

In summary, we have demonstrated experimentally at millimeter-wave frequencies the unusual phase response associated with an effective NRI for the two first propagation bands of a fishnet metamaterial. This effect is achieved by tuning the parameters in such a way that the (±1, ±1) diffraction order of the internal mode is the second propagation band. The index of refraction retrieved from the scattering parameters of numerical simulations shows good agreement with the index derived from the structure eigenmodes, and both are confirmed by experimental measurements. Furthermore, negative refraction in both bands is numerically demonstrated with a prism. This experimental confirmation is another stepping stone in the path to enrich the properties of metamaterials, making them attractive for practical applications at frequencies such as millimeter-wave or terahertz.

Acknowledgements

References

1. L. Solymar and E. Shamonina, *Waves in Metamaterials* (Oxford University, 2009).
2. V. G. Veselago, "The electrodynamics of substances with simultaneously negative values of ε and μ," Sov. Phys. Usp. **10**, 509 (1968).
3. J. B. Pendry, "Negative refraction makes a perfect lens," Phys. Rev. Lett. **85**, 3966 (2000).

4. S. Zhang, W. Fan, N. C. Panoiu, K. J. Malloy, R. M. Osgood, and S. R. J. Brueck, "Experimental demonstration of near-infrared negative-index metamaterials," Phys. Rev. Lett. **95**, 137404 (2005).

5. M. Beruete, M. Sorolla, and I. Campillo, "Left-handed extraordinary optical transmission through a photonic crystal of subwavelength hole arrays," Opt. Express **14**, 5445 (2006).

6. T.W. Ebbesen, H.J. Lezec, H. Ghaemi, T. Thio, and P.A. Wolf, "Extraordinary optical transmission through sub-wavelength hole arrays, " Nature **391**, 667 (1998).

7. M. Beruete, M. Sorolla, I. Campillo, J.S. Dolado, L. Martín-Moreno, J. Bravo-Abad, and F.J. García-Vidal, "Enhanced millimetre-wave transmission through subwavelength hole arrays, " Opt. Lett. **29**, 2500 (2004).

8. G. Dolling, C. Enkrich, M. Wegener, C.M. Soukoulis and S. Linden, "Simultaneous negative phase and group velocity of light in a metamaterial," Science **312**, 892 (2006).

9. M. Navarro-Cía, M. Beruete, M. Sorolla, and I. Campillo, "Negative refraction in a prism made of stacked subwavelength hole arrays," Opt. Express **16**, 560 (2008).

10. J. Valentine, S. Zhang, T. Zentgraf, E. Ulin-Avila, D. A. Genov, G. Bartal, and X. Zhang, "Three-dimensional optical metamaterial with a negative refractive index," Nature **455**, 376 (2008).

11. C. García-Meca, R. Ortuño, F. J. Rodríguez-Fortuño, J. Martí, and A. Martínez, "Double-negative polarization-independent fishnet metamaterial in the visible spectrum," Opt. Lett. **34**, 1603 (2009).

12. R. Ortuño, C. García-Meca, F. J. Rodríguez-Fortuño, J. Martí, and A. Martínez, "Role of surface Plasmon polaritons on optical transmission through double layer metallic hole arrays," Phys. Rev. B **79**, 075425 (2009).

13. S. Xiao, U.K. Chettiar, A.V. Kildishev, V.P. Drachev, V.M. Shalaev, "Yellow-light negative-index metamaterials," Opt. Lett. **34**, 3478 (2009).

14. A. Ishimaru, *Electromagnetic wave propagation, radiation, and scattering* (Prentice Hall, 1991).

15. A. Mary, S.G. Rodrigo, F.J. García-Vidal, L. Martin-Moreno, "Theory of negative refractive-index response of double-fishnet structures," Phys. Rev. Lett. **101**, 103902 (2008).

16. M. Beruete, M. Navarro-Cía, M. Sorolla, and I. Campillo, "Negative Refraction through an Extraordinary Transmission Left-Handed Metamaterial slab," Phys. Rev. B **79**, 195107 (2009).

17. M. Beruete, M. Navarro-Cía, M. Sorolla, and I. Campillo, "Strong lateral displacement in polarization anisotropic extraordinary transmission metamaterial," New J. Phys. **12**, 063037 (2010).

18. C. García-Meca, J. Hurtado, J. Martí, A. Martínez, W. Dickson, and A.V. Zayats, "Low-Loss Multilayered Metamaterial Exhibiting a Negative Index of Refraction at Visible Wavelengths," Phys. Rev. Lett. **106**, 067402 (2011).

19. M. Beruete, M. Navarro-Cía, and M. Sorolla, "High Numerical Aperture and Low-Loss Negative Refraction Based on the Fishnet Rich Anisotropy," Photonic. Nanostruct: Fundam. Appl. (to be published).

20. J. Yang, C. Sauvan, H. T. Liu, and P. Lalanne, "Theory of Fishnet Negative-Index Optical Metamaterials," Phys. Rev. Lett. **107**, 043903 (2011).

21. X. Chen, T. M. Grzegorczyk, B. Wu, J. Pacheco, Jr., and J. A. Kong, "Robust method to retrieve the constitutive effective parameters of metamaterials," Phys. Rev. E **70**, 016608-016614 (2004).

22. L. Landau, and E.M. Lifschitz, *Electrodynamics of Continuous Media* (Elsevier, 1984).

23. C. Menzel, T. Paul, C. Rockstuhl, T. Pertsch, S. Tretyakov, and F. Lederer, "Validity of effective material parameters for optical fishnet metamaterials," Phys. Rev. B **81**, 035320 (2010).

2.9   Our contribution (II): Strong magnetism at visible frequencies and optical security

Our first attempt towards optical NIMs was based on a structure consisting on cut thick nano-strips (PAPER5). For a one-layer configuration, this metamaterial exhibits a low-loss negative-index band and, like the fishnet structure described above, can be made polarization-independent . Unfortunately, we have not yet found a configuration of this metamaterial that can be homogenized.[9] However, a second structure inspired by the nano-strips composite and consisting of closely packed metallic nano-hoops, turned out to have some useful properties. Specifically, the most interesting feature of the nano-hoops metamaterial is that it exhibits a surprisingly strong magnetic response in the visible range. Although it is not homogenizable either, there is no doubt that electromagnetic fields induce unusually high magnetic moments in the nano-hoops medium. This property fits perfectly for a new killing application of metamaterials: optical security. In this sense, the goal is not to obtain an isotropic medium that can be described by global bulk characteristic material parameters and the retrieval of these parameters. Rather, the main objective is to achieve a material with an exclusive optical response that can be easily identified from proper measurements and only reproducible with the most advanced nanofabrication techniques. Certainly, negative magnetic responses in the visible range fulfill these requirements.

Optical security labels are incorporated in a broad variety of objects: bank notes, identity cards, documents, clothes, etc. Most current approaches make use mainly of holographic, interference or diffractive techniques so that the object authenticity can be established by simple visual inspection. In any case, a key aspect in optical security devices is the incorporation of optical properties or features that are difficult to reproduce or mimic by other means. For instance, diffractive gratings provide a more secure performance than techniques based on subtractive color mixing, since their manufacture requires particular tools and processes which are not available to the general public.[83] In this sense, achieving a strong magnetic response at optical/visible wavelengths is a challenging task from the fundamental physics as well as technological (nano-structuring

[9] The retrieved constitutive parameters presented in PAPER5 correspond to a single layer of meta-atoms. The behavior of that specific structure is not preserved for multiple layers.
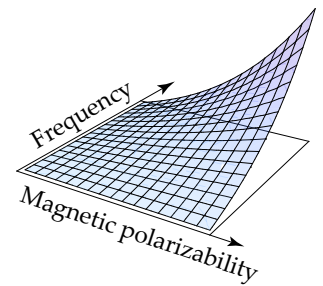
Figure 2.8: Optical security based on artificial magnetism. The fabrication and counterfeiting complexity (graph height) increases with photon frequency and the absolute value of the magnetic polarizability.

with very small resolution) points of view (see Figure 2.8). If the structure providing the magnetic response has to be used in an application that also requires high yield — like optical security labels —, we can conclude that it could be only manufactured in a small number of well-identified nano-foundries. Since the only way to produce a falsification is to fabricate structures of this kind, the possibilities for counterfeiting are enormously restricted, as the necessary fabrication facilities are under control and are not opened to general public. Thus, the optical response (artificial magnetism) of a photonic metamaterial at a certain visible wavelength can be used as an authenticity code or fingerprint for an object, which will ensure its authenticity. The difficulty to imitate is guaranteed by the control of the production mechanisms.

The details about the concept of metamaterials for optical security (due to Alejandro Martínez), as well as the nano-hoops structure, are described in PAPER6.

2.10

PAPER5. LOW-LOSS SINGLE-LAYER METAMATERIAL WITH NEGATIVE INDEX OF REFRACTION AT VISIBLE WAVELENGTHS

Low-loss single-layer metamaterial with negative index of refraction at visible wavelengths

C. García-Meca, R. Ortuño, R. Salvador, A. Martínez, and J. Martí

Nanophotonics Technology Center, Universidad Politécnica de Valencia, Camino de Vera s/n
46022, Valencia, Spain
*[*cargarm2@ntc.upv.es](mailto:cargarm2@ntc.upv.es)*

ABSTRACT

We present a structure exhibiting a negative index of refraction at visible or near infrared frequencies using a single metal layer. This contrasts with recently developed structures based on metal-dielectric-metal composites. The proposed metamaterial consists of periodically arranged thick stripes interacting with each other to give rise to a negative permeability. Improved designs that allow for a negative index for both polarizations are also presented. The structures are numerically analyzed and it is shown that the dimensions can be engineered to shift the negative index band within a region ranging from telecommunication wavelengths down to blue light.

1. Introduction

In the past few years, there has been a growing interest in artificially structured materials, termed metamaterials, showing properties not found in nature. One of the most attractive features of these composites is the possibility of obtaining negative refraction over a certain frequency band. A possible way to achieve a negative refractive index is to have a negative real part of the permittivity ($\varepsilon = \varepsilon' + i\varepsilon''$) and of the permeability ($\mu = \mu' + i\mu''$) at the same frequency. However, this is not a necessary condition. Strictly, the relation that must be satisfied is a more relaxed one [1]: $\varepsilon''\mu' + \mu''\varepsilon' < 0$. It is generally desirable to have simultaneous negative real parts of ε and μ so that losses become small. Since a metamaterial with simultaneous ε' and μ' using split ring resonators (SRR) [2] and wires was demonstrated in the microwave regime [3], much attention has been put in extending negative index of refraction metamaterials to optical wavelengths [4]. The first idea was to scale down the artificial "atoms" to increase the resonance frequency at which the negative refractive index occurred. Unfortunately, there exist limits that prevent from increasing the frequency to an arbitrary high value as the metal stops to behave as an ideal one [5]. Another approach is to use metallo-dielectric stacks, a design with which negative refraction and superlensing have been numerically demonstrated in the visible [6]. Up to now, the best experimental designs are based on the so-called fishnet

structure composed of two perforated metal layers separated by a thin dielectric, rising wavelengths as small as 772 nm [7,8]. Here we propose a metamaterial composed of a single metal layer, which exhibits negative index of refraction for both polarizations and with low losses even in the visible range of the spectrum.

2. Negative index metamaterial

Metamaterials presenting resonant behavior in response to an incident magnetic field are often used to achieve effective negative μ. This is the case of a single SRR, which can be seen as a capacitance in series with an inductance, displaying negative permeability (unless stated explicitly, we refer to the real parts when we talk about permittivity, permeability or index of refraction) at the resonance frequency. Many other designs, such as parallel metal plates or stripes, have the same underlying physical mechanism [9,10]. This is the main reason why a periodic lattice of closed rings does not exhibit negative permeability since there is no capacitance to give the resonant behavior. Nevertheless, we can get negative μ' with closed square rings under certain conditions as in the structures depicted in Fig. 1. We start from a lattice of metal stripes (Fig. 1(a)) with thickness t and width w. The stripes are interrupted periodically by gaps of length s. The incidence is normal to the structure (see Fig. 1(e)) with the E field along the stripes and the H field perpendicular to them. As far as the electric response is concerned, the metamaterial acts as a dilute plasmonic medium, i. e., a metal with a lower plasma frequency than that in bulk. In addition, the cuts in the stripes give rise to a resonance in the permittivity. According to Faraday's law, the incident magnetic field induces an emf, which accounts for a current flow (thanks to a large thickness t of the stripes) in an open loop normal to the H field with opposite directions at each side of the gap. Since the current is interrupted by the gaps, we can consider the structure as an equivalent circuit which consists of an inductance in series with two capacitors, resulting in a resonant permeability that becomes negative in a certain band. This anti-symmetric mode generates a magnetic field that opposes the incident one above the resonance frequency, where the current phase is reversed, as Fig. 2 shows. Moreover, the permittivity is still negative in the magnetic resonance region giving rise to a negative index of refraction. Obviously, the metamaterial is sensible to polarization, in fact, it is almost transparent if we swap E and H. We can make it polarization independent by adding cut stripes normal to the original ones as in Fig. 1(d). The result is a symmetric medium made up of crosses very close to each other. We can go a step further and replicate the stripes (Fig. 1(b)). By doing so, we reinforce the magnetic resonance and shift it slightly. Note that the gap between the upper and lower stripes is of the same length as the one between horizontal stripes. Finally, we add double stripes parallel to H and obtain square rings exhibiting negative refraction in both polarizations.
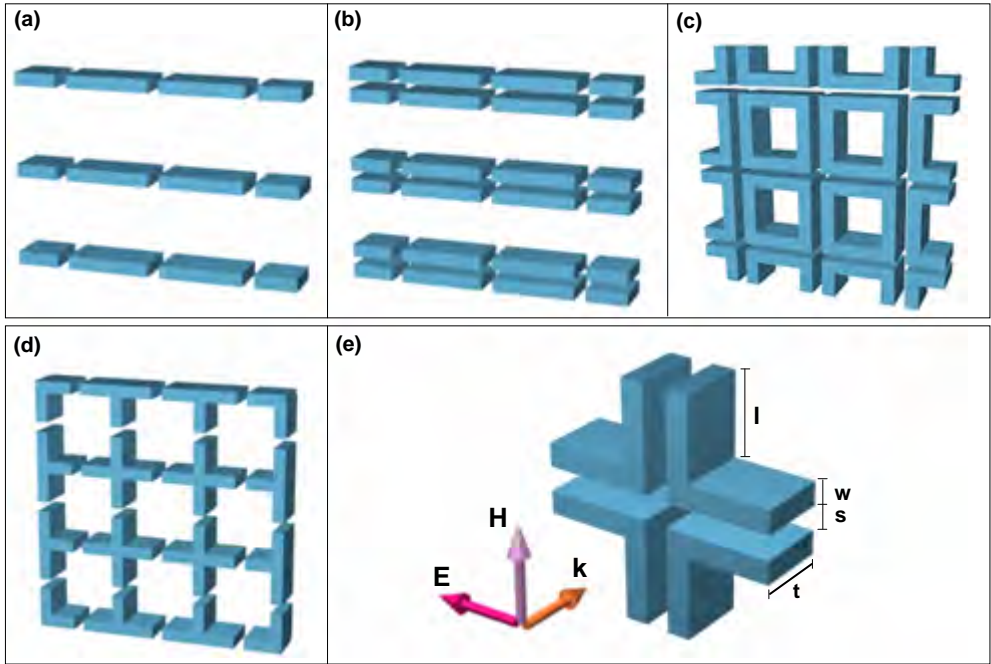
Fig. 1. (a) Basic metamaterial lattice. All other designs are derived from this one. (b) Double stripe metamaterial. (c) Square rings metamaterial (double stripes crossing in normal directions). (d) Cross-hair metamaterial (adding perpendicular stripes to structure in (a). (e) Unit cell of (c) and incident wave (same orientation for all structures).
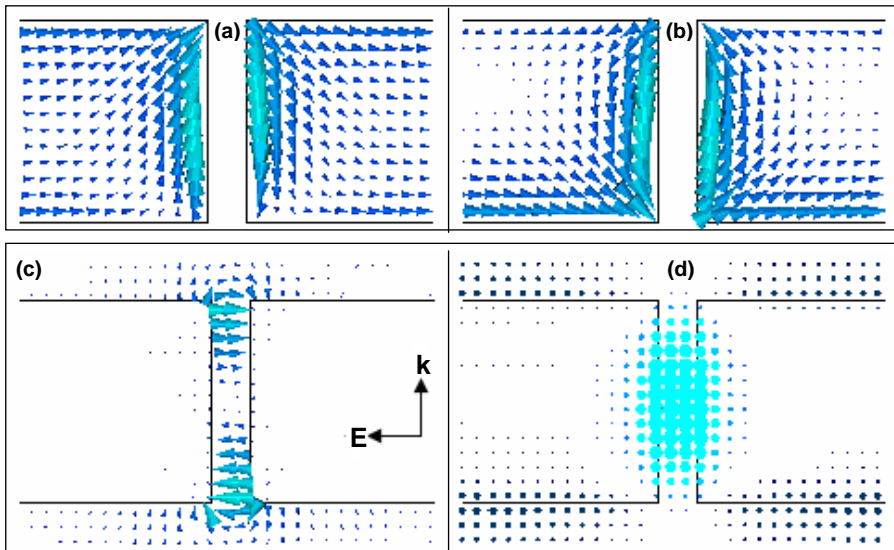
Fig. 2. Calculated currents and fields near the gap for design 1(a). Dimensions are the same as in Fig. 3. (a) Currents below magnetic resonance (450 THz). (b) Currents above magnetic resonance (510 THz) for the same phase of the incident wave. (c) Electric field (510 THz). (d) Magnetic field (510 THz). In all cases, the incident wave has the direction drawn in (c)

3. Numerical analysis

Numerical calculations are performed using a commercial 3D electromagnetic solver (CST Microwave Studio). We simulate a unit cell with periodic conditions along the dimensions normal to propagation and obtain the transmission (S_{21}) and reflection (S_{11}) parameters. Due to its low losses in the optical region, silver is chosen for the simulations. In addition, measured silver epsilon values [11] agree well with the Drude model for this metal in the range of interest, so the latter can be employed in the calculations. The plasma frequency for silver is $\omega_p = 1.37 \times 10^{16}$ s^{-1} and the collision frequency is chosen to match data from [11]. In order to check the validity of the Drude model we also use a best-fit first order Debbie approximation matching with the above-mentioned experimental values, obtaining very similar results. Current and field distributions are calculated below and above the magnetic resonance frequency and are shown in Fig. 2. In addition to the current loop generated by the magnetic field, there is another current directed along the stripes due to the electric field. As expected, the fields are concentrated in the gaps and we can see how the displacement current closes the loop.

To extract the effective n and z from the calculated S_{11} and S_{21}, the traditional retrieval method [12,13] is used. Then, ε and μ are obtained as $n = (\varepsilon\mu)^{1/2}$ and $z = (\mu/\varepsilon)^{1/2}$. As an example, we simulate all structures with $t = 150$ nm, $l = 106$ nm, $w = 54$ nm and $s = 30$ nm (in designs 1(a) and 1(b) the length of the stripes is $2l + 2w$ and their periodicity in the direction parallel to H is chosen to be the same as in their symmetric counterparts). The results are depicted in Fig. 3.

The use of an effective-medium model is justified since the structures dimension in the propagation direction is, depending on the design, from four to six times smaller than the wavelength. Moreover, the amplitude of high-order modes is negligible compared to the plane-wave one. Both the S parameters and extracted ε and μ are very similar for all designs verifying that the stripes parallel to the electric field are the ones responsible for the negative index behavior. There is a dip in S21 around 0.95 µm (no transmission) due to the resonance in ε, which is a consequence of the stripes not being continuous. The real part of the permeability has a strong resonance around 0.64 µm in all structures. At that frequency, the permittivity shows a characteristic antiresonant behavior [14] and is negative, except for the design 1(d) (although n' is negative). However, it is possible to adjust the geometrical parameters of this structure to make ε' and μ' negative in the same region as shown below. For the double stripe metamaterials (Figs. 1(b) and 1(c)), the permittivity becomes more negative, or equivalently, the effective plasma frequency gets higher. This can be ascribed to the higher metal filling factor in the direction normal to the electric field since the larger the filling factor is, the more the material resembles bulk metal. At this point, it is interesting to know how the negative index band shifts in frequency with dimensions scaling, being the most important variables the magnetic resonance frequency (f_{res}) and the effective plasma frequency (f_p). Since all structures have a very similar response, we will focus on the simplest one (structure in Fig. 1(a)).
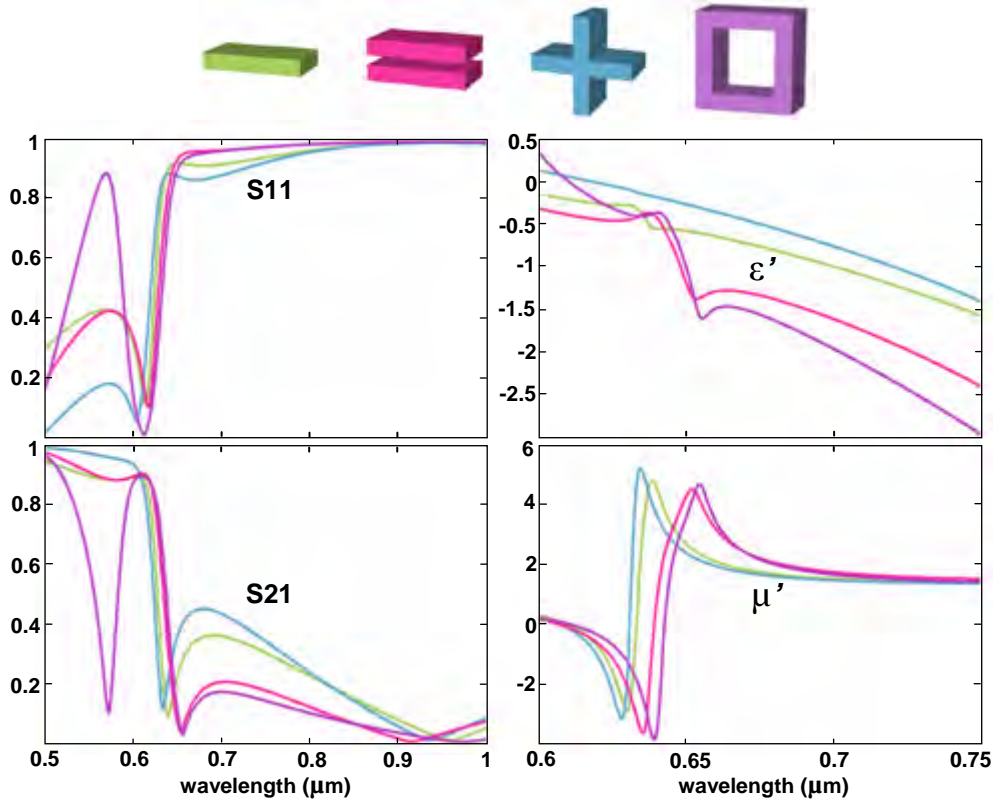
Fig. 3. S parameters and real parts of the permittivity and permeability of structures in Fig. 1.

It is appropriate to note that fabrication of the designs presented above is not straightforward due to the high ratio between thickness t and width w, which is of the order of 3:1. To overcome this difficulty we can increase the width w of the stripes and make it comparable to the thickness. Thus, we will scale the structure 1(a) with $t=w$ and depict the evolution of f_{res} and f_p with a geometrical scaling factor (S). As shown, f_{res} does not vary linearly with S as would occur with ideal metals or any metal at low frequencies. On the contrary, there exists saturation because the magnetic energy no longer dominates the kinetic one and both become comparable [5]. The effective plasma frequency varies almost in a linear fashion with S within this frequency range. There is a region ($S^{-1}<0.8$) where f_{res} is larger than f_p and therefore the refractive index is not negative. In Fig. 4(b) we can see that f_{res} increases when the spacing s grows whilst f_p remains almost unchanged. Hence, we have a way to invert the previous situation and make $f_{res}<f_p$ by decreasing s. The thickness t and width w also have influence in these two parameters and could be adjusted in order to tune the negative index band. As we scale down the structure s becomes too small, complicating its fabrication. To avoid this, we can make s larger and compensate the resonance shift by scaling up the metamaterial. For instance, if we take

the configuration of Fig. 4(b) with s = 30 nm, increase it to 50 nm and then apply $S \approx 1.1$, f_{res} remains in the same location.
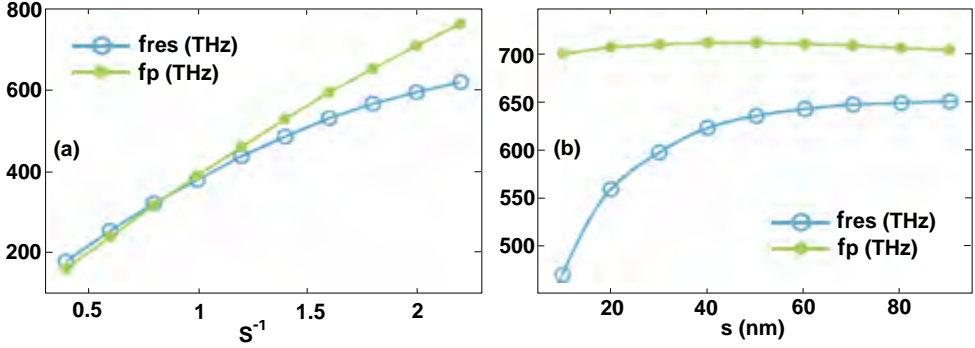
Fig. 4. (a) Dependence of f_{res} and f_p on scaling. The base structure (S=1) has dimensions $t=w$=220 nm, s=60 nm and a total stripe length equal to 440 nm. (b) Dependence of f_{res} and f_p on s. Dimensions are $t=w$=110 nm and 220 nm stripe length.

Regarding losses, the factor of merit (FOM) defined as FOM = $|n'/n''|$ is usually taken as a measure of how good the metamaterial behaves. We show in Fig. 5 the extracted n', ε', μ' and FOM for structure 1(a) with t = w = 110 nm, s = 60 nm and a stripe length equal to 220 nm. In this case, the FOM is larger than 6 at the wavelength where n' = -1 (464 nm). To our knowledge, this is the first metamaterial exhibiting negative refractive index at such high frequencies with only one metal layer.
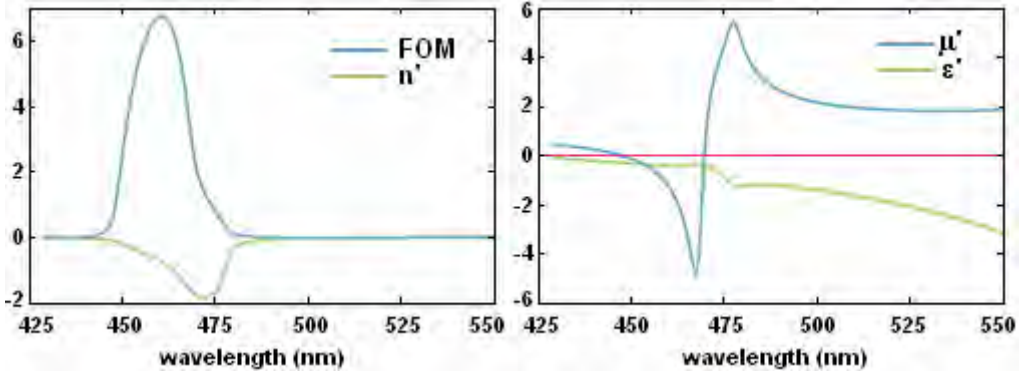
Fig. 5. Retrieved parameters for structure 1(a) with t = w = 110 nm, s = 60 nm and length 220 nm. Left: Factor of merit and real part of the refractive index. Right: Real parts of permittivity and permeability.

Finally, we suggest a 3D extension of the cross-shape metamaterial (see Fig. 6), which is expected to be isotropic. Its complexity is higher because of the fact that the magnetic field will also induce a current loop near the gap between the arms placed along the propagation direction, something that will influence the total magnetic response. In

principle, the electric response will remain almost unchanged since the electric field is normal to the added arms. The involved fabrication difficulty is the major drawback of this structure.

Fig. 6. Proposed 3D metamaterial.

4. Conclusion

In summary, we have presented a single-layer metamaterial based on cut stripes, which displays a negative index of refraction in a band that can be easily tuned over a wide range covering two regions of relevance, namely, the telecommunication (1550 nm) and visible regions of the spectrum, attaining frequencies as high as blue light or even greater. The metamaterial presents several advantages such as polarization independence and high factor of merit. Moreover, the simplicity of the cross-shape design with height equal or smaller than lateral dimensions makes it compatible with current techniques such as conventional lift-off process.

Acknowledgements

References

1. Ricardo A. Depine and Akhlesh Lakhtakia, "A new condition to identify isotropic dielectric-magnetic materials displaying negative phase velocity," Microwave Opt. Technol. Lett. **41**, 315-316 (2004).
2. J. B. Pendry, A. J. Holden, D. J. Robbins, and W. J. Stewart, "Magnetism from conductors and enhanced nonlinear phenomena," IEEE Trans. Microwave Theory Technol. **47**, 2075-2084 (1999).
3. R. A. Shelby, D. R. Smith, S. Schultz, "Experimental verification of a negative index of refraction," Science **292**, 77-79 (2001).
4. Costas M. Soukoulis, Stefan Linden, Martin Wegener, "Negative refractive index at optical wavelengths," Science **315**, 47-49 (2007).
5. J. Zhou, Th. Koschny, M. Kafesaki, E. N. Economou, J. B. Pendry, and C. M. Soukoulis, "Saturation of the magnetic response of split-ring resonators at optical frequencies," Phys. Rev. Lett. **95,** 223902 (2005).

6. Michael Scalora *et al.*, "Negative refraction and sub-wavelength focusing in the visible range using transparent metallodielectric stacks," Opt. Express **15**, 508-529 (2007).
7. G. Dolling, M. Wegener, C. M. Soukoulis, S. Linden, "Negative-index metamaterial at 780 nm wavelength," Opt. Lett. **32**, 53-55 (2007).
8. U. K. Chettiar, A. V. Kildishev, H.-K. Yuan, W. Cai, S. Xiao, V. P. Drachev, and V. M. Shalaev, "Dual-band negative index metamaterial: Double-negative at 813 nm and single-negative at 772 nm," http://arxiv.org/ftp/physics/papers/0612/0612247.pdf.
9. Zhiming Huang, Jianqiang Xue, Yun Hou, Junhao Chu, and D.H. Zhang, "Optical magnetic response from parallel plate metamaterials," Phys. Rev. B **74**, 193105 (2006).
10. Vladimir M. Shalaev, Wenshan Cai, Uday K. Chettiar, Hsiao-Kuan Yuan, Andrey K. Sarychev, Vladimir P. Drachev, and Alexander V. Kildishev, "Negative index of refraction in optical metamaterials," Opt. Lett. **30**, 3356-3358 (2005).
11. P.B. Johnson and R. W. Christy, "Optical Constants of the Noble Metals," Phys. Rev. B **6**, 4370-4379 (1972).
12. D. R. Smith, S. Schultz, P. Markos, and C.M. Soukoulis, "Determination of effective permittivity and permeability of metamaterials from reflection and transmission coefficients," Phys. Rev. B **65**, 195104 (2002).
13. Xudong Chen, Tomasz M. Grzegorczyk, Bae-Ian Wu, Joe Pacheco, Jr., and Jin Au Kong, "Robust method to retrieve the constitutive effective parameters of metamaterials," Phys. Rev. E **70**, 016608 (2004).
14. T. Koschny, P. Markos, D. R. Smith, and C. M. Soukoulis, "Resonant and antiresonant frequency dependence of the effective parameters of metamaterials," Phys. Rev. E **68**, 065602 (2003).

2.11

PAPER 6. METAMATERIALS FOR OPTICAL SECURITY

Metamaterials for optical security

A. Martínez,[a] C. García-Meca,[b] R. Ortuño, F. J. Rodríguez-Fortuño, and J. Martí

Nanophotonics Technology Center, Universidad Politécnica de Valencia, Camino de Vera s/n
46022, Valencia, Spain

[a]amartinez@ntc.upv.es
[b]cargarm2@ntc.upv.es

ABSTRACT

In this letter we introduce the concept of optical security marks based on photonic metamaterials. We propose that a metamaterial with strong negative magnetic activity in the visible wavelength regime can be used to create a security mark that can be incorporated in any object to ensure its authenticity. The sophisticated nanofabrication processes needed to manufacture the metamaterial contribute to avoid counterfeiting. To illustrate the concept, a particular configuration consisting of silver nanohoops is analyzed.

Metamaterials (MMs) are artificial composites whose electric and magnetic responses to incoming waves can be independently controlled to produce unexpected phenomena. Initial interest in MMs was focused on finding a left-handed MM in which the real parts of the relative electric permittivity ε_r and magnetic permeability μ_r were simultaneously negative. Veselago [1] predicted more than 40 years ago that such a composite would refract light negatively, and this phenomenon was experimentally demonstrated in 2001 at microwave frequencies [2]. Since then, MMs research has widened to include not only negative refraction but also the complete tailoring of both ε_r and μ_r to achieve whatever index of refraction $n = (\varepsilon_r \mu_r)^{1/2}$ and medium impedance $\eta = (\mu/\varepsilon)^{1/2}$. In principle, this striking behavior can be achieved even in the optical regime where natural substances do not display magnetic activity ($\mu_r = 1$).

Three main applications have been suggested to exploit the striking properties that MMs provide in the optical domain: the perfect lens [3], which permits subwavelength focusing of a point source; cloaking [4], which permits to cloak a given object from external radiation; and the "trapped rainbow" waveguide, which would allow for slowing down and ultimately stopping light propagation [5]. All these cases have something in common: a three-dimensional (3D) MM with tailored values of ε_r and μ_r and low absorption is required, which is extremely challenging from the fabrication point of view in the optical domain. Even in the simplest case, the perfect lens, in which an isotropic 3D optical MM with $\varepsilon_r = \mu_r = -1$ is required, the practical realization is currently out of reach. Therefore, it makes sense to use the unexpected properties of MMs in simpler ways to develop new functionalities and applications. Here we propose that *a*

photonic MM can be used as a security mark to be attached to a certain object with the aim of providing an authenticity signature (or optical fingerprint). In this case, the MM must provide a special behavior ($|\mu_r'| \gg 1$ and $\mu_r' < 0$, μ_r' being the real part of the complex μ_r') exclusively in one direction, so this device could be produced without requirements for complex 3D nanostructuring.

Optical security marks are incorporated in a broad variety of ordinary objects, for instance, bank notes [6]. Most current approaches make use of holographic, interference or diffractive techniques so the object authenticity can be established with simple visual inspection (first line inspection). Other marks use more complex authentication procedures which can be classified as second- or third-line inspection techniques. In any case, optical security devices include optical features that are difficult to reproduce or mimic by other means [6]. For instance, diffractive gratings provide a more secure performance than techniques based on subtractive color mixing since their manufacture requires particular tools and processes which are not available to the general public [6]. As mentioned above, MMs display features that cannot be achieved by standard, natural materials. Based on this idea, some of the MMs properties (negative refraction, superlens) can be efficiently mimicked by using other structures, such as dielectric photonic crystals [7,8]. However, there is a supposed property that can only be achieved by use of nano-structured MMs: *magnetism* ($\mu_r' \neq 1$) *at optical frequencies*. This is the main basis of the optical security mechanism we propose.

The idea is as follows. MMs with artificial magnetism can be created by properly synthesizing their constituting meta-atoms [9]. Let us consider that the size (period) of the meta-atom is *a*, *the smallest spatial detail in the meta-atom* (for instance, the gap in a split-ring-resonator) [9] *is d* and the wavelength at which the artificial magnetism occurs is λ. To ensure an effective response of the MM, $\lambda \gg a > d$ must be accomplished at least in the direction of propagation of light [10]. Additionally, by scaling down the MM and reducing *a*, the artificial magnetism will be pushed towards higher frequencies (lower λ) [11]. Above gigahertz frequencies, the only means to produce magnetism is by use of MMs, since natural substances are magnetically inert at those frequencies [10]. The higher the frequency for $\mu_r' \neq 1$, the smaller *a* and *d* will be needed in order to produce a magnetic response. This also means that very sophisticated nano-fabrication processes will be required to manufacture MMs with $\mu_r' \neq 1$ at very high frequencies. For instance, in Ref. 11, $\lambda = 3$ μm, $d = 70$ nm and $a = 450$-900 nm (λ is between 6.66 and 3.33 times the period).

In this miniaturization route towards higher frequencies, it has been usual to fabricate single layer MMs onto planar substrates [12]. 3D MMs can be obtained by stacking several layers [10]. The parameters ε_r and μ_r of these layers are typically obtained from transmittance and reflectance measurements by a retrieval procedure [13]. If this procedure is *unambiguous*, a certain effective μ_r can be assigned to a certain MM at a given wavelength λ. Then we can state that the value $\mu_r(\lambda)$ is an optical fingerprint of the material which cannot be counterfeited but by use of another MM with similar magnetic properties. Since achieving magnetic activity is challenging at optical wavelengths owing to inherent physical limitations [12], it will be even more complicated

to engineer a MM with strong negative magnetism ($|\mu_r'| \gg 1$, $\mu_r' < 0$). We choose $\mu_r' < 0$ since in general it is more complicated to achieve largely negative values of the permeability than largely positive ones. In addition, the manufacture of this MM at very high frequencies (visible spectrum) will require technological processes with resolutions well below 100 nm. Such processes should also enable high-volume production of large-area nano-structured metallic layers since the application will require mass-scale manufacturing. Therefore, these processes will only be available in a limited amount of foundries, which enormously restricts the possibility of producing illegal copies (counterfeiting) of the original MM, the main barrier for counterfeiters. Then, we can conclude that the physical as well as technological difficulties in achieving this behavior at very high frequencies is a natural means to avoid counterfeiting of the MM mark since the tools required to produce it can be under control [6].

Therefore, we could think of attaching a MM mark to a certain object to avoid counterfeiting, as shown in Fig. 1(a). From the MM response to illumination we could retrieve [13] the fingerprint, which in our case is the magnetic permeability, and test the authenticity of the object. The concept can be easily extended to arrays of MM mark cells, each one providing a certain matrix fingerprint ($\mu_{ri,j}$) so that a magnetic code is given to the object, which gives an additional security step.
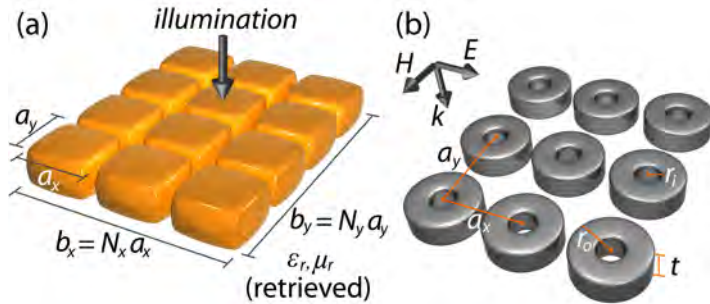
Fig. 1. (a) $N_x \times N_y$ meta-atoms with dimensions a_x and a_y that form a security mark. (b) Nanohoops MM as a security mark.

Now we will illustrate the ideas set forth so far with an example. Specifically we will consider the MM whose unit cell is a silver planar nano-hoop with inner radius r_i, outer radius r_o, and thickness t [see Fig. 1(b)] as a suitable candidate to implement security marks. The reason to use this structure is that it can be engineered to exhibit a very strong magnetic resonance in the visible spectrum as compared with other proposed magnetic structures in the same regime. Moreover, the strength and spectral position of the resonance are easily tunable as shown below. The choice of silver is due to its low loss in the visible regime. To obtain the electromagnetic response of this structure, we have performed a series of numerical simulations using CST Microwave Studio. In the simulations, the permittivity of silver has been described by means of the Drude model

$\varepsilon_d(\omega) = 1 - \omega_p^2/(\omega^2 - i\omega\cdot\omega_c)$ with a plasma frequency $\omega_p = 1.37\times10^{16}$ s⁻¹ and a collision frequency $\omega_c = 6\times10^{13}$ s⁻¹. This last value is somewhat higher than that in bulk because losses increase when the metal is nanostructured. Nevertheless, the exact value of ω_c can only be retrieved from experiment. The effective ε_r and μ_r of the medium are retrieved from the calculated reflection and transmission coefficients using the method described in Ref. 13. As shown in Fig. 1, we consider only normal incidence, with the electric field E along the x direction. In that case, the proposed MM exhibits a strong magnetic response whose origin is a magnetic plasmon resonance similar to that taking place in an array of split ring resonators (see Refs. 14-15 and references therein). Several magnetic MMs are based on this kind of resonance [10-11]. In the case of the nanohoops, the resonance takes place in the gap between neighboring nanohoops where an antisymmetric mode is induced by the magnetic field H. It is responsible for the virtual current loop (VCL) that appears around the gap with currents flowing in opposite directions at each side of the gap and that is closed by displacement currents. We can see this in Fig. 2(a) where we show the currents excited in two adjacent nano-hoops and the E field in the XZ plane that crosses the nano-hoops center. The VCL and the E field that forms the displacement currents at the gap ends can be clearly observed.
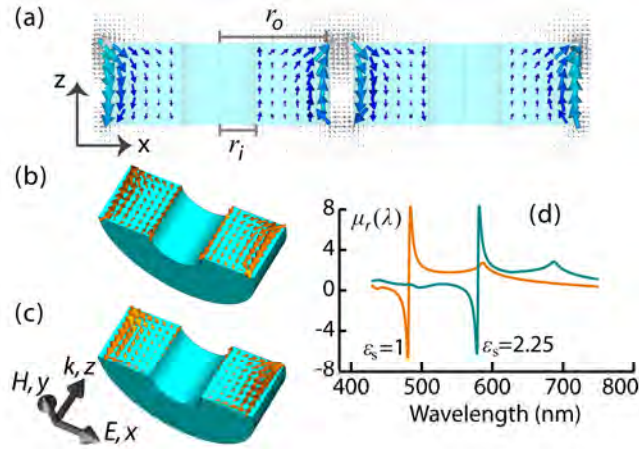
Fig. 2. (a) Electric currents (blue arrows) and E field (gray arrows) of a nanohoop MM in an XZ plane cut at $\lambda_m = 480$ nm. (b) Currents at $\lambda=500$ nm. (c) Currents at $\lambda = 460$ nm. (d) μ_r' with $\varepsilon_s = 2.25$ and $\varepsilon_s = 1$. In all cases $r_i = 50$ nm, $r_o = 150$ nm, $a_x = 330$ nm, $a_y = 420$ nm, and $t = 110$ nm.

Regarding the magnetic resonance, the structure can be considered as an equivalent LC circuit which is going to resonate at a certain wavelength λ_m. For instance, if $r_i = 50$ nm, $r_o = 150$ nm, $a_x = 330$ nm, $a_y = 420$ nm and $t = 110$ nm, then $\lambda_m \approx 480$ nm. Figures 2(b) and 2(c) show the currents below and above λ_m at the same incident wave phase for a MM with the previous dimensions. They are clearly running out of phase. Below λ_m,

these currents create a magnetic field that opposes the incident one and give rise to a large negative μ_r'. This negative μ_r' region is within the visible spectrum, where strong artificial magnetism fits perfectly well with the idea of optical security described above. Obviously, the MM must be fabricated on a substrate. Nonetheless the presence of a low-index substrate hardly alters the MM response as the fields are mainly concentrated in the gaps between adjacent nanohoops. The only noticeable effect of the substrate addition is a slight resonance redshift. To show this, we simulate the nano-hoops MM with the previous dimensions with and without a semi-infinite substrate. The retrieval of the effective MM parameters in the presence of the substrate can be done using a simple transfer matrix formalism [15]. In Fig. 2(d) we depict μ_r' for the two cases. A typical glass permittivity ε_s=2.25 was used to model the substrate. The μ_r' obtained with substrate is almost the same as for the free-standing case but redshifted by 100 nm approximately, keeping the resonance within the visible spectrum. For this reason and for computational simplicity, the substrate was not considered in the rest of simulations.

If we want to associate a discrete (or continuous) code or fingerprint with a set (or interval) of negative values of μ_r', it could be desirable to control the intensity of the magnetic resonance somehow. Looking at the resonant currents, we can observe that as we reduce r_i for a given r_o, the spatial extension of these currents increases, strengthening the magnetic resonance. In Fig. 3(a) we have depicted μ_r' as a function of r_i, keeping the other dimensions unchanged. We can see that λ_m is hardly altered by the variation in r_i. This slight shift could be corrected by adjusting a_x. Nevertheless, this is not needed, since the spectral positions of λ_m for the different values of r_i are so close that we have a nice succession of μ_r' values at, for instance, $\lambda_0 = \lambda_m|_{r_i = 0} = 476$ nm. We have depicted this set of μ_r' values in Fig. 3(b).
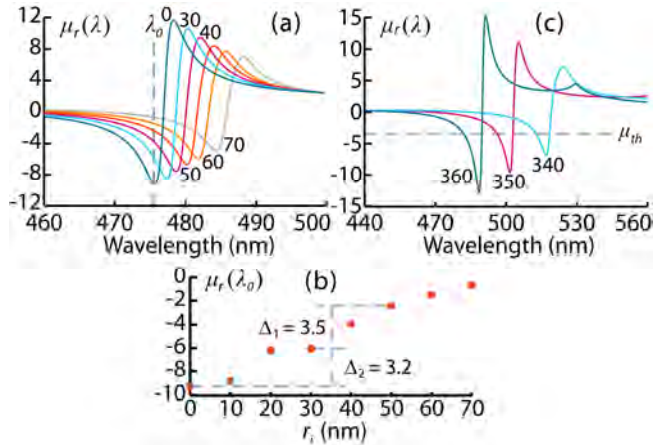
Fig. 3. (a) μ_r' of a nanohoop MM with r_o = 150 nm, a_x = 330 nm, a_y = 420 nm, t = 110 nm. Legend: r_i in nm. (b) μ_r' values of (a) at λ_0 = 476 nm as a function of r_i. (c). μ_r' of a nanohoop MM with r_i = 0 nm, r_o = 160 nm, a_y = 440 nm, and t = 120 nm. Legend: a_x in nm.

As an example, and for optical security purposes, we could create a ternary code where we assign the symbol "0" to μ_r' (475nm) = -9.2, the symbol "1" to μ_r' (475nm) = -6, and the symbol "2" to μ_r' (475nm) = -2.5 (*i.e.*, the μ_r' values corresponding to $r_i = 0$, $r_i = 30$, and $r_i = 50$, respectively). The considerably wide gaps ($\Delta_1 = 3.2$ and $\Delta_2 = 3.5$) between the values of μ_r' associated with consecutive symbols give us a good error tolerance regarding both fabrication and detection. For equally probable symbols, we should use the middle point between each adjacent μ_r' couple as detection thresholds, in such a way that our "detector" would choose symbol "0", "1" or "2" if μ_r' (475nm) $\in$ [-∞,-7.6], [-7.6,-4.25] or [-4.25,0], respectively. In this case we have extended the first interval to -∞ and the last to 0 because they are at the extremes (note that we do not extend the last interval to ∞, since our code works only with negative μ_r' values).

We could also create a wavelength-based code by engineering the MM dimensions so as to have several configurations, each providing a negative magnetic response in a different spectral band. If these bands do not overlap, it would be possible to assign a different symbol to each frequency channel. In Fig. 3(c) we have plotted μ_r' for three different nanohoop-based MM configurations designed with this purpose and differing only in the value of a_x. Each of them exhibits a strong negative magnetic response but centered at three different equidistant frequencies: 580 THz (517 nm), 597 THz (503 nm), and 614 THz (489 nm). It is worth pointing out that although the strength of each resonance is different, the weaker one reaches $\mu_r' = -7$, a value negative enough for our purpose. This is because we used only a_x as a free design parameter for fabrication easiness (the resonance strength also varies with a_x). Nevertheless, the strength of the resonances can be leveled modifying other structure dimensions. Following our ternary code example, we could identify symbol "0", "1" or "2" with $\mu_r' < \mu'_{th}$ occurring at $\lambda \in$ [470,496] nm, $\lambda \in$ [496,510] or $\lambda \in$ [510,530] nm, respectively, μ'_{th} being a security threshold. The extreme points (470 and 530 nm) have been chosen quite arbitrarily as they will depend on the particular implementation of the authentication system. Obviously the previous examples can be extended to codes with larger alphabets or to the continuous case. In addition, other MMs different from the one described here could be potentially used to achieve the required magnetism in the visible or near infrared spectra [16-18]. Since all of them require nano-structuring of metal layers, the most advanced manufacturing tools are needed, thus preventing the possibilities for counterfeiting the security mark.

In summary, we propose that photonic MMs engineered to display strong magnetism at high frequencies can be used as a security mark to ensure the authenticity of goods. Since this application does not require for 3D low loss MMs, we think that it is a good candidate to become a high impact application of photonic MMs in the short term.

Acknowledgements

References

1. V.G. Veselago, Sov. Phys. Usp. **10**, 509 (1968).
2. R. A. Shelby, D. R. Smith, and S. Schultz, Science **292**, 77 (2001).
3. J. B. Pendry, Phys. Rev. Lett. **85**, 3966 (2000).
4. D. Schurig, J. J. Mock, B. J. Justice, S. A. Cummer, J. B. Pendry, A. F. Starr, and D. R. Smith, Science **314**, 977 (2006).
5. K. L. Tsakmakidis, A. D. Boardman, and O. Hess, Nature (London) **450**, 397 (2007).
6. R. L. van Renesse, *Optical Document Security*, 3rd ed. (Artech-House, Boston, 2005).
7. A. Martínez and J. Martí, Phys. Rev. B **71**, 235115, (2005).
8. A. Martinez and J. Marti, Opt. Express **13**, 2858-2868, (2005).
9. J. B. Pendry, A. J. Holden, D. J. Robbins, and W. J. Stewart, IEEE Trans. Microwave Theory Technol. **47**, 2075 (1999).
10. J. Valentine, S. Zhang, T. Zentgraf, E. Ulin-Avila, D. A. Genov, G. Bartal, and X. Zhang, Nature **455**, 376 (2008).
11. S. Linden, C. Enkrich, M. Wegener, J. Zhou, T. Koschny, and C. M. Soukoulis, Science **306**, 1351 (2004).
12. C. M. Soukoulis, S. Linden, and M. Wegener, Science **315**, 47 (2007).
13. X. Chen, T. M. Grzegorczyk, B. Wu, J. Pacheco, Jr., and J. A. Kong, Phys. Rev. E **70**, 016608 (2004).
14. H. Liu, D.A. Genov, D.M. Wu, Y.M. Liu, J.M. Steele, C. Sun, S.N. Zhu, and X. Zhang, Phys. Rev. Lett. **97**, 243902 (2006).
15. A.V. Kildishev, W. Cai, U.K. Chettiar, H. Yuan, A.K. Sarychev, V.P. Drachev, and V.M. Shalaev, J. Opt. Soc. Am. B **23**, 423 (2006)
16. C. García-Meca, R. Ortuño, R. Salvador, A. Martínez, and J. Martí, Opt. Express **15**, 9320 (2007).
17. C. García-Meca, R. Ortuño, F. J. Rodríguez-Fortuño, J. Martí, and A. Martínez, Opt. Lett. **34**, 1603 (2009).
18. C. García-Meca, R. Ortuño, F. J. Rodríguez-Fortuño, J. Martí, and A. Martínez, Opt. Express **17**, 6026-6031 (2009).

Transformation optics

Analogies play an important role in physics. First, once we find an analogy between a well-established branch of physics and an emergent one, we are able to use immediately all the knowledge and results of the former for the latter. Second, they provide alternative ways of looking at a certain theory and the possibility of performing originally out-of-reach experimental work through the analogue phenomenon, which provides a technologically accessible laboratory environment. Analogue gravity is one the most celebrated of these analogies, as it enables us to gain theoretical insight and probe features of curved spacetime physics, whose existence in nature cannot be verified with current technology and knowledge. In turn, general relativity may also shed light to some aspects of the analogue model. The first examples on the concept of gravity analogues originated in relation to acoustics[84], as it was shown that supersonic fluid flow can generate an acoustic analogue of a black hole. From then on, several theoretical proposals and experimental works have followed[85,86]. A remarkable aspect of analogue gravity is that non-relativistic phenomena are found to be governed by a curved Lorentzian (pseudo-Riemannian) geometry. As a consequence, the mathematical machinery of general relativity proves to be useful in other fields of physics.[8,85,87,88].

Along this line, transformation optics is an emerging field (first proposed in 2006)[4,5] that enables us to create curved geometries for light by suitably changing the optical medium it propagates through.[89] Usually, the electromagnetic properties (constitutive parameters) required for the implementation of the above-mentioned curved geometries cannot be found in nature. However, the recent development of metamaterials facilitate the synthesis of such exotic media. Thus, with the aid of metama-

terials, transformation optics provides a new arena for creating optical devices that would be extremely difficult to achieve with classical design methods. There already exist several interesting theoretical proposals and experimental work in this branch of research, which has been cited by Science as one of the ten top scientific discoveries of the last decade, as we mentioned in the introduction. Among the most striking proposals we can find cloaking devices,[4,5], electromagnetic wormholes,[90] or black holes,[91] to name a few. Transformation optics even provides a geometrical interpretation of the negative-index superlens[91,92] studied in the previous chapter, as well as of a positive-index alternative[93].

3.1   Fundamentals

The concept underlying transformation optics is outlined in Figure 3.1. Note that we have employed the standard notation of differential geometry, which we will keep throughout the entire chapter, as it provides a general, compact and elegant way of presenting the theory.

Figure 3.1: Transformation optics concept

1. *Virtual space*		**2**. *Virtual space*		**3**. *Physical space*
$x^{\mu'}, g^{\mu'\nu'}$	$f: x^{\mu'} \to x^{\mu''}$	$x^{\mu''}, g^{\mu''\nu''}$	*Formally equivalent*	$x^{\mu}, \bar{g}^{\mu\nu}$
$X^{\mu'\nu'\rho'\sigma'}$		$X^{\mu''\nu''\rho''\sigma''}$		$\bar{X}^{\mu\nu\rho\sigma}$

We start from an imaginary *virtual space* in which we know how electromagnetic fields behave (stage 1 in Figure 3.1). This space is filled with a certain medium characterized by a constitutive tensor $X^{\mu'\nu'\rho'\sigma'}$. The constitutive tensor contains all the properties of the medium, including its permittivity ε, permeability μ and bianisotropy tensor κ in the most general linear form.[94] In Figure 3.2 we show its main components (the other can be obtained from symmetry considerations[94]).

We choose a certain coordinate system for this space so that *spacetime* points have coordinates $x^{\mu'}$. In addition, the metric of virtual space in the coordinates $x^{\mu'}$ is $g^{\mu'\nu'}$, which contains the information about its curvature. Now we want the fields to propagate in some other way resulting from a geometrical

distortion of this initial situation.

$X^{\mu\nu\rho\sigma}$	$\rho\sigma$	01	02	03	23	31	12
	$\mu\nu$						
Permittivity matrix	01	$-\varepsilon^{11}$	$-\varepsilon^{12}$	$-\varepsilon^{13}$	κ^{13}	κ^{23}	κ^{33}
	02	$-\varepsilon^{12}$	$-\varepsilon^{22}$	$-\varepsilon^{23}$	κ^{21}	κ^{22}	κ^{23}
	03	$-\varepsilon^{13}$	$-\varepsilon^{23}$	$-\varepsilon^{33}$	κ^{31}	κ^{32}	κ^{33}
Bianisotropy	23	κ^{11}	κ^{21}	κ^{31}	χ^{11}	χ^{12}	χ^{13}
	31	κ^{12}	κ^{22}	κ^{32}	χ^{12}	χ^{22}	χ^{23}
	12	κ^{13}	κ^{23}	κ^{33}	χ^{13}	χ^{23}	χ^{33}

← Bianisotropy (row 02)

← Inverse permeability matrix

Figure 3.2: Constitutive tensor relevant components.

Such a distortion can be encoded by a mapping $f : x^{\mu'} \rightarrow x^{\mu''}$. The fields follow the desired "paths" when expressed in the new coordinates $x^{\mu''}$, as their value at $x^{\mu'}$ now takes place at $f(x^{\mu'})$ (with some rescaling factors arising from the fields tensorial character). However, this is just a representation illusion, since, in spite of having changed the coordinate system, we are still in virtual space (stage 2 in Figure 3.1) and nothing physical has changed. In this new coordinate system, the metric of virtual space is $g^{\mu''\nu''}$, which still represents the same curvature, and the constitutive tensor is $X^{\mu''\nu''\rho''\sigma''}$, which still represents the same medium too. At this point comes the smart contribution of transformation optics. Maxwell's equations in a space with a certain metric $g^{\mu''\nu''}$ filled with a medium $X^{\mu''\nu''\rho''\sigma''}$ are formally equal to Maxwell's equations in another space with a metric $\bar{g}^{\mu\nu}$ and filled with the appropriate medium $\bar{X}^{\mu\nu\rho\sigma}$, if we interpret the coordinates $x^{\mu''}$ as those in physical space. In practical terms, although we cannot change the metric of the space we live in (which we call *physical space*) or view it in another coordinate system, we can fill it with a wide variety of media (partly thanks to metamaterials). Thus, we are able to force electromagnetic fields to follow the same desired paths as they would do in our distorted and/or curved virtual space (stage 2), but now in the real physical — and effectively flat (usually) — space we live in (stage 3), if the latter is filled with a suitable medium. The following interesting effects can be achieved from the scenario depicted in Figure 3.1:

- Coordinate transformation: In this case, virtual and physical space are the same (the metrics $g^{\mu'\nu'}$ and $\bar{g}^{\mu\nu}$ represent the

same curvature, usually that of Euclidean space). We only want to implement the distortion undergone by the fields under the mapping f (step from stage 1 to stage 2). For that, the coordinates $x^{\mu''}$ are interpreted as those in physical space x^μ, which is also filled with the appropriate medium $\bar{X}\mu\nu\rho\sigma$ to mimic the metric $g^{\mu''\nu''}$, as mentioned above. In most cases, virtual and physical space (stages 1 and 3) are expressed in the same coordinate system and the coordinates $x^{\mu'}$ and x^μ, as well as the metrics $g^{\mu'\nu'}$ and $\bar{g}^{\mu\nu}$, coincide. In virtual space (stage 2), the fields follow the desired paths as a result of the chosen representation (coordinates $x^{\mu''}$), while in physical space they follow the same paths because of the medium, which makes light virtually experience the same space (virtual space, stage 2). The first invisibility cloaks belong to this class.

- Implementation of a curved geometry: We start from a curved virtual space (stage 1), which is mapped through f to another space (virtual space, stage 2). This space has the same curvature as in stage 1, but we have distorted the fields in the way we want them to appear in physical space. In the final step, this virtual space is interpreted as flat space filled with a medium (stage 3) — again, we need to interpret the coordinates $x^{\mu''}$ as the coordinates x^μ. Then, the transformation f is effectively mapping virtual curved space to physical flat space. Maxwell's fisheye is an example of this class. It might be possible that we want to implement a curved space in flat space just as it is, without distortion. In this case, f would be the identity map, while $\bar{X}^{\mu\nu\rho\sigma}$ would simply mimic the metric $g^{\mu'\nu'}$.

Up to now, we have only described transformation optics with words. The associated mathematics, which essentially provides us with a recipe for the constitutive parameters required to implement a certain coordinate transformation and/or curved geometry, can be derived from Maxwell's equations, as it was done in the first versions of the theory and subsequent refinements.

A general expression for the medium and the sources with which physical space must be filled in order to mimic the geometry of an empty curved virtual space (stage 2), as a function

of the metrics of both spaces is[95]

$$X^{\mu\nu\rho\sigma} = \frac{\sqrt{-g'}}{\sqrt{-g}}\left(g'^{\mu\rho}g'^{\nu\sigma} - g'^{\mu\sigma}g'^{\nu\rho}\right) \quad \text{and} \quad j^{\alpha} = \frac{\sqrt{-g'}}{\sqrt{-g}}j'^{\alpha}. \tag{3.1}$$

Here j^{α} denotes the four-current.[95] We must bear in mind that virtual space (stage 2) could be the result of a coordinate transformation from virtual space in other coordinate system (stage 1). Extension to the case in which virtual space is non-empty is simple.

In the following, we only work with space — as opposed to spacetime — transformations. Therefore, it would be interesting to have a simplified version of Eq. (3.1) for this particular case. We can do this by taking into account that for pure spatial curvatures and coordinate transformations, $g^{00} = -1$ and $g^{i0} = g^{0i} = 0$. From Figure 3.2 and Eq. (3.1) we arrive at[1]

$$\varepsilon^{ij} = -X^{0i0j} = -\frac{\sqrt{-g'}}{\sqrt{-g}}\left(g'^{00}g'^{ij} - g'^{0j}g'^{i0}\right) = \frac{\sqrt{\gamma'}}{\sqrt{\gamma}}\gamma'^{ij} \tag{3.2}$$

It can be shown that the same result is obtained for μ^{ij}.

> [1] γ^{ij} is the "spatial part" of the spacetime metric $g^{\mu\nu}$, in such a way that $\gamma^{ij} = g^{ij}$, where Latin indices run from 1 to 3, while Greek indices run from 0 to 3. Note that $\gamma = \det\left(\gamma_{ij}\right)$ and $g = \det\left(g_{\mu\nu}\right)$ are the determinants of the covariant metrics.

3.2   Examples of transformation-optics-based devices

In this section we describe some key devices that have heavily influenced the development of transformation optics.

Invisibility cloak

Undoubtedly, the application that boosted transformation optics and defined the focus of subsequent research in this field is the invisibility cloak. Indeed, two different kinds of cloak were chosen by the creators of transformation optics to exemplify the first versions of the theory. The common basic idea is to use a transformation that opens a hole in space and then use the appropriate medium to implement such a transformation. For instance, a two-dimensional transformation of this form is (see Figure 3.3)

$$r = \frac{b-a}{b}r' + a,$$
$$\phi = \phi', \tag{3.3}$$
$$z = z',$$

(a)

(b)
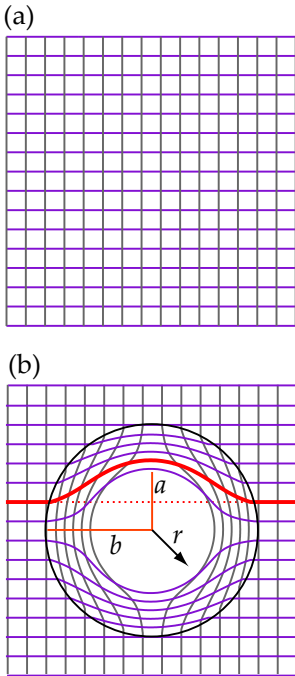
Figure 3.3: Coordinate transformation opening a hole in space

where we have used a cylindrical coordinate system for virtual space (primed coordinates). This transformation compresses the region $0 < r' < b$ in virtual space into the region $a < r < b$ in physical space, where the cloak (medium implementing the transformation) is located. In the region $r > b$, virtual space is unchanged and it is not necessary to use any medium.

On the other hand, the fields attempting to enter the region $r < a$ are deflected and guided around it by the cloak, which finally return them to their original trajectory, as if they had passed through empty space. This is valid for waves as well as for rays, as the one depicted in red in Figure 3.3(b), whose original trajectory (in the absence of the cloak) is represented as a dashed line, and coincides with the modified trajectory (in the presence of the cloak) in the region $r > b$. Since the fields never get into the region $r < a$, any object inside this region is invisible for them and also for an external observer, who cannot detect the cloak or the objects inside it, as the original field distribution (the one that would exist in the absence of cloak and objects) in the region $r > b$ is unaltered by the cloak. Note that the cloak works for any radiation impinging onto it from any point in any direction, as shown in Figure 3.4.

The first experimental demonstration of such an invisibility cloak was reported in 2006 at microwave frequencies[96] and there exist theoretical proposals for the visible range.[97] Cloaking devices are not restricted to cylindrical or spherical shapes. The same concept can be applied to any other shape, as in the example in Figure 3.5, where we show the cloaking effect for waves. Recent design methods allow the numerical calculation of the constitutive parameters of a cloak with any shape.[98]
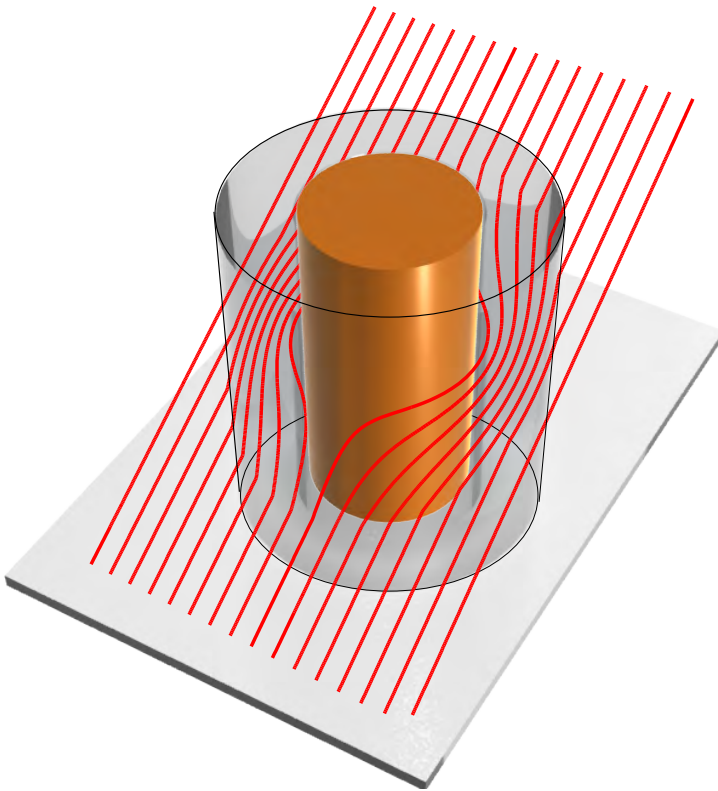
Figure 3.4: Performance of a cloaking device. The cloak (shaded region) bends rays around a certain region of space, preventing them from entering there. After exiting the cloak, the rays continue their paths as if there was nothing in their way. Anything inside the hole (metallic cylinder in this case) is rendered invisible.

However, perfect cloaking devices like the ones we have just described suffer from a fundamental drawback. The point $r' = 0$ in virtual space has turned into the line $r = a$ in physical space. The time it takes light to pass through a point is zero, but this is not true anymore in physical space, since light has to make a detour around the invisible region in the same time. Covering a finite distance in zero time requires an infinite phase

velocity —infinite refractive index, roughly speaking. Materials with almost infinite light phase velocity are possible, but only for discrete frequencies. The other original approach for cloaking is less demanding as it only requires a zero refractive index at two points.[4] In addition, since it is based on conformal mappings, it does not need anisotropic materials for its implementation, in contrast to the perfect cloak.[2] The problem of the critical points can be circumvented by using advanced techniques as Non-Euclidean cloaking[99] or transmutation of singularities,[100] but at the expense of introducing some anisotropy, as we will see below. Despite the rapid development of new strategies for broadband cloaking, it seems that a final device is still out of reach.

Gravity analogues

The formal equivalence between Maxwell's equations in a curved geometry and in a medium sets the perfect scenario for constructing gravity analogues within the frame of transformation optics. Along this line, interesting theoretical proposals include analogues of orbital motion,[7] or black holes.[8,91]

A fiber-optical experimental verification of the event horizon realized in 2008 deserves special mention[6]. It is common practice to visualize a black hole as a river flowing towards a waterfall in which water has a variable speed v, steadily increasing as we get closer to the waterfall.[85] The river supports waves propagating with velocity c relative to the water. When these waves propagate upstream against the current, they undergo a dragging effect towards the waterfall because of the moving water. If v exceeds c, no water wave will be able to continue its way upstream, getting trapped in this water-analogue black hole. The point where v equals c is the corresponding event horizon. In a similar fashion, waves coming from the sea that approach the waterfall from below are not able to climb up against it, a physical phenomenon known as a white hole. That is to say, moving media create equivalent spacetime geometries that can resemble black or white holes. Following this idea, an analogue event horizon was generated by inserting ultrashort pulses in a microstructured optical fiber. Each pulse induces a change in the fiber index of refraction due to the non-linear *Kerr* ef-

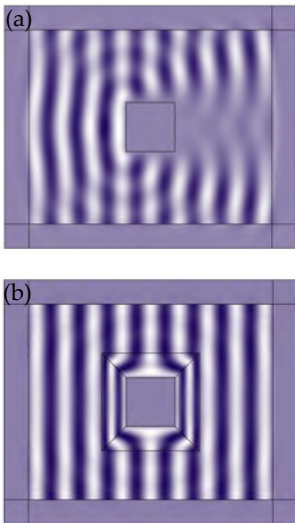[2] Unlike the perfect cloak, this device only works in the limit of geometrical optics.

Figure 3.5: Square cloak. (a) A plane wave impinges upon a metallic object, being diffracted by the latter in such a way that shadows and reflections appear, allowing us to detect the presence of the object. (b) If we surround the object with a square cloak, the electromagnetic flow is redirected around it avoiding "contact" with the object. After passing through the cloak, the wave recovers the shape it would have if the cloak plus object system were not there, which are effectively rendered invisible. The design of this particular cloak is described in[101]. We have simulated its performance with COMSOL Multiphysics.

fect. This change of index is carried with the pulse giving rise to a moving medium for light. As a consequence, each pulse creates a black-hole horizon at the front and a white-hole horizon at its rear end. Remarkably, the blue-shift of a continuous wave (chasing after the pulse with slightly higher speed) was observed in this experiment, as it should occur with light at a white-hole horizon. In addition to this classical effect, this kind of analogue model could probe quantum-physical aspects of the event horizon such as Hawking radiation, since the interaction between the moving medium and the wave is linear even at the quantum scale. This fact was theoretically shown in Ref. 6. Moreover, Belgiorno *et al.* claim to have observed Hawking radiation in a more recent experiment by using optical filaments (laser pulses in the form of needle-like beams) in bulk glass.[102] Notwithstanding, we must bear in mind that gravity analogues have limitations and that they only capture certain aspects of gravitational fields.[88,8]

Focusing and lensing devices
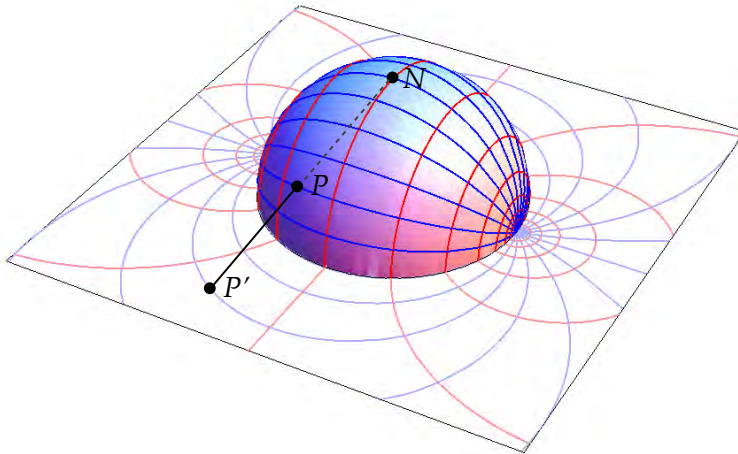
Figure 3.6: The stereographic projection, already known by Ptolemy, Hipparchus and probably the Egyptians, maps the surface of a sphere to the equatorial plane. Each point P in the sphere is mapped to a point P' in the plane, which corresponds to the intersection of the line passing through the north pole (N) and P, with the equatorial plane. The figure shows the projection of some lines in the sphere to the plane.

Maxwell's fisheye provides a simple and beautiful example of the implementation of a curved geometry in a flat space. It synthesizes the stereographic projection (see Figure 3.6) of the surface of a sphere (virtual space with a curved geometry) to

the plane (flat geometry in physical space) — hypersphere to hyperplane in general. Invented by Maxwell more than 150 years ago, Maxwell's fisheye (it reminded Maxwell of the eyes of a fish) is a spatially-varying positive refractive index distribution that focuses all light rays emitted from any point in an exact image point, therefore constituting a perfect lens for ray optics.[103] A century and a half later, it was suggested that Maxwell's fisheye could also image waves with perfect resolution, something that could pave the way for perfect imaging devices with positive index of refraction, which do not have the physical and implementation limitations of negative index lensing devices.[93,104,105,106,107] Much like the perfect lens based on negative refraction, this proposal did not come without controversy.[108]

Other devices

A myriad of interesting devices have arisen thanks to transformation optics. Special lenses,[109] beam shifters and splitters,[110] concentrators,[101] polarization rotators,[111] superscatterers[112] or illusion-optics devices,[113] are among them. Other important devices will be mentioned or studied in next sections. The interested reader can consult additional references from the Bibliography.[89,114,115,116]

3.3 Transmutation of singularities: optimizing the constitutive parameters (our contribution)

As we mentioned in the previous section, the main problem in some cloaking devices is the existence of singularities where the refractive index should be zero. There exist other optical devices in which the singularity comes in the form of an infinite value of the refractive index. This is the case of the invisible sphere or the Eaton lens. All of them have a common feature: the refractive index behaves like $n = r^p$ near the singularity, where p is a real constant. Transformation optics provides a solution to this situation consisting of stretching space around the singularity in order to increase or decrease the refractive index to a finite reasonable value, without affecting the part of the device that interacts with the exterior.[100] Note that in this case, transformation optics is used as a tool to modify existing devices in order to facilitate their practical realization without altering their functionality, instead of creating novel devices with new functionalities. The price to pay for removing the singularity is that the original isotropic device is transformed into an anisotropic one — a less harmful feature than the singularity in any case.

Although it is not possible to achieve a completely isotropic device by transforming another isotropic device via a radially symmetric mapping, we would like to find the optimal transformation that minimizes the anisotropy. For this purpose we focus our attention on the Eaton lens — the results can be extended to other devices straightforwardly —, which has a spherically symmetric index profile given by

$$n(r) = \begin{cases} \sqrt{\frac{2a}{r} - 1}, & r \le a \\ 1, & r > 0 \end{cases} \tag{3.4}$$

The transformation that we want to apply has the form

$$
\begin{aligned}
R &= R(r) \\
\theta &= \theta' \\
\phi &= \phi'
\end{aligned}
\tag{3.5}
$$

By using Eq. (3.2) and expressing the result in the local orthonormal system, it can be shown that the required constitutive parameters of the transformed device are[3]
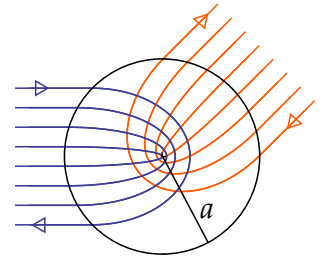
Figure 3.7: The Eaton lens is a perfect retroreflector that reflects back incident light rays coming from any direction.

[3] Note that Eq. (3.2) needs to be modified to account for the fact that virtual space is not empty, but filled with an isotropic medium (the orginal device with the singularity, *e.g*, the Eaton lens) with permittivity ε' and permeability μ'. It is easy to see that in this case

$$\varepsilon^{ij} = \varepsilon' \frac{\sqrt{\gamma'}}{\sqrt{\gamma}} \gamma'^{ij} \quad \mu^{ij} = \mu' \frac{\sqrt{\gamma'}}{\sqrt{\gamma}} \gamma'^{ij}$$

$$\left(\varepsilon_j^i\right) = \left(\mu_j^i\right) = n(r) \begin{pmatrix} \frac{r^2}{R^2}\frac{dR}{dr} & 0 & 0 \\ 0 & \frac{dR}{dr}^{-1} & 0 \\ 0 & 0 & \frac{dR}{dr}^{-1} \end{pmatrix}, \tag{3.6}$$

where it is assumed that $\varepsilon' = \mu' = n(r)$. The transformation $R(r)$ must fulfill the conditions

$$R(r \to 0) \to r^{p+1}, \tag{3.7}$$

$$R(a) = a. \tag{3.8}$$

The first condition ensures that the singularity is removed. The second implies that the transformation is continuous at the device exterior boundary (which corresponds to $r = a$) so that its functionality (as viewed by an external observer) remains unchanged. For the Eaton lens, $p = -1/2$. The following transformation, which satisfies the previous conditions, was initially proposed to solve the problem [100]

$$R = \frac{2}{n_0}\left[\arcsin\left(\sqrt{\frac{r}{2a}}\right) + \sqrt{\frac{r}{2a}\left(1 - \frac{r}{2a}\right)}\right], \quad n_0 = \frac{\pi + 2}{2}. \tag{3.9}$$

Using Eq. (3.9) in Eq. (3.6) yields

$$\left(\varepsilon_j^i\right) = \left(\mu_j^i\right) = \begin{pmatrix} \frac{1}{n_0}\left(\frac{n(r)r}{R}\right)^2 & 0 & 0 \\ 0 & n_0 & 0 \\ 0 & 0 & n_0 \end{pmatrix}, \tag{3.10}$$

which obviously represents an anisotropic medium.[4] Let us see if we can find a better mapping $R(r)$ in the sense of minimizing the anisotropy — defined as $|\varepsilon_r^r - \varepsilon_\theta^\theta| = |\varepsilon_r^r - \varepsilon_\phi^\phi|$. Solving this problem analytically is quite involved, so we address it numerically. To this end, we need to set optimization variables.

[4] This result was subsequently used to implement an Eaton lens, which constitutes an omni-directional retroreflector. [117]

Figure 3.8: Transmutation of singularities. Optimization scheme for the minimization of the anisotropy.
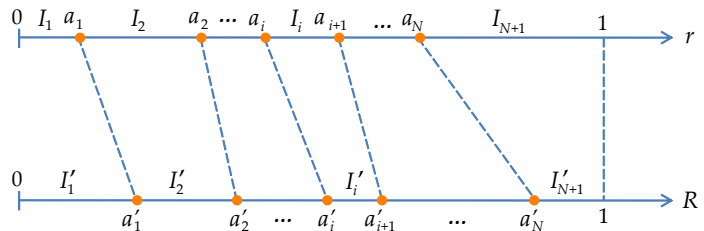
For that purpose, we divide the interval $[0,1]$ in r and R into $N + 1$ smaller intervals (note that we have taken $a = 1$ for simplicity), as in Figure 3.8. Then, we map each interval I_i to the interval I_i' by using a certain function $R_i(r)$. We cannot use a linear transformation in the first interval, since we would not remove the singularity in that case. However, we need to choose a certain function because the optimization algorithm needs to control it through optimization variables. The function must fulfill the condition given by Eq. (3.7). Thus, in this interval we use the function $R_1(r) = C\sqrt{r}$, where we have introduced the constant C as an optimization variable to allow for a higher degree of freedom[5]. We map any other interval I_i to interval I_i' using a linear transformation

$$R_i = A_i + B_i r, \tag{3.11}$$

with

$$\begin{aligned} a_i' = R_i(a_i) = A_i + B_i a_i \\ a_{i+1}' = R_i(a_{i+1}) = A_i + B_i a_{i+1} \end{aligned} \Rightarrow \begin{aligned} B_i = (a_{i+1}' - a_i')/(a_{i+1} - a_i) \\ A_i = a_{i+1}' - B_i - a_{i+1} \end{aligned} \tag{3.12}$$

Now, regarding the nodes a_i and a_i' as variables that can be optimized, we can try to find the optimal curve $R(r)$. Note that we can obtain any arbitrary function $R(r)$ for a sufficiently high value of N. The error function to be minimized will be:

$$\begin{aligned} F(a_i, a_i') &= \max_i \max_{R \in I_i'} \left(\varepsilon_r^r(R) - \varepsilon_\theta^\theta(R) \right)^2 \\ &= \max_i \max_{R \in I_i'} n^2(r) \left(\frac{r^2}{R^2} \frac{dR}{dr} - \frac{dr}{dR} \right)^2. \end{aligned} \tag{3.13}$$

This way, we minimize the maximum anisotropy (*minimax* optimization). To perform this optimization we write a suitable code in MATLAB. It is worth mentioning that we are taking into account the specific refractive index profile in virtual space and the solution found will be valid only for that specific problem. We tested the code with different number of nodes N. The initial set of nodes a_i and a_i' is arbitrarily chosen. The results are depicted in Figure 3.9.

Although the optimization algorithm is not perfect — it only finds local minima — and the error function could be improved, the results indicate that the optimal curve lies slightly below
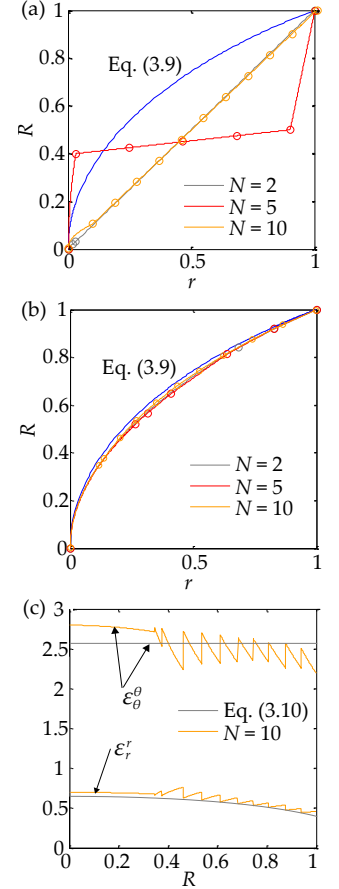
Figure 3.9: Optimized curves and constitutive parameters. (a) Initial set of nodes and corresponding curves $R(r)$ for different values of N. The nodes are represented by circles. The curve corresponding to Eq. (3.9) is also shown. (b) Same as in (a) but after optimization. (c) Constitutive parameters corresponding to the case $N = 10$ and to Eq. (3.10).
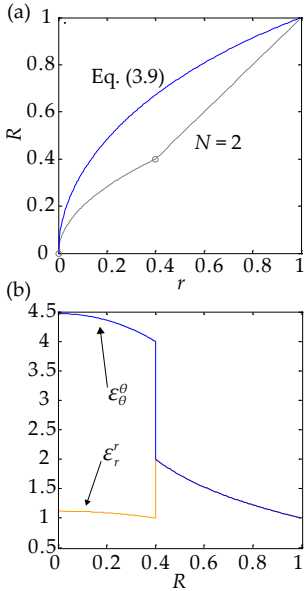
Figure 3.10: Special case with constitutive parameters above unity. (a) Function $R(r)$. (b) Constitutive parameters.

Eq. (3.9). Even with just two points ($N = 2$) we almost obtain the optimal result. Unfortunately, the reduction of the anisotropy provided by the optimal curve is very low as compared to the solution given by Eq. (3.10). Specifically, for the curve given by Eq. (3.9), $\max |\varepsilon_r^r - \varepsilon_\theta^\theta| = 2.182$ and our best result is $\max |\varepsilon_r^r - \varepsilon_\theta^\theta| = 2.08$. Luckily, we found something positive during the optimization process. An interesting set of constitutive parameters is obtained for $N = 1$ and $a_1 = a_1'$. Let us take for instance $a_1 = a_1' = 0.4$. The result is depicted in Figure 3.10.

As we can see, in the interval $a_1 < R < 1$ we have the identity transformation and, therefore, the original isotropic Eaton lens index profile. For this reason, this technique has been called *partial transmutation of singularities*. In addition, in contrast to the results achieved with Eq. (3.9), the parameters corresponding to the interval $R < a_1$ are above 1 (the minimum value of the constitutive parameters can be adjusted by moving a_1). Values above 1 mean that no resonant elements are needed for their implementation, so that the device can be broadband in principle. This could turn into reality interesting devices that otherwise would be difficult to realize or, at least, would be inherently narrow-band. The idea of partial transmutation of singularities was independently conceived and developed by J. Perczel soon after. The main features and advantages of the partial transmutation of singularities are also described in PAPER7. One of the key applications is the realization of invisibility cloaks without superluminal propagation.[118]

3.4 Reflectionless light squeezers and expanders and their applications (our contribution)

A considerable part of our research in transformation optics has been focused on the study of the properties of light squeezers and expanders based on transformation optics. Although this kind of elements arise from one of the simplest transformations (a continuous compression or expansion of space), they may lead to extremely useful applications, ranging from beam collimation to nanolithography, optical data storage, imaging quality enhancing and efficient coupling to nanoscale structures.[119,120] Squeezers and expanders correspond to transformations that are inherently discontinuous at the input or the output of the device. This kind of mappings belong to what has been termed finite embedded transformation.[110], which enables us to transfer light alterations, such as bends or shifts, from the transformed media to another one,[110] so it appears that this technique is very adequate for building squeezing devices. A simple two-dimensional (2D) version of a compressing device embedded in free space was studied in Ref. 121, showing that unavoidable reflections appear in that case. Reflections imply power loss, which invalidates the utility of squeezers in many situations. The need for antireflective coatings was also observed in Ref. 121, although it was not clear at all how to design an antireflective coating for such a complex material and no hint was given in that study. Moreover, the conclusions drawn from the 2D case cannot be generalized to the three-dimensional (3D) one, as there can be fundamental differences between them. In addition, the heuristic condition for no reflections given in Ref. 121 only allows us to know whether the device is reflectionless for all angles or not. However, the reflected power depends on the polarization and on the angle, and could be negligible for certain spatial directions. Finally, in some situations it would be desirable that the output medium was different from the input one (in fact, we will take advantage of the squeezer properties in this situation to make a reflectionless device). Therefore, the possibility of achieving reflectionless squeezers was still open and a general study with the aim of obtaining this feature, indispensable for most applications, was lacking. We performed such a study in PAPER8 and describe it in detail in the follow-

ing subsections. The striking possibility of implementing devices that couple free-space light to surface plasmon polaritons along non-patterned metallic surfaces with angular bandwidths considerably higher than those of conventional couplers is described in PAPER9. The practical implementation of squeezing and expanding devices is addressed in next section.

Theory

In an isotropic homogeneous background, only rotations and displacements of the outer boundaries achieve all-angle reflectionless transformation media.[122] Thus, to build an all-angle reflectionless squeezer, which has a compressed boundary, it is necessary to consider a more general scenario. Specifically, we will allow the medium that will be transformed into the squeezer to be different from the output medium in original space. This step is the key for some of the results obtained below. It is also important to consider a full problem with the possibility of a 3D transformation as mentioned above. Finally, our aim is to obtain an analytical expression for the total reflection coefficient of the squeezer, so that we can evaluate the reflected power and see if there is any preferred spatial direction for which no reflections occur. The problem under consideration is sketched in Figure 3.11.

Figure 3.11: Sketch of the problem. Cartesian coordinate mesh in the original media is "seen" distorted by the fields in the transformed media
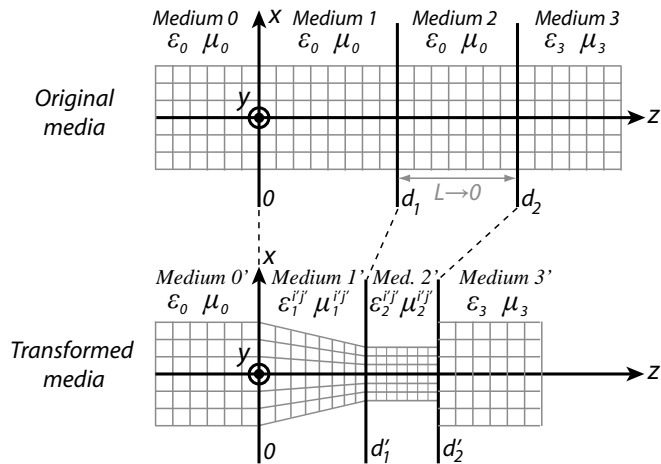
We start from Euclidean flat space with Cartesian coordinates denoted by x^i ($i = 1, 2, 3$, $x^1 = x$, $x^2 = y$ and $x^3 = z$) and map it to another space with coordinates $x^{i'}$. Both coordinate sets are related by the functions $x^{i'} = f_i(x^j)$. We assume that in original space all media are isotropic. A pair of constitutive parameters $\varepsilon = \varepsilon_0 \varepsilon_r$ and $\mu = \mu_0 \mu_r$ in this space, becomes $\varepsilon^{i'j'} = \left(\epsilon^{klm} \Lambda_k^1 \Lambda_l^2 \Lambda_m^3 \right)^{-1} g^{i'j'} \varepsilon$ and $\mu^{i'j'} = \left(\epsilon^{klm} \Lambda_k^1 \Lambda_l^2 \Lambda_m^3 \right)^{-1} g^{i'j'} \mu$ in transformed space, where ϵ and $\Lambda_i^{i'}$ are the Levi-Civita and Jacobian tensors.[91] In the materials interpretation, these are the media to be placed in physical space, represented by the original coordinate system, to modify the fields according to the transformations given by f_i. We have divided the problem into four slab-shaped regions (see Figure 3.11). Medium 0 is air, from which light impinges onto medium 1. Mediums 1 and 2 are also air. Medium 3 (output medium), is isotropic and is characterized by ε_3 and μ_3. These media are transformed into those denoted by primed numbers according to the piecewise functions given by

$$
f_i := \begin{cases} x^i, & -\infty < z \le 0 \\ \left\{ h_i \,|\, h_{(i),(i)}(z = 0) = 1, h_{(i),(i)}(z = d_1) = F_i \right\} & 0 < z \le d_1 \\ x^k D_k^i & d_1 < z \le d_2 \\ x^i - (d_2 - d_2')\delta_1^i & d_2 < z < \infty \end{cases}
\tag{3.14}
$$

where $d_2' = d_2 / F_3$ and we have defined $D_k^i = diag\,(1/F_1, 1/F_2, 1/F_3)$. No summation is to be performed over repeated indices in parentheses. Note the discontinuity in the transformation at $z = d_2$, which is in general the reason for reflections in embedded compressors. The transformation performed on media 0 and 3 does not change their parameters. Medium 1' (transformed medium 1) is the squeezer/expander. A continuous compression is made in it, going from no compression at $z = 0$ to a compression F_i in coordinate x^i at $z = d_1$ ($0 < F_i < 1$ means expansion). The parameters of medium 1', $\varepsilon_1^{i'j'}$ and $\mu_1^{i'j'}$, are inhomogeneous and generally quite complicated at $z = d_1$, making it very difficult to calculate the reflection between this medium and the output one. Our approach to calculate the squeezer's reflection is to introduce an auxiliary layer (medium 2 and its transformed counterpart medium 2'), in which the squeezer's

compression at $z = d_1$ is kept constant. Thus, the relative constitutive parameters of medium 2' are:

$$\xi^{i'j'} := \varepsilon_{2r}^{i'j'} = \mu_{2r}^{i'j'} = F_1 F_2 F_3 diag\left(1/F_1^2, 1/F_2^2, 1/F_3^2\right) \quad (3.15)$$

Restricting ourselves to continuous transformations at the boundaries between media 0-1 and 1-2 ensures that no reflections will take place at these interfaces. The fact that $\xi^{i'j'}$ is homogeneous and has its principal components along the Cartesian axes greatly simplifies the problem of calculating the reflection coefficient R between media 2' and 3'. This can be done by matching the tangential components of the eigenmodes of an anisotropic homogeneous slab (medium 2') and the isotropic outer medium (medium 3') at their interface.[123] R does not depend on the length L of medium 2. This enables us to make L tend to zero, so in practice this layer will not exist. We now analyze the case corresponding to $k_y = 0$ (the derived formula can be generalized with some extra work), for which it can be shown that (see derivation below)

$$R = \alpha \frac{\rho_3 \sqrt{\omega^2 \varepsilon_0 \mu_0 F_1^2 - k_x^2} - F_2 \sqrt{\omega^2 \varepsilon_3 \mu_3 - k_x^2}}{\rho_3 \sqrt{\omega^2 \varepsilon_0 \mu_0 F_1^2 - k_x^2} + F_2 \sqrt{\omega^2 \varepsilon_3 \mu_3 - k_x^2}} \quad (3.16)$$

where $\rho_3 = \varepsilon_{r3}$, $\alpha = -1$ for TM polarization (**H** field along the y axis) and $\rho_3 = \mu_{r3}$, $\alpha = 1$ for TE polarization (**E** field along the y axis). The cross-reflection coefficients between both polarizations are zero. Since reflection is only possible at this boundary, Eq. (3.16) expresses the total reflection of the squeezer/expander. First, we observe that R is independent of z compressions. Moreover, we can identify three very interesting cases in which reflection vanishes

1. $\mu_{r3} = F_2 = 1$ and $\varepsilon_{r3} = F_1^2$ for TE incidence.

2. $\mu_{r3} = 1$ and $\varepsilon_{r3} = F_2 = F_1^2$ for TM incidence.

3. $\varepsilon_{r3} = \mu_{r3} = 1$ and $F_1 = F_2$ for normal incidence ($k_x = 0$) and arbitrary polarization.

We have focused on non-magnetic output media, which are the most common ones. The first two cases tell us that $R = 0$ if the outer medium is a certain dielectric. Note that allowing media

2 and 3 to be different has been crucial to find these two conditions. Remarkably, the third case indicates that, for normal incidence (which is the case in many applications), $R = 0$ if we perform a uniform transversal compression from air to air. It has to be stressed that this condition cannot be found by studying a 2D problem. Going a step further, we would like to transfer squeezed light to any dielectric medium characterized by ε_d, regardless of the compression. The conditions for $R = 0$ give us a key knowledge to achieve this. Since there are no reflections if the output dielectric permittivity is ε_3, we only need to match this dielectric to the desired one, with constant ε_d. Antireflective coatings engineering between two isotropic dielectrics is a much explored field that offers many simple and flexible options.[124] Therefore, a straight solution is to put the proper antireflective coating between the squeezer and the medium characterized by ε_d. This way the squeezer will be matched to ε_d instead of ε_3 (no medium with ε_3 is then needed, as it happened with the auxiliary layer). Usually, antireflective coatings consist of one or few dielectric layers, depending on bandwidth and angular requirements. Placing a dielectric layer at the device's output is easier than implementing the squeezer and it does not pose a technological drawback. To verify our theoretical results, numerical simulations have been performed using COMSOL Multiphysics. As an example, we designed a 2D squeezer for TE polarization with $h_1 = x/(1 + Cz)$, $h_2 = y$, $h_3 = z$, $C = (F_1 - 1)/d_1$ and $F_1 = 4$. Figure 2 shows its performance when the incident wave is a Gaussian beam.

Two cases are considered. In the first one, the output medium is $\varepsilon_{rd} = \varepsilon_{r3} = F_1^2$ so that no antireflective coating is needed. In the second case, $\varepsilon_{rd} = 1$ and we use a $\lambda/4$ dielectric coating with constant ε_{rc}. It is known that if $\varepsilon_{rc}^2 = \varepsilon_{r3}\varepsilon_{rd}$, reflections are suppressed. In both cases, the calculated relative transmitted power $P_t = P_{out}/P_{in}$ is 100% (P_{in} and P_{out} are the squeezer input and output power). Without the coating, $P_t = 63\%$. We can verify this result with Eq. (3.16), as $P_t = 1 - |R|^2$. Since incidence is almost normal, we can put $k_x = 0$. Substituting the problem data in Eq.(3.16) we obtain $P_t = 64\%$, in very good agreement with numerical results. Note that the different **E** field intensities in the input and output media are consistent with the conservation of total power flow. It is also worth mentioning that the
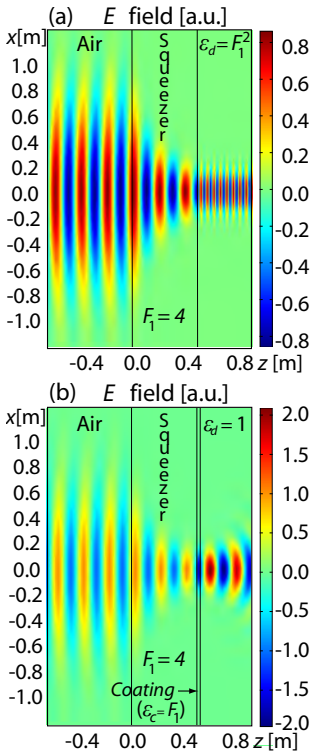
Figure 3.12: Electric field distribution in the squeezer. The working wavelength is $\lambda = 0.2$ m. The relative permittivity of medium 3 is (a) $\varepsilon_{rd} = F_1^2$. (b) $\varepsilon_{rd} = 1$.

squeezer provides a compressed version of the fields inside it. This compression is transferred to the outside world near the squeezer. However, once the electromagnetic wave has exited the squeezer, it is subject to the diffraction laws of the output medium. Thus, the Gaussian beam exiting the squeezer will diverge as it propagates. This is mainly observed in Figure 2(b), as this divergence is faster in air than in the medium with $n = 4$.

Applications

Applications of the proposed reflectionless device are straightforward. Here, two additional potential applications are proposed. The first one is a perfect squeezer-based spot size converter for an efficient coupling between an optical fibre and a high-index nanophotonic waveguide or nanowire, which is one of the most challenging tasks in the field of silicon photonics, due to the large mismatch in mode size of nanowires (sub-wavelength transversal dimensions) and standard single mode fibres (SMF, 10 μm mode diameter). Many solutions have been proposed, following one of these approaches: lateral (in plane) or vertical (out of plane) coupling. The latter requires out of plane diffraction, usually via grating couplers, whose achievable efficiency with conventional designs is lower than 40%.[125] To reach higher efficiencies, highly sophisticated designs are needed, extremely increasing fabrication difficulty.[126] Lateral coupling implies 2D SSC via waveguide inverse tapering down to tens of nanometers wide,[120] so matching the high SMF mode size is very challenging with a single inverted tapering structure. Most actual realizable single stage structures are limited in mode size to approximately 3-4 μm. Efficient coupling to such mode diameters can be achieved by means of lensed or high-numerical-aperture fibres with 3-4 μm mode diameters. Usually, in these structures the required inverted taper is longer than 200 μm and maximum coupling efficiency is lower than 80%.[127] We aim to use our squeezer as an efficient SSC with a dramatically reduced length while achieving 100% coupling efficiency. Thus, the squeezer must compress incoming light fitting its size to that of the waveguide and then deliver the compressed beam to the waveguide without reflections, *i.e.*, match air to the waveguide high-index core. Then, light is kept con-

fined in the waveguide by total internal reflection (TIR) (see Figure 3.13). We will assume the telecom wavelength $\lambda = 1.5\mu m$, and a waveguide with sub-wavelength width $w = 1\mu m$ and refractive index $n = 4$, as in the example of Figure 2 (the problem would be very similar if we used silicon, since $n_{Si} = 3.45$ in this band).
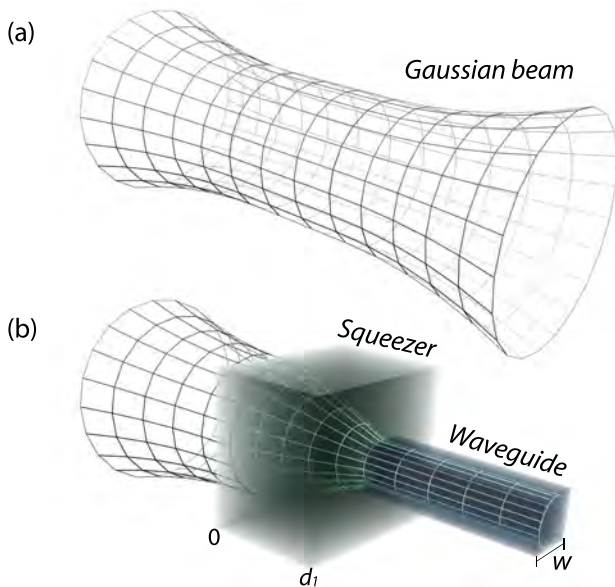
Figure 3.13: (a) Gaussian beam propagating in free space. (b) The squeezer couples the beam to a nanophotonic dielectric waveguide.

We limit our study to a 2D case due to the computational complexity of the 3D problem. Given the size of the input beam, a compression $F_1 = 4$ is enough, which satisfies condition 1 for no reflections. A seamless coupling can be observed in Figure 3.14. Numerical calculations reveal that $P_t = 100\%$ again, where P_{out} has been evaluated at the right waveguide end. Without the squeezer, $P_t < 40\%$ and decreases with z due to an inefficient mode matching. To extend the application to larger compression factors, antireflective coatings are necessary. In a 3D problem, compression in both transversal directions is demanded. Since in this application we have normal incidence, a squeezer fulfilling condition 3 with the proper antireflective coating can be employed. As for its size, the squeezer can be as short as desired. Nonetheless, the necessary constitutive pa-

rameters become extreme as we reduce d_1. A surprisingly small length below 10 μm, far below the current state of the art, is enough to achieve a set of parameters with very moderate values for the 2D and 3D cases. Although fabrication of the 3D squeezer would be challenging, it is worth pointing out that quasi-conformal mappings would provide a practically realizable non-magnetic isotropic implementation for the 2D squeezer, as we will see below. Regardless of its application as SSC, our squeezer-TIR waveguide device presents the important advantage of using an isotropic homogeneous dielectric as the guiding element, as opposed to previously proposed squeezers based on transformation optics,[128] where complex materials are needed.

Figure 3.14: (a) Simulation of a 2D Gaussian beam propagating in free space. (b) The beam in (a) is squeezed and perfectly coupled to the nanophotonic waveguide.
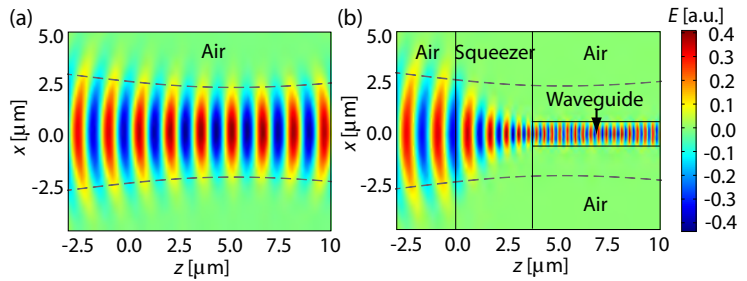
The second application that we propose is a flat hyperlens that uses our reflectionless device as a wave expander. It is known that subwavelength spatial features of light sources are lost in the far field, since they are carried by evanescent waves that decay exponentially with distance. A hyperlens transforms evanescent components into propagating ones by magnifying the near field pattern, which can then be treated with conventional optics. Original hyperlenses had cylindrical geometry and suffered from reflections, two undesired features.[114] A flat hyperlens arising from the truncation of the original design has been reported, although the truncation gave rise to a variable gain, stronger at the hyperlens centre.[129] Transformation optics has led to alternative designs that improved the impedance matching and made one of the two lens surfaces flat.[114,130] A hyperlens with both flat surfaces was also proposed.[131] However, it is not reflectionless and, as no expansion in the z-direction

is made, its width must be extremely small. The above theoretical results, enables us to design an expander that implements a completely flat reflectionless hyperlens. Following a similar approach to that of Ref. 130, we transform a little slab of length d_1 into a larger slab of length d_1' (this can be done without affecting the reflection properties of the device, since the reflection coefficient is independent of compressions/expansions in the z-direction as was shown above), while expanding the fields in the x-direction at the same time. This transformation can be described by $h_1 = x/(1 + C_1 z)$, $h_2 = y$, and $h_3 = x/(1 + C_2 z)$, with $C_1 = (F_1 - 1)/d_1$, $C_2 = (F_3^{1/2} - 1)/d_1$ and $F_1, F_3 < 1$. Since light goes from air to air, antireflective coatings are needed. An interesting particular case is that in which the sources are embedded in a dielectric medium with constant $\varepsilon_{r3} = n_3^2$. In this case we can use a squeezer from air to that dielectric, described by the previous functions with the same value of F_3 and satisfying $F_1 = n_3$ (no coating is needed in this case). Since light now travels from right to left (according to Figure 3.11), the squeezer acts as an expander. Propagating components inside the dielectric also become propagating in air, improving the resolution by F_1, in a similar way to solid immersion lenses, with the advantage of being flat and reflectionless. Note that this lens can perform in far field. In Figure 3.15 we provide a numerical example with $F_1 = 2$, $F_3 = 1/100$ and $d_1 = \lambda/20$, where two test point sources separated by $\lambda/4$ are placed near the lens left surface (for better clarity, in Figure 3.15 the squeezing device is flipped from left to right as compared to the previous figures).

The magnitude of the resulting power flow is shown in Figure 3.15. Cuts at $z = 0$ (the lens output) and at a distance $\lambda/20$ away from the sources without the lens are also depicted. Clearly, the device provides a magnified image of the fields where the images of the two sources are separated by $\lambda/2$. Finally, we apply our theoretical results to the coupling between two metallic waveguides of different transverse size. Several devices based on transformation optics have been proposed to solve this problem.[132,133] However, as in the other cases, the problem of reflections has not been addressed. In these works, some simple compressing or expanding spatial transformation is applied to adapt the dimensions of one waveguide to the other one. This way, and according to our previous theoretical

results, a mismatch between the modes supported by the coupler and the outer medium (in this case, the output waveguide) is introduced.
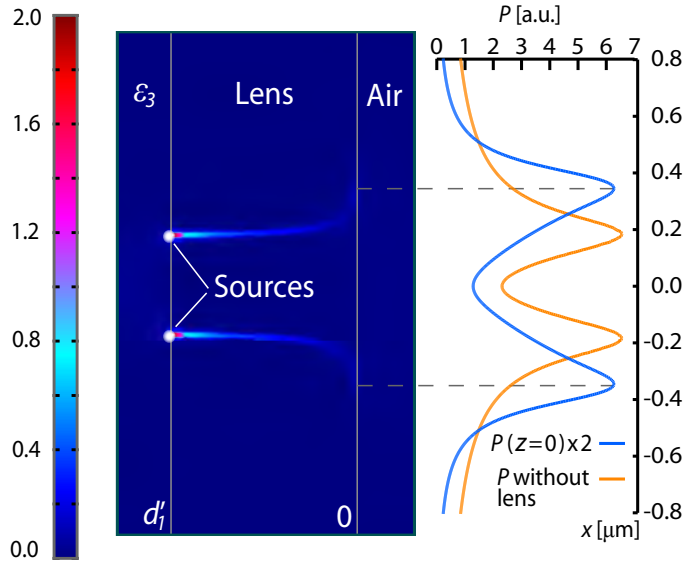
As an example, let us assume that we desire to couple a waveguide $W1$ of transverse size a, to another waveguide $W2$ of transverse size $a/2$, where we only excite the first TE mode at the left end of waveguide $W1$. In Figure 3.16, we show the norm of the electric field for different solutions to this problem. In Figure 3.16(a), no coupler is used and we just linearly change the metallic boundary of the waveguide. The strong modulation appearing in waveguide $W1$ and the transition waveguide indicates that high reflections are taking place at the boundary between the transition waveguide and waveguide $W2$.

In Figure 3.16(b), we use a coupler that implements a linear spatial transformation from a transverse size of a, to a transverse size of $a/2$ ($F_1 = 2$), similar to the one employed in the previous examples and to those in [19, 20]. Again, strong reflections are observed. Now we apply our theory to this example. To a first approximation, we assume that the effective indices in

waveguides $W1$ and $W2$ are those of the filling medium. There-fore, in Figure 3.16(b), $\varepsilon_{r3} = n_3^2 = 1$.

Figure 3.16: Several solutions for coupling two metallic waveguides of different trans-verse size. In this example, $a = 0.4$ m and $d = 0.5$ m. The free space wavelength is $\lambda = 0.37$ m, below cut-off in all waveguides. $|\mathbf{E}|$ distribution (a) without coupler, (b) with coupler and $n_3 = 1$, and (c) with coupler and $n_3 = 2$. (d) S_{11} parameter as a function of n_3 when the coupler is used.
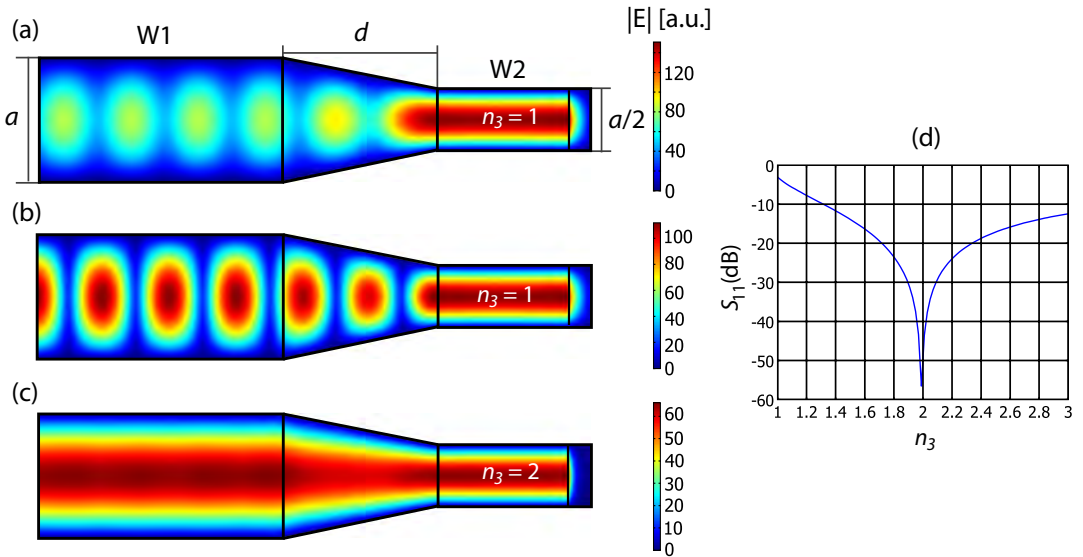
Obviously, reflections appear because we are not fulfilling condition 1. This can be easily solved by filling waveguide $W2$ with a material $n_3 = 2$ [Figure 3.16(c)]. In this case, no modu-lation of the electric field is observed, showing that reflections have been suppressed. Alternatively, if we want waveguide $W2$ to be empty, we can design and use a dielectric antireflective coating following the procedure described above. This way, a perfect coupling between both waveguides is achieved. In Fig-ure 3.16(d), we depict the scattering parameter S_{11} as a function of the refractive index of the filling medium of waveguide $W2$, for the case where the coupler is used [as in Figs. 3.16(b-c)]. A pronounced minimum is clearly seen very close to $n_3 = 2$, vali-dating our choice of effective indices.

Derivation of the reflection and transmission coefficients

We will work in Cartesian coordinates (we do not care about in-dices being up or down) with symbolic notation. In this frame, the permittivity and permeability tensors are

$$(\varepsilon) = \begin{pmatrix} \varepsilon_{11} & \varepsilon_{12} & \varepsilon_{13} \\ \varepsilon_{21} & \varepsilon_{22} & \varepsilon_{23} \\ \varepsilon_{31} & \varepsilon_{32} & \varepsilon_{33} \end{pmatrix}, \qquad (\mu) = \begin{pmatrix} \mu_{11} & \mu_{12} & \mu_{13} \\ \mu_{21} & \mu_{22} & \mu_{23} \\ \mu_{31} & \mu_{32} & \mu_{33} \end{pmatrix} \qquad (3.17)$$

We also define the tensors (analogous expressions are defined for μ_{tt}, μ_{tz}, and μ_{zt})

$$(\varepsilon_{tt}) = \begin{pmatrix} \varepsilon_{11} & \varepsilon_{12} & 0 \\ \varepsilon_{21} & \varepsilon_{22} & 0 \\ 0 & 0 & 0 \end{pmatrix}, \quad (\varepsilon_{tz}) = \begin{pmatrix} 0 & 0 & \varepsilon_{13} \\ 0 & 0 & \varepsilon_{23} \\ 0 & 0 & 0 \end{pmatrix}, \quad (\varepsilon_{zt}) = \begin{pmatrix} 0 & 0 & 0 \\ 0 & 0 & 0 \\ \varepsilon_{31} & \varepsilon_{32} & 0 \end{pmatrix} \qquad (3.18)$$

and separate Maxwell's equations in their transverse and longitudinal components

$$i\mathbf{k}_t \times E_z \hat{z} + \hat{z} \times \frac{\partial \mathbf{E}_t}{\partial z} = i\omega \mu_{tt} \cdot \mathbf{H}_t + i\omega \mu_{tz} \cdot H_z \hat{z} \qquad (3.19)$$

$$i\mathbf{k}_t \times \mathbf{E}_t = i\omega \mu_{zt} \cdot \mathbf{H}_t + i\omega \mu_{33} H_z \hat{z} \qquad (3.20)$$

$$i\mathbf{k}_t \times H_z \hat{z} + \hat{z} \times \frac{\partial \mathbf{H}_t}{\partial z} = -i\omega \varepsilon_{tt} \cdot \mathbf{E}_t - i\omega \varepsilon_{tz} \cdot E_z \hat{z} \qquad (3.21)$$

$$i\mathbf{k}_t \times \mathbf{H}_t = -i\omega \varepsilon_{zt} \cdot \mathbf{E}_t - i\omega \varepsilon_{33} E_z \hat{z}, \qquad (3.22)$$

where $\mathbf{E}_t = E_x \hat{x} + E_y \hat{y}$, $\mathbf{H}_t = H_x \hat{x} + H_y \hat{y}$, $\mathbf{k}_t = k_x \hat{x} + k_y \hat{y}$. From Eq. (3.20) and Eq. (3.22), the longitudinal components of the fields can be expressed as a function of the transverse ones

$$H_z \hat{z} = \frac{1}{\omega \mu_{33}} \mathbf{k}_t \times \mathbf{E}_t - \frac{1}{\mu_{33}} \mu_{zt} \cdot \mathbf{H}_t \qquad (3.23)$$

$$E_z \hat{z} = -\frac{1}{\omega \varepsilon_{33}} \mathbf{k}_t \times \mathbf{H}_t - \frac{1}{\varepsilon_{33}} \varepsilon_{zt} \cdot \mathbf{E}_t \qquad (3.24)$$

Upon substitution of Eq. (3.23) and Eq. (3.24) in Eq. (3.19) and Eq. (3.21), we arrive to

$$\frac{\partial \mathbf{E}_t}{\partial z} = \left(-\frac{i}{\mu_{33}} \hat{z} \times \mathbf{I} \cdot \mu_{tz} \cdot \mathbf{k}_t \times \mathbf{I} - \frac{i}{\varepsilon_{33}} \hat{z} \times \mathbf{I} \cdot \mathbf{k}_t \times \mathbf{I} \cdot \varepsilon_{zt} \right) \cdot \mathbf{E}_t$$
$$+ \left(-i\omega \hat{z} \times \mathbf{I} \cdot \mu_{tt} + \frac{i\omega}{\mu_{33}} \hat{z} \times \mathbf{I} \cdot \mu_{tz} \cdot \mu_{zt} - \frac{i}{\omega \varepsilon_{33}} \hat{z} \times \mathbf{I} \cdot \mathbf{k}_t \times \mathbf{I} \cdot k_t \times \mathbf{I} \right) \cdot \mathbf{H}_t \qquad (3.25)$$

$$\frac{\partial \mathbf{H}_t}{\partial z} = \left(i\omega \hat{z} \times \mathbf{I} \cdot \varepsilon_{tt} - \frac{i\omega}{\varepsilon_{33}} \hat{z} \times \mathbf{I} \cdot \varepsilon_{tz} \cdot \varepsilon_{zt} + \frac{i}{\omega \mu_{33}} \hat{z} \times \mathbf{I} \cdot \mathbf{k}_t \times \mathbf{I} \cdot k_t \times \mathbf{I} \right) \cdot \mathbf{E}_t$$
$$+ \left(-\frac{i}{\varepsilon_{33}} \hat{z} \times \mathbf{I} \cdot \varepsilon_{tz} \cdot \mathbf{k}_t \times \mathbf{I} - \frac{i}{\mu_{33}} \hat{z} \times \mathbf{I} \cdot \mathbf{k}_t \times \mathbf{I} \cdot \mu_{zt} \right) \cdot \mathbf{H}_t \qquad (3.26)$$

Where $\mathbf{I} = \hat{x}\hat{x} + \hat{y}\hat{y} + \hat{z}\hat{z}$. As stated above, we will limit our-
selves to $k_y = 0$. In addition, the problem is simplified due to
the fact that both the auxiliary layer and the outer medium are
characterized by diagonal constitutive parameters. Given these
simplifications and considering that $\partial/\partial z = ik_z$, Eqs. (3.25)-
(3.26) reduce to:

$$ik_z \begin{pmatrix} \mathbf{E}_t \\ \mathbf{H}_t \end{pmatrix} = \mathbf{A} \cdot \begin{pmatrix} \mathbf{E}_t \\ \mathbf{H}_t \end{pmatrix} \tag{3.27}$$

$$\mathbf{A} = \begin{pmatrix} 0 & 0 & 0 & -\frac{ik_x^2}{\varepsilon_{33}\omega} + i\omega\mu_{22} \\ 0 & 0 & -i\omega\mu_{11} & 0 \\ 0 & \frac{ik_x^2}{\mu_{33}\omega} - i\omega\varepsilon_{22} & 0 & 0 \\ i\omega\varepsilon_{11} & 0 & 0 & 0 \end{pmatrix} \tag{3.28}$$

This is an eigenvalue problem with four solutions. From the
eigenvalues ik_z we find the four possible values of k_z (two for TE
polarization and two for TM polarization), together with their
corresponding eigenvectors (polarization states)

$$TE: \quad k_z^{1,2} = \pm\sqrt{\frac{\mu_{11}}{\mu_{33}}\left(\omega^2\varepsilon_{22}\mu_{33} - k_x^2\right)}, \quad \mathbf{E}_t = E\hat{y}, \quad \mathbf{H}_t = E\frac{k_z^{1,2}}{\omega\mu_{11}}\hat{x} \tag{3.29}$$

$$TM: \quad k_z^{3,4} = \pm\sqrt{\frac{\varepsilon_{11}}{\varepsilon_{33}}\left(\omega^2\mu_{22}\varepsilon_{33} - k_x^2\right)}, \quad \mathbf{E}_t = E\hat{x}, \quad \mathbf{H}_t = -E\frac{\omega\varepsilon_{11}}{k_z^{3,4}}\hat{y} \tag{3.30}$$

Now we particularize Eq. (3.29) and Eq. (3.30) for the parame-
ters of the auxiliary layer and the outer medium. The parame-
ters of the former correspond to a transformation medium asso-
ciated with the transformation $x^{i'} = x^{(i)}/F_{(i)}$, which leads to:

$$\begin{aligned} \varepsilon_2^{ij} &= \varepsilon_0\xi^{ij} \\ \mu_2^{ij} &= \mu_0\xi^{ij} \end{aligned} \tag{3.31}$$

$$(\xi^{ij}) = F_1F_2F_3 \begin{pmatrix} \frac{1}{F_1} & 0 & 0 \\ 0 & \frac{1}{F_2} & 0 \\ 0 & 0 & \frac{1}{F_3} \end{pmatrix}^T \begin{pmatrix} \frac{1}{F_1} & 0 & 0 \\ 0 & \frac{1}{F_2} & 0 \\ 0 & 0 & \frac{1}{F_3} \end{pmatrix} = \begin{pmatrix} \frac{F_2F_3}{F_1} & 0 & 0 \\ 0 & \frac{F_1F_3}{F_2} & 0 \\ 0 & 0 & \frac{F_1F_2}{F_3} \end{pmatrix} \tag{3.32}$$

This agrees with Eq. (3.15). In the case of the isotropic outer medium, we have

$$
\begin{aligned}
\varepsilon_2^{ij} &= \varepsilon_0 \delta^{ij} \\
\mu_2^{ij} &= \mu_0 \delta^{ij}
\end{aligned}
\tag{3.33}
$$

Substituting Eqs. (3.31)-(3.33) into Eqs. (3.29)-(3.30), we have

$$
TE: \quad k_{z,aux}^{1,2} = \pm \sqrt{\frac{\xi_{11}}{\xi_{33}} \left(\omega^2 \varepsilon_0 \mu_0 \xi_{22} \xi_{33} - k_x^2 \right)}, \quad \mathbf{E}_t = E \hat{y}, \quad \mathbf{H}_t = E \frac{k_{z,aux}^{1,2}}{\omega \mu_0 \xi_{11}} \hat{x}
\tag{3.34}
$$

$$
TM: \quad k_{z,aux}^{3,4} = \pm \sqrt{\frac{\xi_{11}}{\xi_{33}} \left(\omega^2 \varepsilon_0 \mu_0 \xi_{22} \xi_{33} - k_x^2 \right)}, \quad \mathbf{E}_t = E \hat{x}, \quad \mathbf{H}_t = -E \frac{\omega \varepsilon_0 \xi_{11}}{k_{z,aux}^{3,4}} \hat{y}
\tag{3.35}
$$

for the auxiliary layer, and

$$
TE: \quad k_{z,out}^{1,2} = \pm \sqrt{\omega^2 \varepsilon_3 \mu_3 - k_x^2}, \quad \mathbf{E}_t = E \hat{y}, \quad \mathbf{H}_t = E \frac{k_{z,out}^{1,2}}{\omega \mu_3} \hat{x}
\tag{3.36}
$$

$$
TM: \quad k_{z,out}^{3,4} = \pm \sqrt{\omega^2 \varepsilon_3 \mu_3 - k_x^2}, \quad \mathbf{E}_t = E \hat{x}, \quad \mathbf{H}_t = -E \frac{\omega \varepsilon_3}{k_{z,out}^{3,4}} \hat{y}
\tag{3.37}
$$

for the outer medium. Finally, we obtain the reflection coefficients for both TE and TM excitation. To this end, we suppose and incident field (TE or TM) in the auxiliary layer propagating towards the outer medium and see if there are TE or TM reflected and transmitted waves, demanding equality of the tangential fields at the boundary between both media. For simplicity, we assume that $z = 0$ at the boundary. For TE excitation we have in matrix notation

$$
\begin{pmatrix} 0 \\ 1 \\ -\frac{k_{z,aux}^1}{\omega \mu_0 \xi_{11}} \\ 0 \end{pmatrix} + R_{11} \begin{pmatrix} 0 \\ 1 \\ \frac{k_{z,aux}^1}{\omega \mu_0 \xi_{11}} \\ 0 \end{pmatrix} + R_{21} \begin{pmatrix} 1 \\ 0 \\ 0 \\ -\frac{\omega \varepsilon_0 \xi_{11}}{k_{z,aux}^1} \end{pmatrix} = T_{11} \begin{pmatrix} 0 \\ 1 \\ -\frac{k_{z,out}^1}{\omega \mu_3} \\ 0 \end{pmatrix} + T_{21} \begin{pmatrix} 1 \\ 0 \\ 0 \\ -\frac{\omega \varepsilon_3}{k_{z,out}^1} \end{pmatrix}
\tag{3.38}
$$

From which we deduce that

$$
R_{21} = T_{21} = 0
\tag{3.39}
$$

$$
R_{11} = \frac{\mu_3 k_{z,aux}^1 - \mu_0 \xi_{11} k_{z,out}^1}{\mu_3 k_{z,aux}^1 + \mu_0 \xi_{11} k_{z,out}^1} \qquad T_{11} = \frac{2 \mu_3 k_{z,aux}^1}{\mu_3 k_{z,aux}^1 + \mu_0 \xi_{11} k_{z,out}^1}
\tag{3.40}
$$

R_{11} and T_{11} are the TE reflection and transmission coefficients for TE excitation. R_{21} and T_{21} are the cross-polarization reflection and transmission coefficients from TE excitation to TM polarized waves. Analogously, for the TM case we have:

$$
\begin{pmatrix} 1 \\ 0 \\ 0 \\ \frac{\omega\varepsilon_0\xi_{11}}{k^1_{z,aux}} \end{pmatrix} + R_{12} \begin{pmatrix} 0 \\ 1 \\ \frac{k^1_{z,aux}}{\omega\mu_0\xi_{11}} \\ 0 \end{pmatrix} + R_{22} \begin{pmatrix} 1 \\ 0 \\ 0 \\ -\frac{\omega\varepsilon_0\xi_{11}}{k^1_{z,aux}} \end{pmatrix} = T_{12} \begin{pmatrix} 0 \\ 1 \\ -\frac{k^1_{z,out}}{\omega\mu_3} \\ 0 \end{pmatrix} + T_{22} \begin{pmatrix} 1 \\ 0 \\ 0 \\ -\frac{\omega\varepsilon_3}{k^1_{z,out}} \end{pmatrix}
$$

$$(3.41)$$

and

$$R_{12} = T_{12} = 0 \tag{3.42}$$

$$R_{22} = \frac{\xi_{11}\varepsilon_0 k^1_{z,out} - \varepsilon_3 k^1_{z,aux}}{\xi_{11}\varepsilon_0 k^1_{z,out} + \varepsilon_3 k^1_{z,aux}} \qquad T_{22} = \frac{2\xi_{11}\varepsilon_0 k^1_{z,out}}{\xi_{11}\varepsilon_0 k^1_{z,out} + \varepsilon_3 k^1_{z,aux}} \tag{3.43}$$

In a similar way to the previous case, R_{22} and T_{22} are the TM reflection and transmission coefficients for TM excitation. R_{12} and T_{12} are the cross-polarization reflection and transmission coefficients from TM excitation to TE polarized waves. Finally, substituting Eq. (3.32) and Eqs. (3.34)-(3.37) into the previous equations, we arrive to Eq. (3.16):

$$R_{TE} = R_{11} = \frac{\mu_{r3}\sqrt{\omega^2\varepsilon_0\mu_0 F_1^2 - k_x^2} - F_2\sqrt{\omega^2\varepsilon_3\mu_3 - k_x^2}}{\mu_{r3}\sqrt{\omega^2\varepsilon_0\mu_0 F_1^2 - k_x^2} + F_2\sqrt{\omega^2\varepsilon_3\mu_3 - k_x^2}} \tag{3.44}$$

$$R_{TM} = R_{22} = \frac{F_2\sqrt{\omega^2\varepsilon_3\mu_3 - k_x^2} - \varepsilon_{r3}\sqrt{\omega^2\varepsilon_0\mu_0 F_1^2 - k_x^2}}{F_2\sqrt{\omega^2\varepsilon_3\mu_3 - k_x^2} + \varepsilon_{r3}\sqrt{\omega^2\varepsilon_0\mu_0 F_1^2 - k_x^2}} \tag{3.45}$$

3.5

PAPER 9. EXCITING SURFACE PLASMONS WITH TRANSFORMATION MEDIA

Exciting surface plasmons with transformation media

Carlos García-Meca[*], **Rubén Ortuño, Javier Martí, and Alejandro Martínez**

Nanophotonics Technology Center, Universidad Politécnica de Valencia, Camino de Vera s/n
46022, Valencia, Spain
[*]*cargarm2@ntc.upv.es*

ABSTRACT

We present a way of exciting surface plasmon polaritons along non-patterned metallic surfaces by means of a flat squeezing slab designed with transformation optics. The slab changes the dispersion relation of incident light, enabling evanescent coupling to propagating surface plasmons. Unlike prism couplers, the proposed device does not introduce reflections at its input interface. Moreover, its compact geometry is suitable for integration. A feasible dielectric implementation of the coupler is suggested. Finally, we show that the angular response of the device can be engineered by using a non-uniform compression factor. As an example, we design a coupler with a half-power angular bandwidth 2.5 times higher than that of a conventional dielectric coupler.

1. Introduction

Surface plasmon polaritons (SPPs) are hybrid electron-photon excitations that are trapped at the interface between a dielectric and a conductor [1-3]. This property of SPPs allows us to concentrate electromagnetic fields at the nanoscale by using subwavelength metallic structures. The branch of plasmonics exploits this unparalleled light-concentration ability of metals for a wide range of applications [2-5]. These include the miniaturization of photonic circuits, modulators and photodetectors, the enhancement of non-linear phenomena, the realization of extremely sensitive biosensors, and the improvement of the efficiency of photovoltaic cells. Recently, the use of transformation optics (TO) has been proposed to fully control the propagation of SPPs [6-9]. This technique enables us to engineer electromagnetic space by implementing arbitrary geometries and coordinate transformations with suitable media [10-12]. This way, TO makes it possible to design a variety of devices for SPPs such as cloaks, beam shifters, extreme bends, lenses, and wave adapters [6-9]. Although all these works have focused on flow control, SPPs need to be excited before they can be manipulated. Due to their bound nature, the momentum of SPPs is always higher than that of free-space photons of the same frequency [1-3]. Therefore, it is not possible to directly excite SPPs with free-space light. There exist several techniques to provide the required additional momentum for far-field excitation of SPPs. The most important ones are based on gratings or prism

couplers [1-3,13]. The former consists of structuring periodically the metal surface or surrounding dielectric. If the gratings are sufficiently deep, the SPP dispersion relation (DR) can be significantly altered by the periodic pattern and photonic bandgaps and localized modes may appear [2,3]. The latter is based on the use of a prism placed next to a thin metal film. For instance, in the Kretschmann configuration, light entering the prism at a right angle increases its momentum by a factor equal to the prism index. When light reaches the prism-metal interface, total internal reflection occurs and the wave evanescently tunnels to the other metal side (in contact with air), where the SPP is excited [3,13]. The prism shape imposes a minimum size for the coupler that may not be suitable for integration. Here we propose an alternative way to excite SPPs with the help of TO. Specifically, we show that a properly-designed flat slab that performs a spatial compression can play the role of a prism coupler with important advantages.

2. Theory

Light squeezers based on TO have been extensively studied from the spatial viewpoint [14-18]. However, although there exist some works that link Fourier optics and TO [19], little attention has been paid to the properties of squeezers in the Fourier domain. We begin by analyzing this kind of devices regarding them as k-space filters. For simplicity, we will focus on a two-dimensional problem (invariant in the y-direction), although the results could be extended to three dimensions. In flat-space TO, one starts from a virtual space and performs a certain coordinate transformation in such a way that electromagnetic fields are distorted in the desired manner. It is possible to implement this deformation in real physical space by filling it with the appropriate relative permittivity ε^{ij} and permeability μ^{ij} [10,12]. Our compressing device will result from transforming a rectangular region A'B'C'D' in virtual empty space into region ABCD in physical space [Fig 1(a-b)].

Fig. 1. (a) Virtual space (b) Physical space (c) Squeezer and propagating waves inside and outside it

Both spaces are described by a Cartesian system (after reinterpretation) with coordinates x', y', z' and x, y, z. The squeezer is placed between isotropic media characterized by relative constitutive parameters $\varepsilon_{in} = \mu_{in} = 1$ and ε_{out}, μ_{out}. The field **A** is polarized along the y-direction (**A** = A_y**y**), with **A** being the electric (magnetic) field **E** (**H**) for TE (TM) waves. We denote the Fourier transform of $A_y(x,z)$ in the x-variable as $\hat{A}_y\left(k_x, z\right)$, where k_x is the transverse component of the wavevector **k**. Our aim is to obtain the relation between incident, reflected and transmitted waves $\hat{A}_{IN}\left(k_x\right)$, $\hat{A}_R\left(k_x\right)$ and $\hat{A}_T\left(k_x\right)$ [see Fig. 1(c)]. A general transformation is given by $x = x\ (x',z')$, $y = y'$ and $z = z(x',z')$. The transformation can be whatever, except at the boundaries. In particular, we want the identity transformation at $z' = 0$ in order to avoid reflections at the input boundary, *i.e.*, $x(x',0) = x'$ and $z(x',0) = 0$. At $z' = d'$, we want the transformation to satisfy $\partial x / \partial x' = 1/F$ (F is the compression factor along the x-direction) and $z(x',d') = d$. The first condition implies that the compression is uniform at the output interface. The second ensures that the output boundary is flat. With these simplifications, it can be shown that (derivation details are given in the appendix):

$$\hat{A}_R\left(k_x\right) = \hat{A}_{IN}\left(k_x\right) R\left(k_x F\right) M^2\left(k_x\right)$$
$$\hat{A}_T\left(k_x\right) = \frac{1}{F} \hat{A}_{IN}\left(k_x / F\right) T\left(k_x\right) M\left(k_x / F\right)$$

(1)

with $M(k_x) = \exp\left(i\sqrt{k^2 - k_x^2}\, d'\right)$. For TM polarization:

$$R(k_x) = \frac{\varepsilon_{out}\sqrt{k_0^2 F^2 - k_x^2} - \sqrt{k_0^2 \varepsilon_{out}\mu_{out} - k_x^2}}{\varepsilon_{out}\sqrt{k_0^2 F^2 - k_x^2} + \sqrt{k_0^2 \varepsilon_{out}\mu_{out} - k_x^2}}.$$

(2)

$T(k_x)$ can be obtained from the relation $T(k_x) = 1 + R(k_x)$. The coefficients $R_2(k_x)$ and $T_2(k_x)$ for light impinging from the right at $z = d$ are given by $R_2(k_x) = -R(k_x)$ and $T_2(k_x) = 1 + R_2(k_x)$. To choose a specific transformation, we gave priority to those requiring only dielectric media, as the main difficulty at optical frequencies lies on achieving magnetic materials. Since we are dealing with a two-dimensional problem, only some components of the constitutive parameters need to be implemented. For TE polarization the tensor components that affect the fields are ε^{yy}, μ^{tt} and μ^{ll}, being t and l the in-plane tensor principal directions. In this case, the problem can be solved by using quasi-conformal mappings, which give rise to $\mu^{tt} \approx \mu^{ll} \approx 1$ [18,20]. In the geometrical optics regime, such a medium should work for both polarizations. Nonetheless, an exact realization for TM waves involves the implementation of μ^{yy}, ε^{tt} and ε^{ll}. It can be shown that $\mu^{yy} = 1$ if we use a transformation of the form $x = x'f_1(z')$, $z = f_2(z')$, with $f_1(z') = (df_2(z')/dz')^{-1}$. Here we will employ the functions $f_1(z') = 1/(1+Cz')$ and $f_2(z') = z'(1+Cz'/2)$. This way, the exact realization of the squeezer only requires an anisotropic dielectric. For a squeezer length d as small as 3 µm, only moderate refractive indices, approximately ranging from 0.5 to 2, are required. These values can be relaxed by using a lower compression factor or longer

lengths. Moreover, $f_1(z')$ and $f_2(z')$ could be optimized to further adjust this range. The implementation of anisotropic dielectrics is feasible with the use of multilayer structures [9,19]. Remarkably, an exact dielectric realization of a compressing device working simultaneously for both polarizations could be achieved, since we only need to implement ε^{tt} and ε^{ll} for TM polarization and ε^{yy} for TE polarization.

In order to verify Eqs. (1-2), a squeezer with $F = 2$ embedded in air ($\varepsilon_{out} = \mu_{out} = 1$) was simulated with COMSOL Multiphysics for TM polarization. In Fig. 2, the theoretical values of $R(k_x)$ and $T(k_x)$ are compared with the relations between simulated $\hat{A}_{IN}(k_x)$, $\hat{A}_R(k_x)$, and $\hat{A}_T(k_x)$ for light impinging from the left, finding an excellent agreement. Similar results were obtained for light impinging from the right.
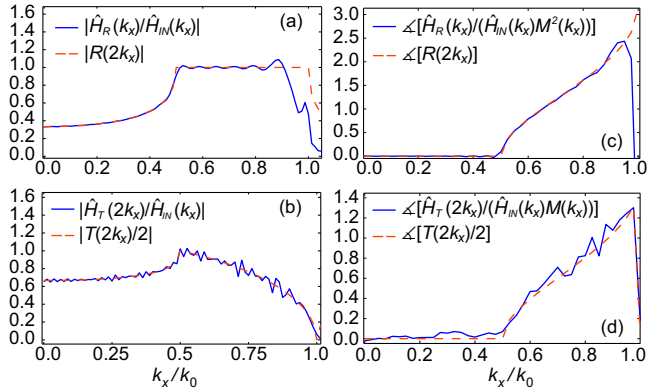
Fig. 2. Comparison of theoretical $R(k_x)$ and $T(k_x)$ with the corresponding relations between simulated fields

3. Excitation of SPPs with a squeezing flat slab

As shown by Eq. (1), in addition to changing the amplitude of incident waves, the squeezer performs an expansion in k_x by a constant factor F, whilst frequency is conserved. This change in the DR suggests that the squeezer could be used to excite SPPs. To illustrate this idea, we study the situation depicted in Fig. 3. A thin metal film (thickness t) is placed next to the output interface of a squeezer. The whole system is surrounded by air. Light impinges onto the squeezer at an angle φ with $k_x = k_0\sin(\varphi)$, where $k_0 = 2\pi/\lambda$ and λ is the free-space wavelength. The curve associated to its DR and that of an SPP propagating along the metal-air interface never cross and direct coupling is not possible. However, after passing through the squeezer, the DR of free-space light is scaled in k_x by a factor F and intersects the SPP DR curve.

Fig. 3 (a) Air light DR (orange), expanded air DR (blue), and metal-air SPP DR (grey) (b) SPPs excitation configuration

Thus, light exiting the squeezer can tunnel through the metal and excite the SPP along the metal-air surface via evanescent coupling. Since the squeezer expands $k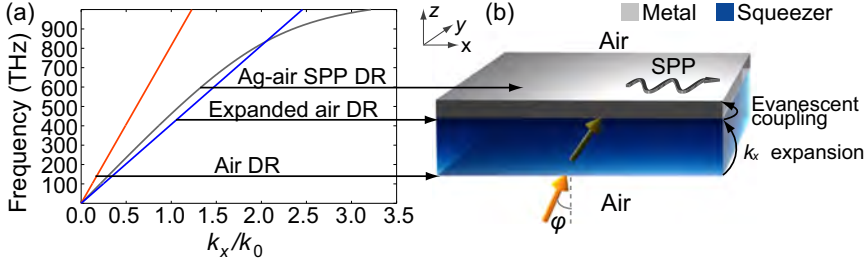_x$ by F, this is analogous to using a prism with refractive index F in the Kretschmann configuration. As an example, we consider a typical situation with $\lambda = 632.8$ nm (HeNe laser), $F = 1.766$ (Sapphire refractive index), and $t = 45$ nm [13]. As for the metal, we use Ag, whose permittivity was found to be $\varepsilon_m = -15.98 + 0.72i$ at this wavelength in [13]. We can deduce the value of k_x for which the SPP is excited at λ from the reflection coefficient $\Gamma(k_x)$ of the system squeezer-metal-air. Since there are no reflections at the input, we only need to take into account the squeezer-metal and metal-air interfaces. By using Eq. (2) and Fresnel equations we calculated $\Gamma(k_x)$ (see Fig. 5). The SPP excitation is stronger at the $\Gamma(k_x)$ minimum, at $k_x = 1.029 \cdot 10^7$ rad/m. This is also the value of k_x at the squeezer output. According to Eq. (1), this corresponds to $k_x = 1.029 \cdot 10^7/1.766 = 5.83 \cdot 10^6$ rad/m for incident light ($\varphi \approx 36^\circ$). Finally, we simulate this example. A Gaussian beam impinging onto the squeezer at $\varphi = 36^\circ$ is used as the source. SPPs only exist for TM polarization, for which we check our device. The simulated power flow is rendered in Fig. 4(a).
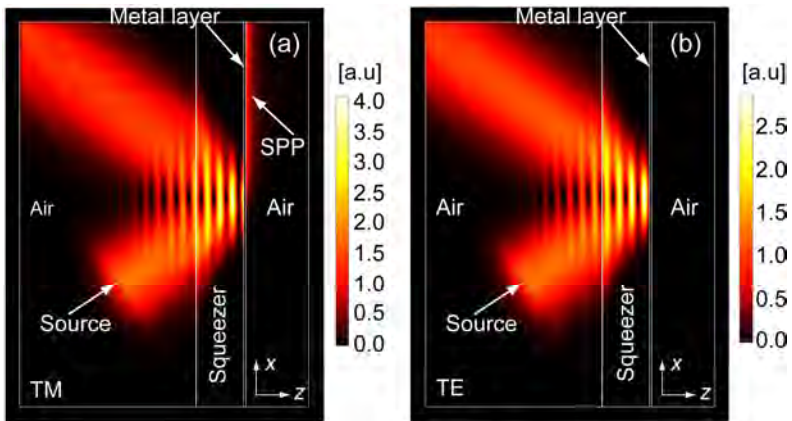

Fig. 4 Simulated SPP excitation ($d = 1.5$ μm). Absolute value of the power flow for (a) TM and (b) TE polarization.

The beam smoothly enters the squeezer, reaches the metal layer and tunnels through it, launching the SPP. As a verification test, we repeated the simulations for TE polarization [Fig. 4(b)]. As expected, no SPP is excited in this case. It is worth noting that, unlike in prism couplers, no Fabry-Perot interference exists within the squeezer because no reflections occur at its input interface. As a consequence, the power transferred to the SPP does not depend on the size of the squeezer. In this sense, the proposed excitation configuration mimics a dielectric-metal-air system with the source embedded inside the dielectric [13], but with the advantage that the source can be placed outside the system without the need of giving the dielectric a prism shape.

4. Broadening the angular bandwidth

According to Fig. 3, SPPs can be excited only at the angle whose associated k_x matches that of the SPP. In a more realistic picture, the SPP resonance has a certain width, as seen in Fig. 5, where $\Gamma(k_x)$ is depicted (the coefficient for a system dielectric-metal-air turns out to be the same if the dielectric refractive index is F). The strength of the excitation is higher at the minimum of $\Gamma(k_x)$, but waves with k_x around the optimal one also excite the SPP to a lesser extent. Moreover, in many cases the incident wave is not a plane wave and its power spectral density (PSD) spreads over a finite region in k_x (for instance, when using a laser or the output of an optical fiber). This allows the excitation of SPPs at a set of angles determined by the source distribution in the angular spectrum. To analyze the angular bandwidth of the proposed device and compare it with that of a prism coupler, we consider the case in which the source is a Gaussian beam with the same excitation configuration as in Fig. 4. The beam axis always crosses the point $x = 0$, $z = d$. In order to avoid Fabry-Perot resonances, we model the prism coupler as a semi-infinite dielectric medium that extends over the interval $z \in (-\infty, d)$, with the source embedded within the dielectric (configuration of Fig. 4, but replacing the squeezer and left air region by the dielectric). To be comparable with the squeezer, the dielectric refractive index is taken to be equal to the compression factor F (see discussion above). In Fig. 5(a) we show the profile of the field that impinges onto the metal film in each case (at $z = d$), which we call $A(x,d)$ to follow the notation of Fig. 1. The beam exiting the squeezer is a compressed version of that exiting the dielectric. Therefore, its associated spectral distribution $\hat{A}(k_x, d)$ is wider than that of the dielectric. This results in a broader angular bandwidth, as we can infer from Fig. 5. When φ is the optimal one [Fig. 5(c)], both spectral distributions are centered at the minimum of $\Gamma(k_x)$, providing the maximum excitation intensity. Naturally, the excitation strength is higher in the case of the prism, since the PSD of the wave exiting the squeezer is lower due to the spreading in k_x that it performs. However, when we decrease φ [Fig. 5(b)], both spectral distributions shift to the left. Now, the PSD overlapping the dip in $\Gamma(k_x)$ is very low in the prism case. Due to its broader spectral extension, the PSD is much higher in the squeezer case, and so is the excitation strength. The situation is similar at larger values of φ [Fig. 5(d)].
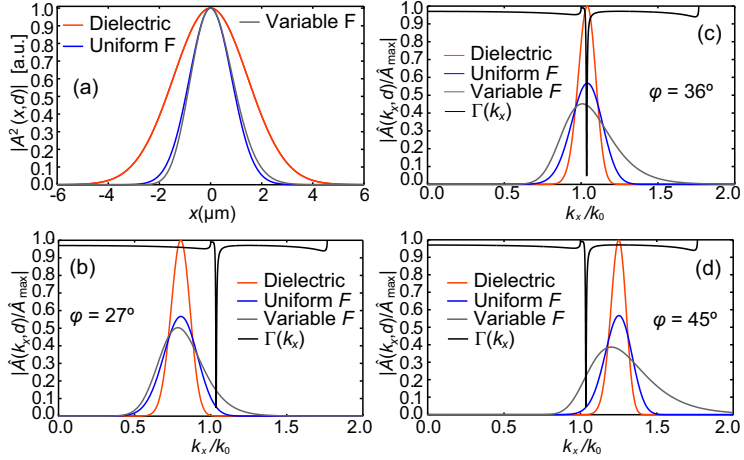
Fig. 5. (a) Field $A(x,d)$ impinging onto the metal film after exiting the dielectric coupler (orange), uniform squeezer (blue) and variable squeezer (grey). (b-d) Corresponding $\hat{A}(k_x,d)$ normalized to its maximum value $\hat{A}_{max}$ (reached by the dielectric coupler) at different angles of incidence φ. $\Gamma(k_x)$ is shown in black.

It is worth mentioning that the coupling efficiency can be significantly lower in a real prism coupler than in the considered ideal case, depending on the reflections that take place at the input interface. Moreover, due to these reflections, a secondary SPP can be excited in the undesired direction. To quantify the angular bandwidth of dielectric and squeezer couplers, we performed a series of simulations at different angles. The source field distribution is the same for both couplers, except for a multiplicative constant, to ensure that the power radiated by the source is the same in all cases. In Fig. 6(a) we depict the electric field amplitude of the excited SPP at the metal surface as a function of φ. For the dielectric coupler, the half-power angular bandwidth (BW) was found to be 4º, while in the case of the squeezer, a value of 7.1º was obtained.

Fig. 6 (a) Electric field amplitude of the excited SPP at the metal surface as a function of the ϕ. Orange: dielectric coupler. Blue: uniform squeezer. Grey: variable squeezer (b) Transformation used for the variable squeezer at $z = d$

These results are explained by the previous discussion and the information in Fig. 5. We have seen that the squeezer coupler presents a higher BW becaus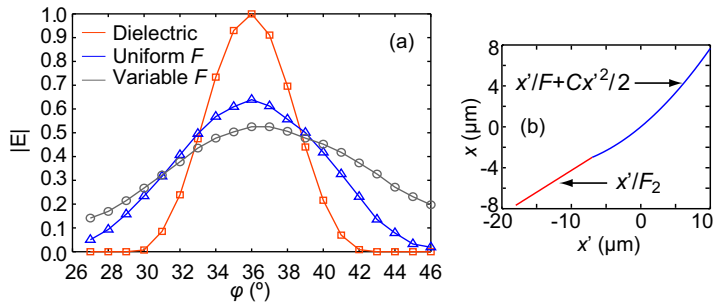e of the compression in x (expansion in k_x) that it performs. This suggests that we could control the device BW by engineering the way in which the fields are transformed. For instance, we could further increase the BW by allowing a compression factor that varies with the x-coordinate at the squeezer output. Intuitively, a variable compression introduces more spatial frequencies and the transformed beam should have a broader associated PSD. As an example, consider the transformation $x = x'(1\text{-}z/d) + zg(x')/d$, $y = y'$, and $z = z'$, with $g(x') = x'/F + Cx'^2/2$ for $x' \geq x_0$ and $g(x') = x'/F_2$ for $x' < x_0$, C being a constant. At $z = 0$ we have the identity transformation. At $z = d$ and for $x' \geq x_0$ the compression varies linearly with x', being equal to F at $x = 0$. In order to keep this variable compression factor within a reasonable range of values, our transformation only performs a uniform scaling for $x' < x_0$. F_2 is chosen so that the transformation is continuous at x_0. In Fig. 5(a) we render the appearance of the previous Gaussian beam after undergoing this transformation with $F = 1.766$, $F_2 = 2.346$, $C = 4\cdot10^5$ m^{-1} and $x_0 = -7$ μm. The transformation at $z = d$ is shown in Fig. 6(b). Owing to the non-uniform compression, the transformed beam has no symmetry with respect to the origin. As a consequence, $\hat{A}(k_x, d)$ is also non-symmetric and extends over a broader spectral range. At the optimal coupling angle, the PSD of the wave exiting the variable squeezer is slightly lower than that of the uniform one [Fig. 5c]. However, at angles away from the optimal one, the PSD is significantly larger for the variable squeezer [Fig. 5(b,d)], which implies a widening of the angular bandwidth. Although the results in Fig. 5 only provide a qualitative description (the reflection coefficients of both squeezers are different and this affects the coupling efficiency) they capture the essential features of both devices. Simulations confirmed the behavior predicted for the variable squeezer (see Fig. 6), which reaches a BW of 10.1º (2.5 times that of the dielectric coupler). Note that the variable squeezer always broadens the angular bandwidth (even if the source is a plane wave). This technique not only allows us to broaden the BW, but also to achieve other coupler angular responses by using different mappings that properly transform the source PSD. Although we cannot use the previous dielectric implementation for the variable squeezer [the transformation is not of the form $x = x'f_1(z')$], a dielectric realization could still be possible, for instance, by allowing a curved output boundary.

5. Conclusions

In summary, we have presented an alternative way of exciting SPPs with the help of TO. To this end, we exploit the modification in the DR introduced by a squeezing device. The squeezer plays the role of a prism coupler but is more suitable for integration because of its flat geometry and small dimensions. Moreover, it does not introduce reflections at its input interface, preventing the appearance of Fabry-Perot resonances and the excitation of SPPs in the undesired direction. The implementation of the squeezer can be achieved with dielectric anisotropic materials. Finally, we have shown that the coupler angular

bandwidth can be broadened by using a variable compression. As an example, we have designed a device with a BW 2.5 times higher than that of a conventional dielectric coupler. This technique could pave the way for engineering SPP couplers with tailor-made angular responses.

Acknowledgements

Appendix

A detailed derivation of Eq. (1) is provided next. The fields propagating in physical space can be expressed as a function of those in virtual space. In component notation:

$$A_i(x,z) = \Lambda_i^{i'} A_{i'}\left(x'(x,z), z'(x,z)\right), \tag{3}$$

with $\Lambda_i^{i'} = \partial x_i / \partial x_{i'}$, i = 1, 2, 3, and $x_1 = x$, $x_2 = y$, $x_3 = z$, with analogous expressions for primed coordinates. Since we have the identity transformation at z' = 0, then $x(x',0) = x'$ and $z(x',0) = 0$. Therefore, using Eq. (3) and taking into account that the only non-vanishing component of **A** is $A_2 = A_y$:

$$A_y(x,0) = \Lambda_2^{i'} A_{i'}\left(x'(x,0), z'(x,0)\right) = A_{y'}(x,0). \tag{4}$$

At z' = d' we also have the restrictions $\partial x / \partial x' = 1/F$ and $z(x',d') = d$. The first condition implies that the compression is uniform at the device output interface, leading to $x = x'f(z')$ at z' = d', i.e., $x(x',d') = x'/F$, if there is no translation in x at this point. With these simplifications, we can write:

$$A_y(x,d) = \Lambda_2^{i'} A_{i'}\left(x'(x,d), z'(d)\right) = A_{y'}(xF, d'). \tag{5}$$

Our goal is to relate the fields transmitted and reflected by the squeezer with the corresponding incident field as a function of k_x. For this purpose, we will first calculate in Fourier space the relation between the fields at $z = 0$ and $z = d$ inside the device. In virtual space (empty flat space), the relation between the fields at z' = 0 and z' = d' is well known. Specifically, $\hat{A}_{y'}(k_{x'}, d') = \hat{A}_{y'}(k_{x'}, 0) M(k_{x'})$ when propagation is towards increasing values of z [blue arrows in Fig. 1(a)] and $\hat{A}_{y'}(k_{x'}, 0) = \hat{A}_{y'}(k_{x'}, d') M(k_{x'})$ when propagation is towards decreasing values of z [orange arrows in Fig. 1(a)]. $M(k_x)$ is the transfer function

of a free space slab of thickness d', i.e., $M(k_x) = \exp\left(i\sqrt{k^2 - k_x^2}\,d'\right)$. With the aid of Eqs. (4-5), we find for waves propagating towards increasing values of z [blue arrows in Fig. 1(b)]:

$$\hat{A}_y\left(k_x, d\right) = \int_{-\infty}^{\infty} A_y\left(x, d\right)e^{-jk_x x}\,dx = \int_{-\infty}^{\infty} A_{y'}\left(xF, d'\right)e^{-jk_x x}\,dx =$$
$$= \frac{1}{F}\hat{A}_{y'}\left(k_x / F, d'\right) = \frac{1}{F}\hat{A}_y\left(k_x / F, 0\right)M\left(k_x / F\right) \qquad (6)$$

For waves propagating towards decreasing values of z [orange arrows in Fig. 1(a-b)]:

$$\left.\begin{aligned}\hat{A}_y\left(k_x, 0\right) &= \hat{A}_{y'}\left(k_x, d'\right)M\left(k_x\right)\\ \hat{A}_y\left(k_x, d\right) &= \frac{1}{F}\hat{A}_{y'}\left(k_x / F, d'\right)\end{aligned}\right\} \Rightarrow \hat{A}_y\left(k_x, 0\right) = F\hat{A}_y\left(k_x F, d\right)M\left(k_x\right). \qquad (7)$$

Now we consider the squeezer as a block that returns two outputs (reflected and transmitted waves A_R and A_T) under an input (incident wave A_{IN}). The relation between $\hat{A}_{IN}\left(k_x\right)$, $\hat{A}_R\left(k_x\right)$ and $\hat{A}_T\left(k_x\right)$ can be obtained with the help of Fig. 1(c). As mentioned in the main text, the squeezer is placed between isotropic media characterized by relative constitutive parameters ε_{in}, μ_{in} (input medium) and ε_{out}, μ_{out} (output medium) and we consider the input medium to be the same as in virtual space ($\varepsilon_{in} = \mu_{in} = 1$). This way, the transformation is continuous at $z = 0$ and there occur no reflections at this interface. Thus, $\hat{A}_{IN}\left(k_x\right) = \hat{A}(k_x, 0)$ and $\hat{A}_R\left(k_x\right) = \hat{B}(k_x, 0)$. However, the transformation discontinuity at $z = d$ introduces reflections at the (squeezer)-(output medium) interface. The relation between a wave impinging from the left at $z = d$ and the transmitted and reflected waves can be characterized by a pair of reflection and transmission coefficients $R(k_x)$ and $T(k_x)$, in such a way that $\hat{A}_T\left(k_x\right) = \hat{A}(k_x, d)T(k_x)$ and $\hat{B}(k_x, d) = \hat{A}(k_x, d)R(k_x)$.

Moreover, we know that $\hat{A}(k_x, d) = F^{-1}\hat{A}(k_x / F, 0)M\left(k_x / F\right)$ from Eq. (6), and that $\hat{B}(k_x, 0) = F\hat{B}(k_x F, d)M\left(k_x\right)$ from Eq. (7). According to these relations:

$$\hat{A}_R\left(k_x\right) = \hat{A}_{IN}\left(k_x\right)R\left(k_x F\right)M^2\left(k_x\right)$$
$$\hat{A}_T\left(k_x\right) = \frac{1}{F}\hat{A}_{IN}\left(k_x / F\right)T\left(k_x\right)M\left(k_x / F\right) \qquad (8)$$

References

1. H. Raether, *Surface Plasmons on Smooth and Rough Surfaces and on Gratings* (Springer, 1988).
2. W. L. Barnes, A. Dereux, and T. W. Ebbesen, "Surface plasmon subwavelength optics," Nature **424**, 824–830 (2003).
3. S. A. Maier, *Plasmonics: Fundamentals and applications* (Springer, 2007).
4. J. A. Schuller, E. S. Barnard, W. Cai, Y. C. Jun, J. S. White, and M. L. Brongersma, "Plasmonics for extreme light concentration and manipulation," Nat. Mater **9**, 193–204 (2010).
5. M. L. Brongersma and V. M. Shalaev, "The case for plasmonics," Science **328**, 440–441(2010).
6. Y. Liu, T. Zentgraf, G. Bartal, and X. Zhang, "Transformational Plasmon Optics," Nano Lett. **10**, 1991–1997 (2010).
7. P. A. Huidobro, M. L. Nesterov, L. Martín-Moreno, and F. J. García-Vidal, "Transformation Optics for Plasmonics," Nano Lett. **10**, 1985–1990 (2010).
8. M. Kadic, S. Guenneau, and S. Enoch, "Transformational plasmonics: cloak, concentrator and rotator for SPPs," Opt. Express **18**, 12027–12032 (2010).
9. J. Zhang, S. Xiao, M. Wubs, and N. A. Mortensen, "Surface Plasmon Wave Adapter Designed with Transformation Optics," ACS Nano **5**, 4359–4364 (2011).
10. J. B. Pendry, D. Schurig, and D. R. Smith, "Controlling Electromagnetic Fields," Science **312**, 1780–1782 (2006).
11. U. Leonhardt, "Optical conformal mapping," Science **312**, 1777–1780 (2006).
12. U. Leonhardt and T. G. Philbin, "General Relativity in Electrical Engineering," New J. Phys. **8**, 247 (2006).
13. J. R. Sambles, G. W. Bradbery, and F. Yang, "Optical excitation of surface plasmons: an introduction," Contemp. Phys. **32**, 173–183 (1991).
14. M. Rahm, D. A. Roberts, J. B. Pendry, and D. R. Smith, "Transformation-optical design of adaptive beam bends and beam expanders," Opt. Express **16**, 11555–11567 (2008).
15. B. Vasic, G. Isic, R. Gajic, and K. Hingerl, "Coordinate transformation based design of confined metamaterial structures," Phys. Rev. B **79**, 85103 (2009).
16. P. Tichit, S. N. Burokur, and A. Lustrac, "Waveguide taper engineering using coordinate transformation technology," Opt. Express **18**, 767–772 (2009).
17. X. Zang and C. Jiang, "Manipulating the field distribution via optical transformation," Opt. Express **18**, 10168–10176 (2010).
18. C. García-Meca, M. M. Tung, J. V. Galán, R. Ortuño, F. J. Rodríguez-Fortuño, J. Martí, and A. Martínez, "Squeezing and expanding light without reflections via transformation optics," Opt. Express **19**, 3562–3575 (2011).
19. J. Li, S. Han, S. Zhang, G. Bartal, and X. Zhang, "Designing the Fourier space with transformation optics," Opt. Lett. **34**, 3128-3130 (2009).
20. J. Li and J. B. Pendry, "Hiding under the Carpet: A New Strategy for Cloaking," Phys. Rev. Lett. **101**, 203901 (2008).

3.6   Quasi-conformal mappings

One of the main difficulties in transformation optics arises from the fact that anisotropic constitutive parameters must be achieved in order to implement most of the devices based on this technique. This is a direct consequence of the metric being anisotropic, as can be easily seen from the relation between metric and constitutive parameters.

It would be interesting to restrict the transformation or metric that we want to implement in such a way that the required properties are isotropic. This particular case takes place when we implement conformal transformations or, in general, conformally flat spaces whose associated metric is completely defined by one scalar field. Under such transformations, angles are preserved and infinitesimal balls are just scaled and rotated, which is the reason why conformal mappings give rise to isotropic transformation media. Thus, conformal mappings fulfill our simplicity requirement and have been previously used in transformation optics[4] and, to a lesser extent, in transformation acoustics.[134] Unfortunately, except for some specific cases, we usually do not have at our disposal a conformal transformation mapping the considered region in virtual space onto the desired shape in physical space.

A possible solution is to use the so-called quasi-conformal mappings. This kind of mapping transforms infinitesimal balls to ellipsoids of bounded eccentricity. Thus, transformation media resulting from a quasi-conformal mapping have a bounded anisotropy that can be neglected if it is small enough. The advantage of quasi-conformal transformations is that they always exist and can be easily calculated numerically in many cases. We only need to be careful so that this transformation has a negligible associated anisotropy.

Mathematical principles

Consider the case in which we want to implement a two-dimensional coordinate transformation. We assume that the problem is invariant in the z-direction. For simplicity, we will work in

Cartesian coordinates, so that our transformation reads

$$
\begin{aligned}
x &= x\left(x', y'\right)\\
y &= y\left(x', y'\right)\\
z &= z'
\end{aligned}
\tag{3.46}
$$

In this case, the constitutive parameters that implement our transformation can be expressed as (in matrix notation)[6]

$$
\left(\varepsilon^{ij}\right) = \left(\mu^{ij}\right) = \frac{1}{\sqrt{\det \gamma^{ij}}}
\begin{pmatrix}
\gamma^{11} & \gamma^{12} & 0\\
\gamma^{21} & \gamma^{22} & 0\\
0 & 0 & 1
\end{pmatrix}
\tag{3.47}
$$

Now we can locally express the constitutive parameters as a diagonal matrix if we employ a Cartesian coordinate system aligned with their eigenvectors:

$$
\left(\varepsilon_D^{ij}\right) =
\begin{pmatrix}
\varepsilon_x & 0 & 0\\
0 & \varepsilon_y & 0\\
0 & 0 & \boxed{\varepsilon_z}
\end{pmatrix},
\qquad
\left(\mu_D^{ij}\right) =
\begin{pmatrix}
\boxed{\mu_x} & 0 & 0\\
0 & \boxed{\mu_y} & 0\\
0 & 0 & \mu_z
\end{pmatrix},
\tag{3.48}
$$

with[7]

$$
\varepsilon_x = \mu_x = \frac{k + \sqrt{k^2 - 4}}{2},
\tag{3.49}
$$

$$
\varepsilon_y = \mu_y = \frac{k - \sqrt{k^2 - 4}}{2},
\tag{3.50}
$$

$$
\varepsilon_z = \mu_z = \frac{1}{\sqrt{\det \gamma^{ij}}},
\tag{3.51}
$$

$$
k = \frac{\gamma^{11} + \gamma^{22}}{\sqrt{\det \gamma^{ij}}} = \frac{\operatorname{tr}\left(\gamma^{ij}\right)}{\sqrt{\det \gamma^{ij}}}.
\tag{3.52}
$$

Note that ε_z is unchanged after diagonalization. To further simplify the problem we restrict ourselves to propagation of TE waves (**E** directed along the z-direction). As a consequence, only the boxed components in Eq. (3.48) affect the electromagnetic fields. Now imagine that our transformation is conformal so that

$$
\frac{\partial x}{\partial x'} = \frac{\partial y}{\partial y'},
\tag{3.53}
$$

$$
\frac{\partial x}{\partial y'} = -\frac{\partial y}{\partial x'},
\tag{3.54}
$$

[6] γ^{ij} are the contravariant components of the metric tensor in the transformed space, with

$$
\gamma^{11} = \left(\frac{\partial x}{\partial x'}\right)^2 + \left(\frac{\partial x}{\partial y'}\right)^2
$$

$$
\gamma^{22} = \left(\frac{\partial y}{\partial x'}\right)^2 + \left(\frac{\partial y}{\partial y'}\right)^2
$$

$$
\gamma^{12} = \frac{\partial x}{\partial x'}\frac{\partial y}{\partial x'} + \frac{\partial x}{\partial y'}\frac{\partial y}{\partial y'}
$$

$$
\sqrt{\det \gamma^{ij}} = \frac{\partial x}{\partial x'}\frac{\partial y}{\partial y'} - \frac{\partial x}{\partial y'}\frac{\partial y}{\partial x'}
$$

[7] k has the same form when expressed in terms of the covariant metric tensor

$$
k = \frac{\gamma_{11} + \gamma_{22}}{\sqrt{\det \gamma_{ij}}}.
$$

which implies that

$$\begin{matrix} \gamma^{11} = \gamma^{22} = \sqrt{\det \gamma^{ij}} \\ \gamma^{12} = \gamma^{21} = 0 \end{matrix} \Rightarrow \varepsilon_x = \mu_x = \varepsilon_y = \mu_y = 1. \qquad (3.55)$$

Therefore, in this particular situation, we can implement the transformation with a non-magnetic isotropic material of the form

$$\left(\varepsilon_D^{ij} \right) = \begin{pmatrix} n^2 & 0 & 0 \\ 0 & n^2 & 0 \\ 0 & 0 & \boxed{n^2} \end{pmatrix} = n^2 \delta^{ij}, \qquad \left(\mu_D^{ij} \right) = \begin{pmatrix} \boxed{\begin{matrix} 1 & 0 \\ 0 & 1 \end{matrix}} & \begin{matrix} 0 \\ 0 \end{matrix} \\ 0 \quad 0 & 1 \end{pmatrix}, \qquad n^2 = \varepsilon_z = \frac{1}{\sqrt{\det \gamma^{ij}}},$$

$$(3.56)$$

since the relevant boxed components would be the same as in Eq. (3.48). This means that for TE waves, two-dimensional conformal transformations only require a spatially varying refractive index n for their implementation. Unfortunately, there is not always a conformal transformation mapping the virtual domain to the desired physical one or it is just too difficult to find an analytical expression for it. It is here where quasi-conformal mappings come into play. The idea is to obtain a mapping as close as possible to the conformal one and that we can compute numerically. If we could achieve $\mu_x \approx 1$ and $\mu_y \approx 1$, we could set $\mu_x = \mu_y = 1$ assuming a little imperfection in our device. To measure the quality of our mapping, we define the anisotropy factor α as

$$\alpha = \max \left(\sqrt{\frac{\mu_x}{\mu_y}}, \sqrt{\frac{\mu_y}{\mu_x}} \right) \qquad (3.57)$$

It can be easily shown that

$$\alpha + \frac{1}{\alpha} = \sqrt{\frac{\mu_x}{\mu_y}} + \sqrt{\frac{\mu_y}{\mu_x}} = k \geq 2 \qquad (3.58)$$

The *no anisotropy* condition occurs for the minimum value of k, i.e., $k = 2$ (which implies that $\alpha = 1$)[8]

$$\alpha = 1 \Leftrightarrow k = 2 \qquad \text{NO ANISOTROPY CONDITION} \quad (3.59)$$

Therefore, our goal is to minimize k. There exist several theorems providing a solution to this problem when the domain in

[8] Proof.

$$k = \sqrt{\frac{\mu_x}{\mu_y}} + \sqrt{\frac{\mu_y}{\mu_x}} = \frac{1 + \mu_y / \mu_x}{\sqrt{\mu_y / \mu_x}}.$$

We call $t = \mu_y / \mu_x$ and search for the value of t that minimizes k

$$\frac{\partial (1+x)/\sqrt{x}}{\partial x} = 0 \Rightarrow x = 1$$

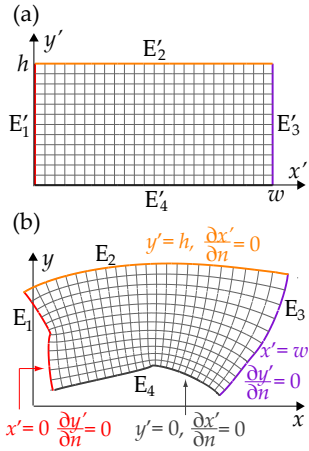$$\Rightarrow \mu_x = \mu_y = 1 \Rightarrow k = 2.$$

(a)

(b)

Figure 3.17: Quasi-conformal mapping from a rectangular domain to an arbitrary shape. Each square is approximately mapped to another square (no local distortion). The meaning of sliding boundary conditions is also shown. Each of the four edges E_i' of the rectangle in virtual space depicted in (a) must be mapped to the specified edge E_i in physical space depicted in (b) up to a sliding freedom. This is achieved by forcing the appropriate mathematical conditions on each edge, as shown in (b), where n represents the direction normal to the boundary of the transformed square.

virtual space is a rectangle. Specifically, it can be shown that, in that case, the maximum value of k is minimized when the metric in the transformed space minimizes the Modified-Liao functional [135,136]

$$\phi = \frac{1}{wh} \int_0^w \int_0^h k^2 \, dx' dy', \qquad (3.60)$$

and we apply Neumann-Dirichlet (sliding) boundary conditions (as shown in Figure 3.17).

Equivalently, the solution to the inverse Laplace equation with the same boundary conditions [135,137]

$$\nabla_\mathbf{x}^2 \mathbf{x}' = 0 \quad + \quad \text{Sliding boundary conditions,} \qquad (3.61)$$

yields the same result. The resulting transformation is known as the *quasi-conformal mapping* and it is the best approximation to the conformal mapping between both domains (being equal to it when the latter exists). Of course, we can solve any of the previous equations numerically and find the corresponding anisotropy factor and refractive index required to implement the transformation.

The use of quasi-conformal mappings has led to interesting devices, such as bends with arbitrary shapes [138] and the concept of carpet cloak [136], which is a special kind of invisibility cloak that makes a curved metallic region appear as a ground plane, enabling us to hide an object behind it. In colloquial language, the object is hidden "under the carpet". In Figure 3.18 we have a typical quasi-conformal mapping used for a carpet cloak device. A rectangular grid in virtual space is transformed into a deformed grid with a bump. In this case the anisotropy factor is $\alpha = 1.04$ (negligible anisotropy). The color in Figure 3.18 represents the refractive index required to implement this transformation. We include an example of the performance of this device in Figure 3.20, where we show the power distribution resulting from a Gaussian beam impinging onto different elements from the left side. When the beam impinges onto a flat metallic wall it is perfectly reflected upwards (Figure 3.20(a)). We would like to deform this wall in order to create a space where we can hide an object as in Figure 3.20(b). Nevertheless, in this case the beam is scattered in a different manner due to

the bump, revealing the curvature of the surface. However, if we cover this curved surface with the carpet cloak, light experiences a flat metallic wall like that in virtual space and is reflected in the same fashion. This way, it is impossible to detect the wall curvature (Figure 3.20(c)).
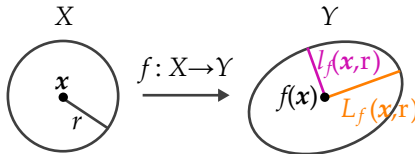
Formal definition

For the sake of completeness, in this section we provide a formal definition of quasi-conformal mapping. Although there exist several equivalent definitions, we present here a metric definition, which we believe is the most intuitive one.

Let $f : X \rightarrow Y$ be a homeomorphism between two metric spaces. For $\mathbf{x}, \mathbf{y} \in X$ and $r > 0$ let

$$L_f(\mathbf{x}, r) = \sup\{|f(\mathbf{x}) - f(\mathbf{y})| : |\mathbf{x} - \mathbf{y}| \leq r\}, \tag{3.62}$$

$$l_f(\mathbf{x}, r) = \inf\{|f(\mathbf{x}) - f(\mathbf{y})| : |\mathbf{x} - \mathbf{y}| \leq r\}. \tag{3.63}$$

(a)

(b)

0.8 1.0 1.2 1.4 1.6 1.8

Figure 3.18: Quasi-conformal mapping for a carpet cloak (a) Rectangular grid in virtual space (b) Deformed grid in physical space. The color represents the required $\varepsilon = n^2$ for its implementation.

X Y

$\mathbf{x}$

r

$f : X \rightarrow Y$

$f(\mathbf{x})$

$l_f(\mathbf{x}, r)$

$L_f(\mathbf{x}, r)$

Figure 3.19: Transformation of an infinitesimal ball under a quasi-conformal mapping.

The ratio

$$H_f(\mathbf{x}, r) = \frac{L_f(\mathbf{x}, r)}{l_f(\mathbf{x}, r)} \tag{3.64}$$

is a measure of the eccentricity of the image of the ball $B(\mathbf{x}, r)$ under f. Then, given $H \geq 1$, f is said to be H-quasiconformal if

$$\lim_{r \to 0} \sup\{H_f(\mathbf{x}, r)\} \leq H \quad \forall x \in X \tag{3.65}$$

This means that infinitesimal balls are transformed into infinitesimal ellipses of bounded eccentricity, as exemplified in Figure 3.19.
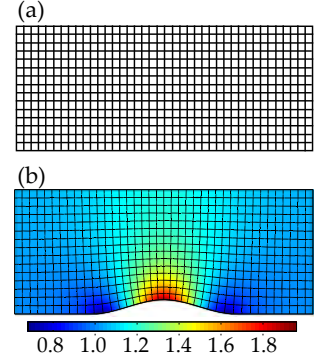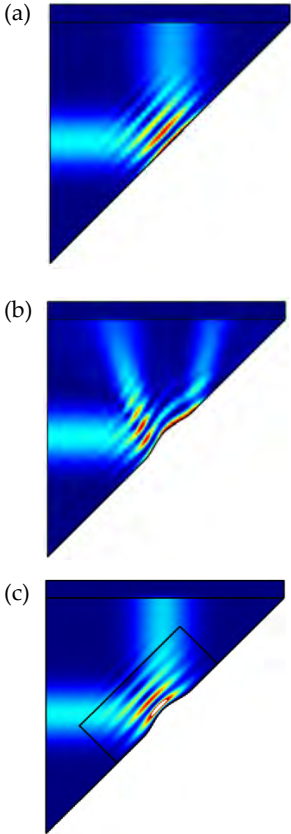
Figure 3.20: Power distribution after a Gaussian beam impinges from the left onto (a) Plane metallic wall. (b) Metallic wall with a bump. (c) Metallic wall with a bump covered by a carpet cloak.

Our contribution: practical squeezers and radiation-pattern-shaping devices

In PAPER10 we show how to use quasi-conformal mappings for the practical implementation of devices that are able to modify the radiation pattern of an isotropic source in almost any desired way.

As we mentioned above, the 2D squeezers presented in the previous section can be implemented with this technique as well. This is an important advantage, since the specific implementations proposed by other authors [132,133] would challenge current state of the art fabrication capabilities. Another disadvantage of those implementations is that lossy resonant elements would be necessary. To illustrate this possibility, we will follow the procedure based on the inverse Laplace equation to solve the problem of the coupling between two metallic waveguides of different cross-section by transforming a piece of waveguide $W1$ into a non-magnetic isotropic realization of the squeezer (see section on squeezing devices). In Figure 3.21 we show the norm of the electric field for this case. All parameters are the same as in Figure 3.16(c), except for the fact that the squeezer is made up of an isotropic non-magnetic material, *i.e.*, just a spatially varying refractive index. We can see in Figure 3.21 that there are almost no reflections in this case either. Specifically, we obtained from the simulation a reflected power of 0.0036%. Thus, we have shown that it is possible to couple both waveguides with only a certain refractive index distribution. In this specific implementation, the required refractive index varies between 0.86 and 2.1 [see Figure 3.21(b)]. Although it is possible to implement a refractive index below unity, it is preferable to have a refractive index range higher or equal to unity. For that purpose, we can just approximate the index by unity in the small regions where it is lower than one. Another possibility is to divide the whole index distribution by its minimum value (0.86). This does not affect the functionality of the device and introduces very weak reflections (as shown by numerical calculations) because the index mismatch is very low. We can of course completely avoid reflections by using the appropriate anti-reflective coating.

Figure 3.21: Implementation of the squeezer with an isotropic spatially varying refractive index. (a) $|\mathbf{E}|$ field distribution. (b) Refractive index profile of the squeezer. For this particular implementation we obtained an anisotropy factor of 1.025. We employed a smooth cosine-like profile for the squeezer.
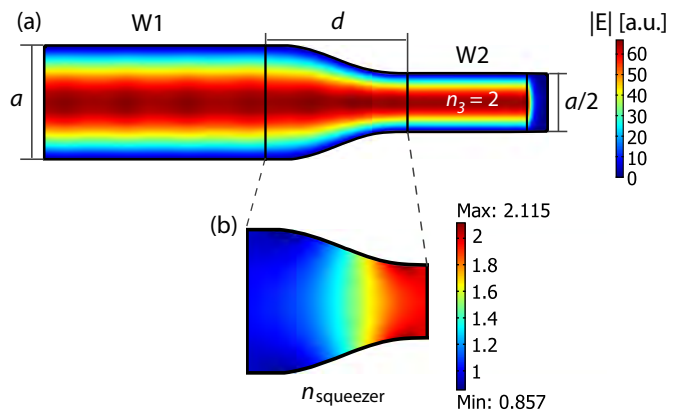
3.7

PAPER10. ENGINEERING ANTENNA RADIATION PATTERNS VIA
QUASI-CONFORMAL MAPPINGS

Engineering antenna radiation patterns via quasi-conformal mappings

Carlos García-Meca,[1,*] Alejandro Martínez,[1] and Ulf Leonhardt[2]

[1]Nanophotonics Technology Center, Universidad Politécnica de Valencia, Camino de Vera s/n 46022, Valencia, Spain
[2]School of Physics and Astronomy, University of St. Andrews, North Haugh, St. Andrews KY16 9SS, United Kingdom
[*]cargarm2@ntc.upv.es

Abstract: We use a combination of conformal and quasi-conformal mappings to engineer isotropic electromagnetic devices that modify the omnidirectional radiation pattern of a point source. For TE waves, the designed devices are also non-magnetic. The flexibility offered by the proposed method is much higher than that achieved with conformal mappings. As a result, it is shown that complex radiation patterns can be achieved, which can combine high directivity in a desired number of arbitrary directions and isotropic radiation in other specified angular ranges. In addition, this technique enables us to control the power radiated in each direction to a certain extent. The obtained results are valid for any part of the spectrum. The potential of this method is illustrated with some examples. Finally, we study the frequency dependence of the considered devices and propose a practical dielectric implementation.

1. Introduction

During the last decade, a variety of complex structures have been proposed to modify the radiation properties of electromagnetic sources. For instance, a near-zero refractive index slab selects only electromagnetic components impinging with a wave vector perpendicular to its interface, transforming an isotropic source into a highly directional beam [1]. Another approach is the use of photonic crystals, which are able to generate a set of directional beams from an omnidirectional embedded source, since propagation is allowed only in some preferred directions inside the crystal, related to the symmetries of the periodic structure. Moreover, inverse engineering can be employed to modify such periodic structure and achieve a desired radiation pattern that need not be symmetric [2]. In the last few years, plasmonic nanoantennas have also attracted considerable attention, as they enable us to extend many radio antenna concepts to the optical range with devices of reduced size. This includes achieving directional emission patterns, for which most works have focused on Yagi-Uda configurations for different purposes [3-6]. Simultaneously, transformation optics [7] has provided an alternative way to mold the radiation properties of antennas [8-18]. This technique makes it possible to design optical media that make light experience a virtual space, different from the physical one. Points

in both spaces (which can be flat or curved) are related by a certain mapping that, together with the metric of those spaces, determines the properties of such optical media [7]. Different transformations have been proposed for a number of applications. These range from the conversion of the cylindrical waves emitted by a line source into four directional beams angularly spaced by 90º [9], to the transformation of more general optical sources that makes them behave as a different virtual source [10-12] and the design of ultra-directive or even invisible antennas [13-15]. The main drawback of this kind of devices is that anisotropic permittivities and permeabilities are required in general, which are difficult to implement.

Recently, the use of conformal transformations [16] has been proposed for antenna engineering [17,18]. Such transformations have the advantage of requiring only isotropic media for their implementation and, for TE polarization (electric field pointing in the direction in which the problem is invariant), only non-magnetic media [7,17,18]. In [17], near-zero constitutive parameters arising from a conformal transformation are employed to transform an isotropic source into one, two or four directional beams. In a more general work, the Schwarz-Christoffel transformation was used to map the circle onto a regular polygon with N sides [18]. The resulting device distributes equally the power of a point source located at the polygon center among N directional beams perpendicular to each polygon side. Thus, these techniques are limited to the design of symmetric antennas radiating in N discrete directions. In this work, we combine this kind of conformal transformations with quasi-conformal mappings to gain more flexibility in the design of radiation-pattern-shaping devices. Although the proposed devices were devised for the optical range, the results are valid for any part of the spectrum. Therefore, normalized distances (in terms of the free-space wavelength λ) are used throughout the text for the sake of generality.

2. Quasi-conformal mappings for antennas

Infinitesimal balls are just scaled and rotated when transformed by a conformal mapping. This is the reason why conformal mappings give rise to isotropic transformation media. Quasi-conformal mappings transform infinitesimal balls to ellipsoids of bounded eccentricity. Thus, transformation media resulting from a quasi-conformal mapping have a bounded anisotropy that can be neglected if it is small enough. Our goal is to change the omnidirectional radiation pattern of a two-dimensional point source. For this purpose, we will consider the transformation of the unit circle (normalized units) in a flat virtual space to another shape in flat physical space. The functionality of the device will be defined solely by the transformation we apply to the boundary of the considered domain in virtual space (the circle in this case). Thus, we are interested in finding a map that simplifies its implementation. Clearly, a conformal mapping fulfils our requirement as it gives rise to isotropic media. However, except for some specific cases, we do not have at our disposal a conformal transformation mapping the unit circle onto the desired shape. To overcome this problem, we will employ quasi-conformal mappings. Since most algorithms used in the calculation of quasi-conformal mappings transform a rectangular

region into other shape, first it is necessary to transform the circle into a rectangle. The best way to do this is by using simple conformal transformations with known analytical expressions. Thus, we will follow a two-step method instead of a direct transformation. First, we will transform the unit circle to a square (with side length $d = 2$) by using a combination of a Möbius transformation mapping the circle to the half upper plane, followed by a Schwarz-Christoffel transformation mapping the half upper plane to the square. The complete transformation is given by Eq. (1):

$$q(w) = \sqrt{-2i}\left(1 - \frac{1}{F\left(\pi/2\,|\,1/2\right)}F\left(\frac{\pi}{2} - \arcsin\left(w\sqrt{i}\right)\Big|\frac{1}{2}\right)\right). \tag{1}$$

$F(\phi\,|\,m)$ is the incomplete elliptic integral of the first kind, with amplitude ϕ and parameter m. We have expressed this two-dimensional transformation as a function of the complex variable $w = w_1 + iw_2$, with $q = q_1 + iq_2$. The refractive index that implements this transformation can be obtained as $n_1 = |dw/dq|$ [7]. As for the second step, we use a quasi-conformal mapping $z(q_1,q_2) = x + iy$ to transform the square to the desired final shape. The advantage of this kind of quasi-conformal transformations is that they always exist and that, they can be easily calculated numerically. We only need to be careful so that this transformation has a negligible associated anisotropy. For a TE two-dimensional problem, the implementation of the exact quasi-conformal mapping would require a permittivity $\varepsilon = \det(g^{ij})^{-1/2}$ and an anisotropic permeability with in-plane components μ_T and μ_L in each of the two principal directions, where g^{ij} is the contravariant metric in the curved coordinates we want to implement [19]. To measure the degree of anisotropy, $\alpha = \max((\mu_T/\mu_L)^{1/2},(\mu_L/\mu_T)^{1/2})$ is usually taken as the anisotropy factor. If α is close to one, $\mu_T \approx \mu_L \approx 1$ and the quasi-conformal mapping can be implemented with negligible error by using only a refractive index distribution $n_2^2 = \varepsilon = \det(g^{ij})^{-1/2}$, as if our mapping were conformal. We will use a simple way of computing such quasi-conformal mappings, which is based on the solution of the inverse Laplace equation supplemented with sliding boundary conditions [20]. In this case, the four sides of the square are mapped to four disjoint specified pieces of the transformed square boundary. The complete transformation refractive index is then given by $n = n_1 n_2$ [7]. In Fig. 1 we illustrate the two steps of this transformation with an example.
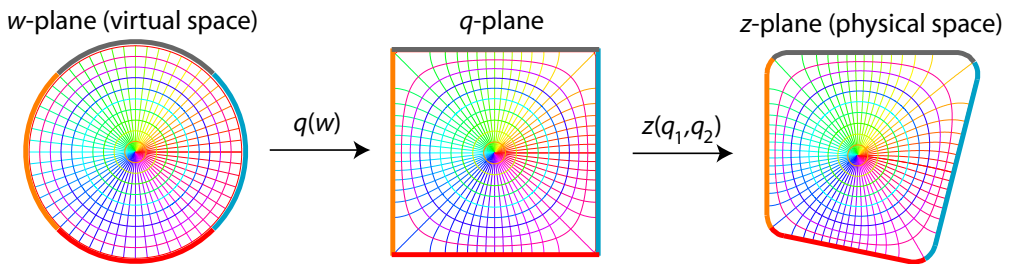

Fig. 1. Mapping of the unit circle to an arbitrary shape by using a conformal transformation $q(w)$ followed by a quasi-conformal one $z(q_1,q_2)$.

Conformal maps preserve angles, *i.e.*, two curves meeting at a certain angle in virtual space are mapped to curves in physical space that meet at the same angle. Lines perpendicular to the unit circle boundary will be perpendicular to its transformed counterpart in physical space. Electromagnetic fields follow this transformation, so light rays emanating from a point source located at the center of the unit circle in original space will be normal to the transformed boundary in physical space as well. In order to shape the radiation diagram of the omnidirectional source, we have to orient each little piece of the transformed boundary so that it is perpendicular to the direction towards which we want to redirect the rays crossing that piece. This way we can engineer the angular distribution of the radiated power. This procedure is not exact because of the wave nature of light and the reflections appearing at the transformed circle boundary, since the transformation is not continuous at it. The other limitation is that we do not have full control of the density of rays crossing the transformed circle boundary. We can only decide where to map each fourth of the circle boundary so that we can distribute the radiated power among four desired sets of angular directions, but we cannot specify the angular distribution within each set. Despite the first limitation, the results achieved by this technique are quite accurate. In addition, the second limitation can be overcome to a certain extent as shown below, increasing the degree of control of the angular power distribution.

3. Examples

In this section we present three examples illustrating the potential of this technique. We will focus on TE waves so that the resulting devices can be implemented with a gradually changing refractive index distribution. As a first example, imagine that we want to divide the power radiated by the point source into four directional beams, each one propagating in an arbitrary direction. To this end, we should use a quasi-conformal mapping transforming each side of the square to a straight line perpendicular to each of these directions. For instance, let as suppose that those directions correspond to $\theta = 90º$, $\theta = 180º$, $\theta = -20º$, and $\theta = -100º$. In Fig. 2(a) we have depicted a possible choice for the boundary of the final device. Note that we have made use of the flexibility allowed by the quasi-conformal mapping technique in order to avoid steep vertices, which have been rounded. This way, the required refractive index n is always greater than zero. We will also apply this kind of smoothing to the next examples. In Fig. 2(b) we show how the calculated mapping transforms the grid in the w-plane depicted in Fig. 1 to the z-plane. The refractive index that implements such mapping is included in Fig. 2(c). In this case, n ranges from 0.1 to 1.75, and α is approximately 1.04 so the anisotropy can be neglected. This also applies for the other examples analyzed below, for which similar values of α are obtained. To verify the behavior of the designed devices, we have performed numerical calculations with the commercially available software COMSOL Multiphysics, based on the finite element technique. Isotropic dielectric media have been used in all simulations (anisotropy neglected). In Fig. 2(d) we render the power flow distribution of a point source located in the transformed center of the circle. In addition, we have calculated the

far-field distribution $E_{far}(\theta)$ radiated by the system. This enables us to evaluate the directivity, which can be defined as $D = |E_{far}(\theta)/E_{omni}|^2$ for a two-dimensional TE problem, where E_{omni} is the electric far field radiated by a two-dimensional point source in any direction. In Fig. 2(e) we have depicted D in polar coordinates for this first example. We can observe that the radiation pattern consists of four well-defined narrow beams in the desired directions (with a maximum angle deviation of 0.1º). The directivity in each of these directions is very similar and is higher than 6 (7.8 dB), with a half-power beamwidth BW between 10º and 13º. For comparison purposes, we simulated the exact implementation of the device (anisotropy not neglected). No appreciable differences were observed, as corresponds to small values of α.
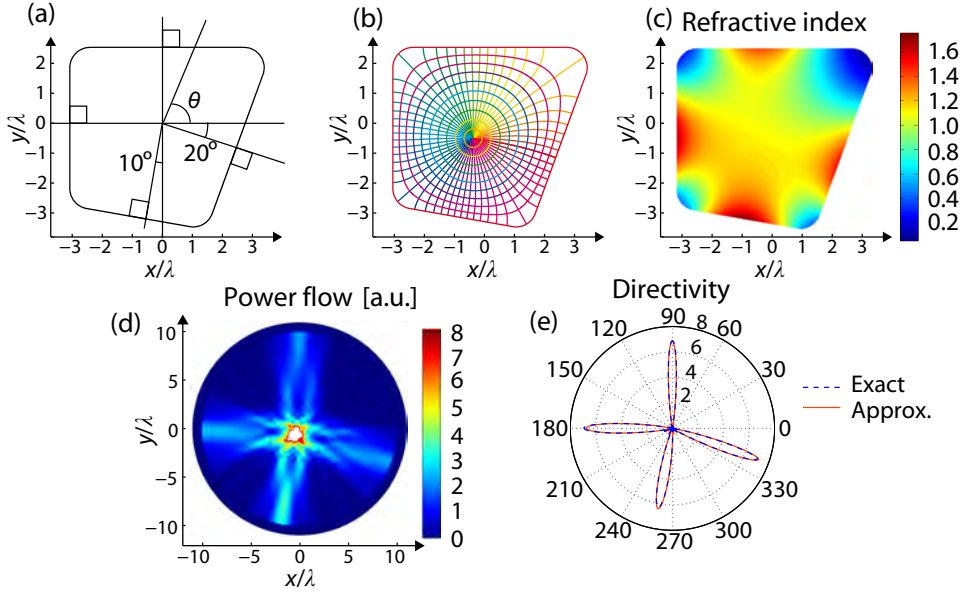

Fig. 2. Control of beam direction: Conversion of an omnidirectional radiation pattern into four narrow beams pointing at any desired direction. (a) Desired boundary of the transformed circle. (b) Resulting quasi-conformal mapping. (c) Refractive index. Simulated (d) power flow, and (e) directivity for the isotropic implementation (red) and exact implementation (blue).

In the second example we show that this technique is not restricted to four-beam antennas and that the power radiated in each direction can be controlled to a certain extent. In this case, imagine that we want to have five beams instead of four, radiating in the directions $\theta = 0º$, $\theta = 90º$, $\theta = 150º$, $\theta = -90º$, and $\theta = -150º$. Moreover, we want the beams associated with the directions $\theta = 150º$ and $\theta = -150º$ to have a smaller directivity than the other ones. These specifications can be accomplished by assigning the left side of the square in the q-plane to two segments in the z-plane, one of them perpendicular to the direction $\theta = 150º$ and the other one to the direction $\theta = -150º$, while leaving the other

three square sides unchanged [Fig. 3(a)]. Since the device is symmetric with respect to the horizontal axis, we know that the beams exiting each of the smaller segments will carry the same power, approximately a quarter of the power carried by each of the other three beams. As in the previous example, the resulting mapping, required refractive index, power flow distribution and directivity are shown in Fig. 3(b-e). The maximum directivity is 3.62 dB for the two secondary lobes and it is between 9.03 dB and 9.2 dB for the main lobes. The refractive index ranges from 0.2 to 1.3.

As a last example, we show that we can also engineer the device to have isotropic radiation within a certain angular range, and not only a set of directional beams. For instance, suppose that we want to have three main lobes radiating in the directions corresponding to $\theta = 0º$, $\theta = 180º$, and $\theta = -90º$, and that we want an isotropic radiation in a 60º angular region defined by the interval $\theta \in [60º, 120º]$. To achieve this, we can transform the upper side of the square in the q-plane to a circular boundary, while leaving the other three square sides with the same orientation [see Fig. 4(a)]. This circular boundary must be an arc subtending an angle of 60º in order to distribute the power uniformly in the desired range. According to Fig. 4(a), the radius r of the circle should be $r = 1/\sin(30) = 2$. The mapping, refractive index (varying between 0.2 and 1.32) and directivity are shown in Fig. 4(b-d).
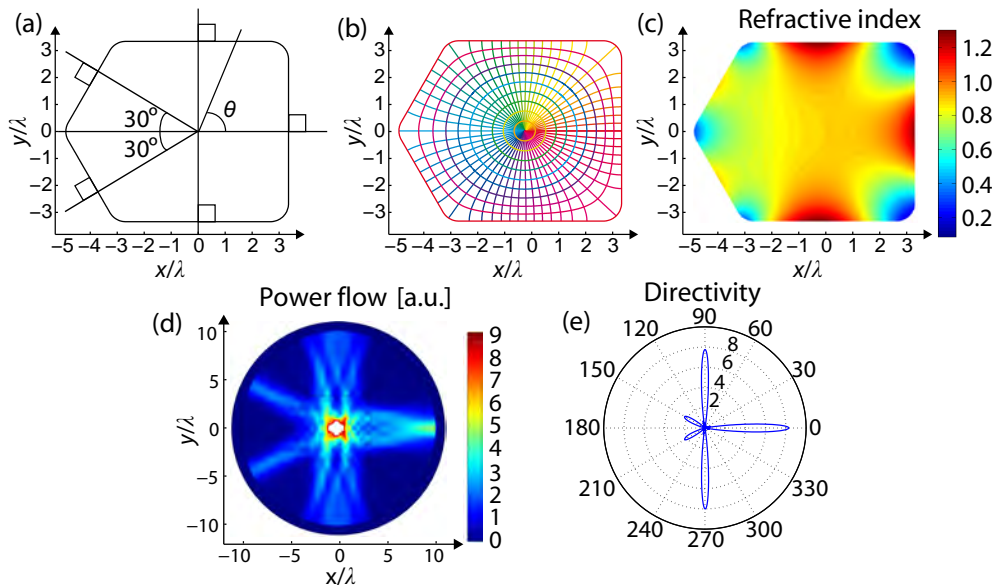

Fig. 3. Control of the number and power of beams: Conversion of an omnidirectional radiation pattern into five narrow beams with different power levels. (a) Desired boundary of the transformed circle. (b) Resulting quasi-conformal mapping. (c) Refractive index. Simulated (d) power flow, and (e) directivity.

For the directional beams, the directivity achieves maximum values of 9.4 dB (θ = 0º and θ = 180º) and 10.1 dB (θ = -90º), with beamwidths of 9.8º. We have included in Fig. 4(e) a detail of the directivity in the region where we desire an isotropic radiation.
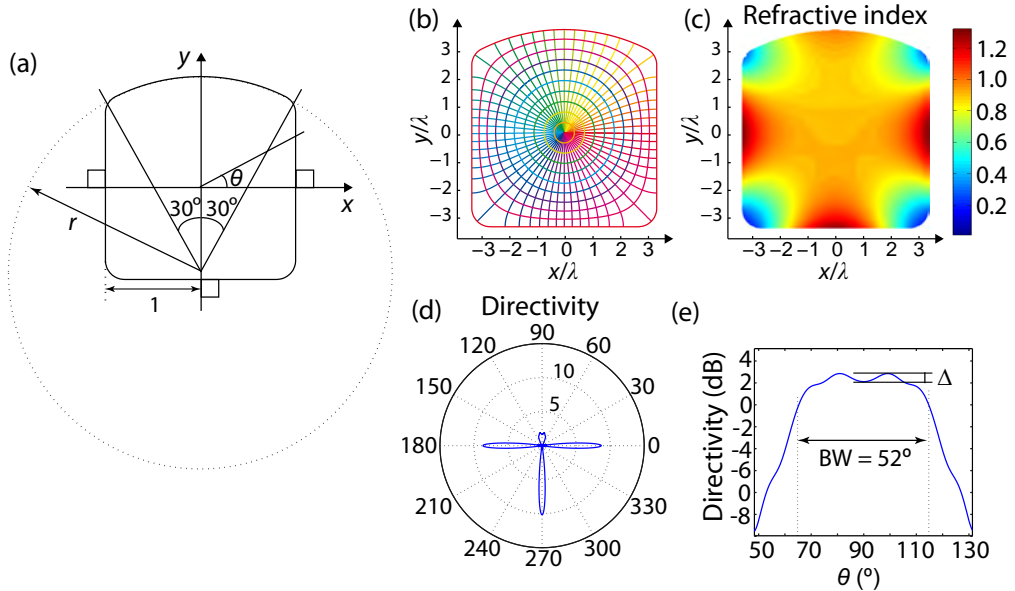

Fig. 4. Generation of a radiation pattern combining high directivity in some directions and isotropic radiation in a desired angular range from an omnidirectional source. (a) Desired boundary of the transformed circle. (b) Resulting quasi-conformal mapping. (c) Refractive index. (d-e) Simulated directivity.

There appears a little ripple with amplitude $\Delta \approx 0.7$ dB owing to reflections at the boundary and the fact that the density of rays is higher at the center of the arc, as shown in Fig. 4(b). Nevertheless, the directivity is higher than 2 dB approximately between 70º and 110º with a beamwidth of around 52º. This last value is somewhat smaller than expected because of the reasons mentioned above and could be corrected by considering a higher angular region in the specifications or by optimizing the radius of curvature of the mapping boundary, which in general could provide a path for engineering a large variety of radiation patterns.

4. Frequency dependence and implementation

The performance of the proposed devices should be frequency-independent, provided that non-dispersive materials are employed for their implementation. However, there exists a limiting upper wavelength for which the performance of the device begins to deteriorate significantly. This is due to the fact that we used concepts of ray optics in the design of our device (see discussion above). Thus, its behavior should be closer to the desired one at shorter wavelengths. To analyze the frequency dependence of the

proposed devices we focused on the example of Fig. 3. In Fig. 5(a-f) we depict the simulated directivity of this device at different wavelengths. We used the size d of the square side (Fig. 1) as the reference length, since the lateral size of the device is of the order of d (the results in Fig. 3 correspond to $d = 6.6\lambda$). As expected, we observe an improvement of all features at shorter wavelengths. Specifically, for sizes of d larger than 20λ the performance is optimal, reaching directivities around 13 dB and half-power beamwidths as small as 4º. On the other hand, for $d = 4\lambda$ the secondary lobes do not point at the desired direction and the directivity is quite low. As an approximate rule, we found that the behavior of the device is acceptable for sizes down to 5λ.
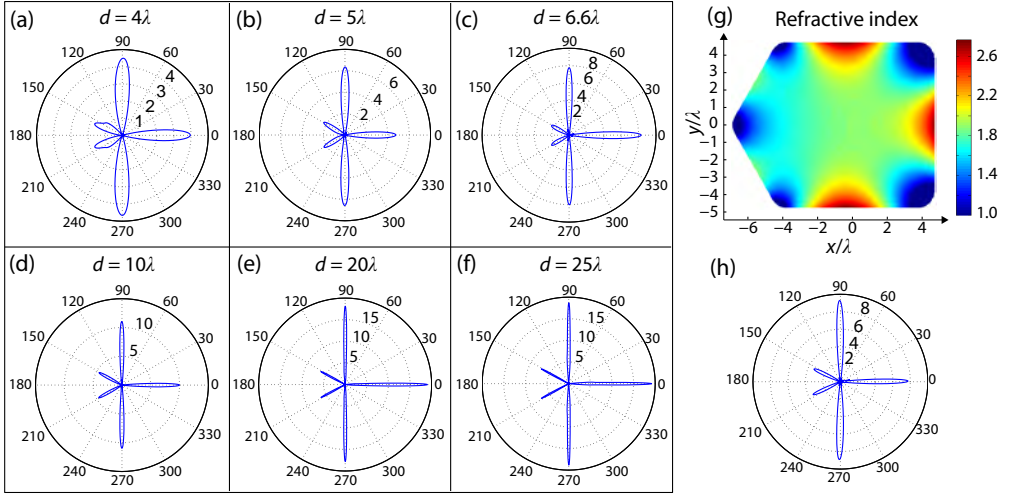
Fig. 5. (a-f) Directivity of the device in Fig. 3 at different wavelengths. (g-h) Refractive index and directivity of a modified version of the device in Fig. 3.

Regarding the practical realization of the device, the main difficulty stems from the need for refractive indices below unity. Nonetheless, there are several ways to synthesize this kind of media, depending on the wavelength of operation. At optical frequencies, it is possible to use a metal-dielectric composite that, in the effective medium regime, can be regarded as a continuous medium with an effective refractive index between those of the constitutive materials. By spatially changing the filling ratio of both constituents, the desired index profile can be achieved [21]. In addition, there exist natural media that posses a resonant permittivity at some frequencies and could be structured in a similar manner to achieve the sought index distribution. For instance, the permittivity of SiC takes values between zero and one in the midinfrared [22]. At microwaves, the desired properties can be attained by employing metamaterials made up of resonant elements exhibiting effective permittivities lower than unity [14]. In all cases, the desired properties are achieved in a narrow band, either due to the dispersive nature of the employed materials (metals, SiC) or the resonant behavior of the constituent elements. To

solve this problem, we can modify the original device so that the required refractive index is always greater than one and only dielectric materials are required for its implementation. For this purpose, we followed three steps. First, we reduced the size of the transformed circle to raise the resulting refractive index distribution (intuitively, light must travel a shorter distance in the same time, so the refractive index must be larger). Second, we multiplied the whole refractive index distribution by a constant factor F. This should not alter the device response in the ray optics approximation, although high values of F could seriously affect its properties. Finally, the refractive index was set to one in the regions where it still was below unity. These regions, as well as F, must be small enough so that the device performance is not affected. Continuing with the previous example, a modified version of the device was obtained by reducing its size by a factor of 0.7 and multiplying the resulting index distribution by 1.5. This gave rise to a refractive index distribution greater than one, except in small areas close to the corners, in which the index was set to one. The resulting profile for a device size of the order of 10λ is shown in Fig. 5(g). It ranges from 1 to 2.7 and could be implemented by milling holes with varying density or size in a dielectric medium [23]. A good directivity is achieved [Fig. 5(h)], somewhat lower than that of the original device [Fig. 5(d)]. It is worth mentioning that the unavoidable discretization of the refractive index profile sets a lower bound for the wavelength of operation, which must be large enough so that the medium is effectively continuous. Despite these limitations, a dielectric implementation should lead to a broadband device, in contrast to the approaches based on photonic crystals or plasmonic nanoantennas, which are usually narrowband due to its resonant nature.

5. Conclusions

We have shown how to engineer antenna radiation patterns in several ways with the aid of quasi-conformal mappings that result in isotropic and non-magnetic devices. As compared to previous works based on conformal transformations this technique provides us with a higher degree of control, allowing us to divide the power into highly directional beams in a set of desired directions and isotropic radiation in other angular ranges. More complex radiation patterns could be achieved by combining the presented ideas. The flexibility offered by quasi-conformal mappings enables us to avoid zero-index regions. In addition, we have analyzed the frequency dependence of the proposed devices, finding that they behave well for lateral sizes down to 5λ. Finally, we have proposed a feasible implementation that only requires isotropic dielectric media with refractive index values above unity.

References

1. A. Martínez, M.A. Piqueras, and J. Martí, "Generation of highly directional beam by k-space filtering using a metamaterial flat slab with a small negative index of refraction," Appl. Phys. Lett. **89**, 131111 (2006).

2. A. Martínez, R. García, A. Hakansson, M.A. Piqueras, and J. Sánchez-Dehesa, "Electromagnetic beaming from omnidirectional sources by inverse design," Appl. Phys. Lett. **92**, 051105 (2008).

3. J. Li, A. Salandrino, and N. Engheta, "Optical spectrometer at the nanoscale using optical Yagi-Uda nanoantennas," Phys. Rev. B **79**, 195104 (2009).

4. Y. Chen, P. Lodahl, and A. F. Koenderink, "Dynamically reconfigurable directionality of plasmon-based single photon sources," Phys. Rev. B **82**, 81402 (2010).

5. A. G. Curto, G. Volpe, T. H. Taminiau, M. P. Kreuzer, R. Quidant, and N. F. van Hulst, "Unidirectional emission of a quantum dot coupled to a nanoantenna," Science **329**, 930-933 (2010).

6. D. Dregely, R. Taubert, J. Dorfmüller, R. Vogelgesang, K. Kern, and H. Giessen, "3D optical Yagi–Uda nanoantenna array," Nat. Commun. **2**, 267 (2011).

7. U. Leonhardt and T. G. Philbin, *Geometry and Light: The Science of Invisibility* (Dover, New York, 2010).

8. F. Kong, B.-I. Wu, J.A. Kong, J. Huangfu, S. Xi, and H. Chen, "Planar focusing antenna design by using coordinate transformation technology," Appl. Phys. Lett. **91**, 253509 (2007).

9. W. X. Jiang, T. J. Cui, H. F. Ma, X. Y. Zhou and Q. Cheng, "Cylindrical-to-plane-wave conversion via embedded optical transformation," Appl. Phys. Lett. **92**, 261903 (2008).

10. Y. Luo, J. Zhang, L. Ran, H. Chen, and J.A. Kong, "Controlling the Emission of Electromagnetic Source," PIERS **4**, 795-800 (2008).

11. N. Kundtz, D.A. Roberts, J. Allen, S. Cummer, and D.R. Smith, "Optical source transformations," Opt. Express **16**, 21215-21222 (2008).

12. B.-I. Popa, J. Allen, and S.A. Cummer, "Conformal array design with transformation electromagnetics," Appl. Phys. Lett. **94**, 244102 (2009).

13. P.-H. Tichit, S.N. Burokur, and A. de Lustrac, "Ultradirective antenna via transformation optics," J. Appl. Phys. **105**, 104912 (2009).

14. P.-H. Tichit, S. Burokur, D. Germain, and A. de Lustrac, "Design and experimental demonstration of a high-directive emission with transformation optics," Phys. Rev. B **83**, 155108 (2011).

15. U. Leonhardt and T. Tyc, "Superantenna made of transformation media," New J. Phys. **10**, 115026 (2008).

16. U. Leonhardt, "Optical Conformal Mapping," Science **312**, 1777-1780 (2006).

17. J.P. Turpin, A.T. Massoud, Z.H. Jiang, P.L. Werner, and D.H. Werner, "Conformal mappings to achieve simple material parameters for transformation optics devices," Opt. Express **18**, 244-252 (2009).

18. M. Schmiele, V. S. Varma, C. Rockstuhl, and F. Lederer, "Designing optical elements from isotropic materials by using transformation optics," Phys. Rev. A **81**, 033837 (2010).

19. J. Li and J.B. Pendry, "Hiding under the carpet: A new strategy for cloaking," Phys. Rev. Lett. **101**, 203901 (2008).

20. Z. Chang, X. Zhou, J. Hu, and G. Hu, "Design method for quasi-isotropic transformation materials based on inverse Laplace's equation with sliding boundaries," Opt. Express **18**, 6089-6096 (2010)

21. J. Li, S. Han, S. Zhang, G. Bartal, and X. Zhang, "Designing the Fourier space with transformation optics," Opt. Lett. **34**, 3128-3130 (2009).

22. D. Korobkin, Y. Urzhumov, and G. Shvets, "Enhanced near-field resolution in midinfrared using metamaterials," J. Opt. Soc. Am. B **23**, 468-478 (2006).

23. J. Valentine, J. Li, T. Zentgraf, G. Bartal, and X. Zhang, "An optical cloak made of dielectrics," Nat. Mater. **8**, 568-571 (2009).

# General discussion of results and conclusions

4

Chapter

This chapter is divided into two parts corresponding to the main topics of the thesis: NIMs and transformation optics.

4.1 Negative index media

In this case, our work has been focused on obtaining low-loss NIMs in the visible spectrum. As a first step, we studied under which conditions structures exhibiting EOT could be used to build NIMs, finding a general procedure for engineering the properties of this kind of structures. This study allowed us to design a multilayer high-performance configuration of the so-called fishnet structure by exploiting a second-order magnetic resonance, in contrast to previous works, which were based on a first order resonance (both related to gap SPP Bloch modes). The proposed structure exhibits a high figure of merit in the visible spectrum, thanks to the low-loss nature of the employed magnetic resonance and the effect of the interacting adjacent layers. The structure also presents polarization independence and homogeneous properties for normal incidence. Our work concludes with two experimental demonstrations of this metamaterial. One of them constitutes the first experimental low-loss NIM in the visible regime and also the first one made up of several unit cells along the propagation direction, an important step towards bulk NIMs in this band. A comparison between the most relevant features of this work and the previous ones can be found in Figure 4.1. This work has been recognized as one of the last milestones in three-dimensional optical metamaterials by two experts in the field in a review article recently

published in Nature Photonics.[139]. It has also been featured in IEEE Spectrum[140] and presented in an invited talk in the 2012 APS March Meeting[CONF12].

Figure 4.1: Experimental NIMs in the visible. We show the maximum figure of merit achieved in existing experimental NIMs in this band. It is worth mentioning that, although in the experiment of Ref. 52 gain was incorporated to achieve extremely high figures of merit, here we only show the properties of this metamaterial without gain so that it can be compared with the other passive structures. In each case, a square indicates the maximum achieved FOM, and a color bar indicates the band where the index is negative with an arrow pointing at the wavelength at which the index reaches its minimum value, which is shown next to the arrow. The number of layers of each metamaterial is also shown. PI means polarization independent. Note that the structures we fabricated are the only ones presenting polarization independence.
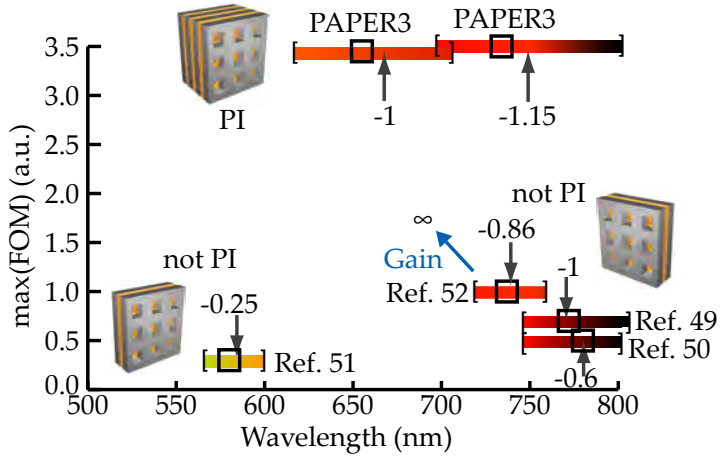
There are several lines that deserve further investigation. First, we found that the gap-SPP Bloch modes determining the permeability resonance in the proposed fishnet metamaterial display weak angular dispersion, as opposed to the highly dispersive SPP modes supported by unstructured metal-dielectric-metal multilayers or previous typical fishnet configurations. It would be interesting to determine if such a property can be exploited to achieve nearly angle-independent NIM properties in a considerable angular range, as well as to explore other routes towards isotropic NIMs in the visible regime.

In any case, it is worth mentioning that important applications of this structure arise even by exploiting only its properties at normal incidence. A remarkable example is given by a recent work that takes advantage of the unusual dispersive features of the refractive index associated to the second-order resonance of our structure (at normal incidence) to control the propagation velocity of a femtosecond laser pulse.[141] In the mentioned work, the values of the refractive index reported by us in PAPER3 are employed to show that subluminal and superluminal pulse propagation velocities can be achieved and tuned just by changing the initial chirp of a pulse propagating in a medium

with such properties. In other work, the second-order resonance is used to demonstrate subpicosecond optical switching experimentally.[142]

Moreover, we have observed that, under certain conditions, a kind of localized mode (not reported so far to our knowledge) is excited in the fishnet structure under off-angle incidence. This mode could damage the NIM behavior and should be well understood so that it can be taken into account in the design process in such a way that it does not interfere with the desired properties of the structure.

Finally, although not directly related to NIMs, we would like to better understand and improve the magnetic properties of the nanohoop structure presented in first chapter. Moreover, it is worth mentioning that the idea of optical security has been patented[PAT1] and that the development of a commercial device is within our short-term goals.

4.2   *Transformation optics*

The first part of our work in this field refers to squeezers and expanders based on transformation optics. Specifically, we have studied the reflection properties of this kind of devices, finding an analytical expression for the angle-dependent reflection coefficient of a generic three-dimensional squeezer. In contrast with previous studies, we found that there exist several conditions that guarantee no reflections and enable us to build reflectionless squeezers. Moreover, we have shown that the design of antireflective coatings for the non-reflectionless case can be reduced to matching the impedance between two dielectrics. We have illustrated the potential of these devices by proposing several applications in which a reflectionless squeezer is the key element: an ultra-short perfect coupler for high-index nanophotonic waveguides, a flat reflectionless hyperlens, a coupler for metallic waveguides with different cross-section, and a structure that is able to couple free-space light to SPPs running along non-patterned metallic surfaces with an angular bandwidth considerably higher than that of conventional couplers.

The second part of the work has been devoted to develop design methodologies that simplify the constitutive parameters required for the implementation of transformation media. On

the one hand, we have worked on the minimization of the aniso-tropy resulting from the transmutation of singularities in certain optical devices. This study gave rise to the idea of partial transmutation of singularities, with which devices without superluminal propagation can be achieved. On the other hand, we have applied the concept of quasi-conformal mapping to build realizable squeezers. In addition, we have shown how to combine conformal and quasi-conformal mappings to engineer isotropic electromagnetic devices that modify the omnidirectional radiation pattern of a point source. The flexibility offered by the proposed method allows us to achieve complex radiation patterns, which can combine high directivity in a desired number of arbitrary directions and isotropic radiation in other specified angular ranges.

As future work, we would like to extend the idea of quasi-conformal mappings to more general cases, as well as to bring some of the proposed structures to the experimental stage. Finally, we are interested in applying some of the studied concepts to the field of acoustics and in designing acoustic analogues of some of the proposed devices.

Bibliography

1. Joannopoulos, J. D. *Photonic Crystals*. Princeton University Press, (1995).

2. Pendry, J. B. *Phys. Rev. Lett.* **85**, 3966–3969 (2000).

3. *Science* **302**, 2039–2045 (2003).

4. Leonhardt, U. *Science* **312**, 1777–1780 (2006).

5. Pendry, J. B., Schurig, D., and Smith, D. R. *Science* **312**, 1780–1782 (2006).

6. Philbin, T. G., Kuklewicz, C., Robertson, S., Hill, S., König, F., and Leonhardt, U. *Science* **319**, 1367–1370 (2008).

7. Genov, D. A., Zhang, S., and Zhang, X. *Nat. Phys.* **5**, 687 (2009).

8. Genov, D. A. *Nat. Photonics* **5**, 76–78 (2011).

9. Service, R. F. and Cho, A. *Science* **330**, 1622 (2010).

10. Sihvola, A. *Metamaterials* **1**, 2–11 (2007).

11. Jackson, J. D. *Classical Electrodynamics*. Wiley & Sons, Inc., (1998).

12. Pendry, J., Holden, A., Robbins, D., and Stewart, W. *IEEE Trans. Microwave Theory Tech.* **47**, 2075–2084 (1999).

13. Zhou, J., Koschny, T., Kafesaki, M., Economou, E. N., Pendry, J. B., and Soukoulis, C. M. *Phys. Rev. Lett.* **95**, 223902 (2005).

14. Sarychev, A. K., Shvets, G., and Shalaev, V. M. *Phys. Rev. E* **73**, 36609 (2006).

15. Linden, S., Enrich, C., Dolling, G., Klein, M. W., Zhou, J., Koschny, T., Soukoulis, C. M., Burger, S., Schmidt, F., and Wegener, M. *IEEE J. Sel. Top. Quantum Electron.* **12**, 1097–1105 (2006).

16. Kriegler, C. E., Rill, M. S., Linden, S., and Wegener, M. *IEEE J. Sel. Top. Quantum Electron.* **16**, 367–375 (2010).

17. Silveirinha, M. G. *Phys. Rev. B* **75**, 115104 (2007).

18. Smith, D. R. and Pendry, J. B. *J. Opt. Soc. Am. B* **23**, 391–403 (2006).

19. Nicolson, A. M. and Ross, G. F. *IEEE Trans. Instrum. Meas.* **17**, 395 (1968).

20. Weir, W. W. *Proc. IEEE* **62**, 33 (1974).

21. Smith, D. R., Schultz, S., Markos, P., and Soukoulis, C. M. *Phys. Rev. B* **65**, 195104 (2002).

22. Chen, X., Wu, B., Kong, J. A., , and Grzegorczyk, T. M. *Phys. Rev. E* **71**, 46610 (2005).

23. Menzel, C., Rockstuhl, C., Paul, T., Lederer, F., and Pertsch, T. *Phys. Rev. B* **77**, 195328 (2008).

24. Simovski, C. R. *J. Opt.* **13**, 013001 (2010).

25. Rockstuhl, C., Paul, T., Lederer, F., Pertsch, T., Zentgraf, T., Meyrath, T. P., and Giessen, H. *Phys. Rev. B* **77**, 035126 (2008).

26. Simovski, C. *Metamaterials* **1**, 62 (2007).

27. Chen, X., Grzegorczyk, T. M., Wu, B.-I., Pacheco, J., and Kong, J. A. *Phys, Rev. E* **70**, 016608 (2004).

28. Maxwell-Garnett, J. C. *Philos. Trans. R. Soc. London, Ser. A* **203**, 385–420 (1904).

29. Pendry, J., Holden, A., Stewart, W., and Youngs, I. *Phys. Rev. Lett.* **76**, 4773–4776 (1996).

30. Rotman, W. *IRE Trans. Ant. Prop.* **10**, 82–95 (1962).

31. Johnson, P. and Christy, R. W. *Phys. Rev. B* **6**, 4370–4379 (1972).

32. Ordal, M. A., Bell, R. J., Alexander, R. W., Long, L. L., and Querry, M. R. *Applied Optics* **24**, 4493–4499 (1985).

33. Solymar, L. and Shamonina, E. *Waves in Metamaterials*. Oxford University Press, 1st edition, (2009).

34. Silveirinha, M. G. *Phys. Rev. E* **73**, 046612 (2006).

35. Silveirinha, M. G., Belov, P. A., and Simovski, C. R. *Phys. Rev. B* **75**, 035108 (2007).

36. Silveirinha, M. G. *Phys. Rev. B* **79**, 035118 (2009).

37. Silveirinha, M. G. *Phys. Rev. B (BR)* **79**, 153109 (2009).

38. Shalaev, V. M., Cai, W., Chettiar, U. K., Yuan, H.-K., Sarychev, A. K., Drachev, V. P., and Kildishev, A. V. *Opt. Lett.* **30**, 3356–3358 (2005).

39. Zhang, S., Fan, W., Malloy, K. J., Brueck, S. R. J., Panoiu, N. C., and Osgood, R. M. *Opt. Express* **13**, 4922–4930 (2005).

40. Huang, Z., Xue, J., Hou, Y., Chu, J., and Zhang, D. H. *Phys. Rev. B* **74**, 193105 (2006).

41. Zhang, S., Fan, W., Panoiu, N. C., Malloy, K. J., Osgood, R. M., and Brueck, S. R. J. *Phys. Rev. Lett.* **95**, 137404 (2005).

42. Beruete, M., Sorolla, M., and Campillo, I. *Opt. Express* **14**, 5445 (2006).

43. Alù, A., Salandrino, A., and Engheta, N. *Opt. Express* **14**, 1557–1567 (2006).

44. Alù, A. and Engheta, N. *Phys. Rev. B* **78**, 085112 (2008).

45. Simovski, C. R. and Tretyakov, S. A. *Phys. Rev. B* **79**, 045111 (2009).

46. Shalaev, V. M. *Nat. Photonics* **1**, 41–48 (2007).

47. Cai, W., Chettiar, U. K., Yuan, H.-K., de Silva, V. C., Kildishev, A. V., Drachev, V. P., and Shalaev, V. M. *Opt. Express* **15**, 3333–3341 (2007).

48. Yuan, H., Chettiar, U. K., Cai, W., Kildishev, A. V., Boltasseva, A., Drachev, V. P., and Shalaev, V. M. *Opt. Express* **15**, 1076–1083 (2007).

49. Chettiar, U. K., Kildishev, A. V., Yuan, H.-K., Cai, W., Xiao, S., Drachev, V. P., and Shalaev, V. M. *Opt. Lett.* **32**, 1671–1673 (2007).

50. Dolling, G., Wegener, M., Soukoulis, C. M., and Linden, S. *Opt. Lett.* **32**, 53–55 (2007).

51. Xiao, S., Chettiar, U. K., Kildishev, A. V., Drachev, V. P., and Shalaev, V. M. *Opt. Lett.* **34**, 3478–3480 (2009).

52. Xiao, S., Drachev, V. P., Kildishev, A. V., Ni, X., Chettiar, U. K., Yuan, H., and Shalaev, V. M. *Nature* **466**, 735–738 (2010).

53. Rockstuhl, C., Lederer, F., Etrich, C., Pertsch, T., and Scharf, T. *Phys. Rev. Lett.* **99**, 017401 (2007).

54. Zhou, J., Koschny, T., and Soukoulis, C. M. *Opt. Express* **16**, 11147–11152 (2008).

55. Burgos, S. P., de Waele, R., Polman, A., and Atwater, H. A. *Nat. Mater.* **9**, 407–412 (2010).

56. Kong, J. A. *Electromagnetic Wave Theory*. John Wiley & Sons, (1986).

57. Veselago, V. G. *Soviet Physics Uspekhi* **10**, 509 (1968).

58. Shelby, R., Smith, D. R., and Schultz, S. *Science* **296**, 77–79 (2001).

59. Parazzoli, C. G., Greegor, R. B., Li, K., Koltenbah, B. E. C., and Tanielian, M. *Phys. Rev. Lett.* **90**, 107401 (2003).

60. Caloz, C. and Itoh, T. *Electromagnetic metamaterials: transmission line theory and microwave applications*. Wiley-IEEE Press, (2005).

61. Milonni, P. W. *Fast Light, Slow Light and Left-Handed Light*. Taylor & Francis, (2004).

62. Depine, R. A. and Lakhtakia, A. *Microwave Opt. Tech. Lett.* **41**, 315–316 (2004).

63. Berman, P. R. *Phys. Rev. E* **66**, 067603 (2002).

64. Tsakmakidis, K. L., Boardman, A. D., and Hess, O. *Nature* **450**, 397 (2007).

65. Leonhardt, U. and Philbin, T. G. *New J. Phys.* **9**, 254 (2007).

66. Veselago, V. G. and Narimanov, E. E. *Nat. Mater.* **5**, 759–762 (2006).

67. Alù, A. and Engheta, N. *IEEE Trans. Microwave Theory Tech.* **52**, 199–210 (2004).

68. Parazzoli, C. G., Greegor, R. B., Nielsen, J. A., Thompson, M. A., Li, K., Vetter, A. M., and Tanielian, M. H. *App. Phys. Lett.* **84**, 3232 (2004).

69. Wiltshire, M., Pendry, J. B., Young, I. R., Larkman, D. J., Gilderdale, D. J., and Hajnal, J. V. *Science* **291**, 849–851 (2001).

70. Goodman, J. W. *Introduction to Fourier Optics*. Roberts & Company Publishers, 3rd edition, (2005).

71. Raether, H. *Surface Plasmons on Smooth and Rough Surfaces and on Gratings*. Springer, (1988).

72. Maier, S. *Plasmonics. Fundamentals and applications*. Springer, (2007).

73. Fang, N., Lee, H., Sun, C., and Zhang, X. *Science* **308**, 534–537 (2005).

74. Liu, Z., Lee, H., Xiong, Y., Sun, C., and Zhang, X. *Science* **315**, 1686 (2007).

75. Smolyaninov, I., Hung, Y.-J., and Davis, C. C. *Science* **315**, 1699–1701 (2007).

76. Barnes, W. L., Dereux, A., and Ebbesen, T. W. *Nature* **424**, 824–830 (2003).

77. Schuller, J. A., Barnard, E. S., Cai, W., Jun, Y. C., White, J. S., and Brongersma, M. L. *Nat. Mater.* **9**, 193–204 (2010).

78. Brongersma, M. L. and Shalaev, V. M. *Science* **328**, 440–441 (2010).

79. Ebbesen, T. W., Lezec, H. J., Ghaemi, H. F., Thio, T., and Wolff, P. A. *Nature* **391**, 667–669 (1998).

80. Bethe, H. *Phys. Rev.* **66**, 163–182 (1944).

81. Dolling, G., Enkrich, C., Wegener, M., Soukoulis, C. M., and Linden, S. *Opt. Lett.* **31**, 1800–1802 (2006).

82. Beruete, M., Navarro-Cía, M., and Sorolla, M. *Photonic. Nanostruct: Fundam. Appl.* (2011).

83. van Renesse, R. L. *Optical Document Security*. Artech-House 2005, 3$^{\rm rd}$ edition, (2005).

84. Unruh, W. G. *Phys. Rev. Lett.* **46**, 1351–1353 ((1981).

85. Unruh, W. G. *Phil. Trans. Roy. Soc. A* **366**, 2905–2913 (2008).

86. Horstmann, B., Reznik, B., and Fagnocchi, S. *Phys. Rev. Lett.* **104**, 250403 (2010).

87. Barceló, C., Liberati, S., and Visser, M. *Living Rev. Relativity* **8**, 12 (2005).

88. Leonhardt, U. and Philbin, T. G. *Phil. Trans. Roy. Soc. A* **366**, 2851–2857 (2008).

89. Leonhardt, U. and Philbin, T. G. *Geometry and Light: The Science of Invisibility*. Dover, (2010).

90. Greenleaf, A., Kurylev, Y., Lassas, M., and Uhlmann, G. *Phys Rev. Lett.* **99**, 183901 (2007).

91. Leonhardt, U. and Philbin, T. G. *New J. Phys.* **8**, 247 (2006).

92. Schurig, D., Pendry, J. B., and Smith, D. R. *Opt. Express* **15**, 14772–14782 (2007).

93. Leonhardt, U. *New J. Phys.* **11**, 93040 (2009).

94. Post, E. J. *Formal Structure of Electromagnetics*. Dover, (1962).

95. Bergamin, L. *Phys. Rev. A* **78**, 43825 (2008).

96. Schurig, D., Mock, J. J., Justice, B. J., Cummer, S. A., Pendry, J. B., Starr, A. F., and Smith, D. R. *Science* **314**, 977–980 (2006).

97. Cai, W., Chettiar, U. K., Kildishev, A. V., and Shalaev, V. M. *Nat. Photonics* **1**, 224–227 (2007).

98. Hu, J., Zhou, X., and Hu, G. *Opt. Express* **17**, 1308–1320 (2009).

99. LeonhardT, U. and Tyc, T. *Science* **323**, 110–112 (2009).

100. Tyc, T. and LeonhardT, U. *New J. Phys.* **10**, 115038 (2008).

101. Rahm, M., Schurig, D., Roberts, D. A., Cummer, S. A., B., D. R. S. J., and Pendry. *Photonic Nanostruct.* **6**, 87–95 (2007).

102. Belgiorno, F., Cacciatori, S. L., Clerici, M., Gorini, V., Ortenzi, G., Rizzi, L., Rubino, E., Sala, V. G., and Faccio, D. *Phys. Rev. Lett.* **105**, 203901 (2010).

103. Maxwell, J. C. *Camb. Dublin Math. J.* **8**, 188 (1854).

104. Leonhardt, U. and Philbin, T. G. *Phys. Rev. A* **81**, 011804 (2009).

105. Ma, Y., Sahebdivan, S., Ong, C. K., Tyc, T., and Leonhardt, U. *New. J. Phys.* **13**, 033016 (2011).

106. Benítez, P., Miñano, J. C., and González, J. C. *Opt. Express* **18**, 7650–7663 (2010).

107. Miñano, J. C., Benítez, P., and González, J. C. *New J. Phys.* **12**, 123023 (2010).

108. Tyc, T. and Zhang, X. *Nature* **480**, 42–43 (2011).

109. Schurig, D., Pendry, J. B., and Smith, D. R. *Opt. Express* **15**, 14772–14782 (2007).

110. Rahm, M., Cummer, S. A., Schurig, D., Pendry, J. B., and Smith, D. R. *Phys. Rev. Lett.* **100**, 063903 (2008).

111. Kwon, D.-H. and Werner, D. H. *Opt. Express* **16**, 18731–18738 (2008).

112. Yang, T., Chen, H., Luo, X., and Ma, H. *Opt. Express* **16**, 18545–18550 (2008).

113. Lai, Y., Ng, J., Chen, H., Han, D., Xiao, J., Zhang, Z.-Q., and Chan, C. T. *Phys. Rev. Lett.* **102**, 253902 (2009).

114. Shalaev, V. M. *Science* **322**, 384–386 (2008).

115. Chen, H., Chan, C. T., and Sheng, P. *Nat. Photonics* **9**, 387–396 (2010).

116. Wegener, M. and Linden, S. *Phys. Today* **63**, 32–36 (2010).

117. Ma, Y. G., Ong, C. K., Tyc, T., and Leonhardt, U. *Nat. Mater.* **8**, 639–642 (2009).

118. Perczel, J., Tyc, T., and Leonhardt, U. *New J. Phys.* **13**, 83007 (2011).

119. Yang, R., Abushagur, M. A., and Lu, Z. *Opt. Express* **16**, 20142–20148 (2008).

120. Vivien, L., Laval, S., Cassan, E., Roux, X. L., and Pascal, D. *J. Lightwave Technol.* **21**, 2429–2433 (2003).

121. Rahm, M., Roberts, D. A., Pendry, J. B., and Smith, D. R. *Opt. Express* **16**, 11555–11567 (2008).

122. Yan, W., Yan, M., and Qiu, M. *Necessary and sufficient conditions for reflectionless transformation media in an isotropic and homogenous background*. arXiv:0806.3231v1, (2008).

123. Grzegorczyk, T. M., Chen, X., Pacheco, J., Chen, J., Wu, B. I., and Kong, J. A. *Prog. Electromagn. Res.* **51**, 83–113 (2005).

124. Hecht, E. *Optics*. Addison Wesley, 4th edition, (2001).

125. Taillaert, D., Bogaerts, W., Bienstman, P., Krauss, T. F., Daele, P. V., Moerman, I., Verstuyft, S., Mesel, K. D., and Baets, R. *IEEE J. Quantum Electron.* **38**, 949–955 (2002).

126. Roelkens, G., Vermeulen, D., Thourhout, D. V., Baets, R., Brision, S., Lyan, P., Gautier, P., and Fedeli, J. M. *Appl. Phys. Lett.* **92**, 131101 (2008).

127. T. Tsuchizawa, K. Yamada, H. F. T. W. J. T. M. T. T. S. E. T. S. I. and Morita, H. *IEEE J. Sel. Top. Quantum Electron.* **11**, 232–240 (2005).

128. Vasic, B., Isic, G., Gajic, R., and Hingerl, K. *Phys. Rev. B* **79**, 85103 (2009).

129. Xiong, Y., Liu, Z., and Zhang, X. *App. Phys. Lett* **94**, 203108 (2009).

130. Kildishev, A. V. and Narimanov, E. E. *Opt. Lett.* **32**, 3432 (2007).

131. Gaillot, D. P., Croënne, C., Zhang, F., and Lippens, D. *New J. Phys.* **10**, 115039 (2008).

132. Tichit, P., Burokur, S. N., and Lustrac, A. *Opt. Express* **18**, 767 (2009).

133. Zang, X. and Jiang, C. *Opt. Express* **18**, 10168 (2010).

134. Ren, C., Xiang, Z., and Cen, Z. *Appl. Phys. Lett.* **97**, 044101 (2010).

135. Thompson, J. F., Sdoni, B. K., and Weatherill, N. P. *Handbook of grid generation*. CRC Press, (1999).

136. Li, J. and Pendry, J. B. *Phys. Rev. Lett.* **101**, 203901 (2008).

137. Chang, Z., Zhou, X., Hu, J., and Hu, G. *Opt. Express* **18**, 6096 (2010).

138. Landy, N. I. and Padilla, W. J. *Opt. Express* **17**, 14872–14879 (2009).

139. Soukoulis, C. M. and Wegener, M. *Nat. Photonics* **5**, 523 (2011).

140. Krieger, K. *Metamaterials step into the light. IEEE Spectrum* (April 2012).

141. Fedorov, V. Y. and Nakajima, T. *Phys. Rev. Lett.* **107**, 143903 (2011).

142. Dani, K. M., Ku, Z., Upadhya, P. C., Prasankumar, R. P., Brueck, S. R. J., and Taylor, A. J. *Nano Lett.* **9**, 3565–3569 (2009).

Peer-reviewed publications

Main contributions

[PAPER1] C. García-Meca, R. Ortuño, F. J. Rodríguez-Fortuño, J. Martí, and A. Martínez. Negative refraction index metamaterials aided by extraordinary optical transmission. *Opt. Express*, 17:6026–6031, 2009.

[PAPER2] C. García-Meca, R. Ortuño, F. J. Rodríguez-Fortuño, J. Martí, and A. Martínez. Double-negative polarization-independent fishnet metamaterial in the visible spectrum. *Opt. Lett.*, 34:1603–1605, 2009.

[PAPER3] C. García-Meca, J. Hurtado, J. Martí, A. Martínez, W. Dickson, and A. V. Zayats. Low-loss multilayered metamaterial exhibiting a negative index of refraction at visible wavelengths. *Phys. Rev. Lett.*, 106:067402, 2011.

[PAPER4] M. Navarro-Cía, C. García-Meca, M. Beruete, A. Martínez, and M. Sorolla. Dual-band double-negative-index fishnet metamaterial at millimeter-waves. *Opt. Lett.*, 36:4245–4247, 2011.

[PAPER5] C. García-Meca, R. Ortuño, R. Salvador, A. Martínez, and J. Martí. Low-loss single-layer metamaterial with negative index of refraction at visible wavelengths. *Opt. Express*, 15:9320–9325, 2007.

[PAPER6] A. Martínez, C. García-Meca, R. Ortuño, F. J. Rodríguez-Fortuño, and J. Martí. Metamaterials for optical security. *App. Phys. Lett.*, 94:251106–251108, 2009.

[PAPER7] J. Perczel, C. García-Meca, and U. Leonhardt. Partial transmutation of singularities in optical instruments. *J. Opt.*, 13:075103, 2011.

[PAPER8] C. García-Meca, M. M. Tung, J. V. Galán, R. Ortuño, F. J. Rodríguez-Fortuño, J. Martí, and A. Martínez. Squeezing and expanding light without reflections via transformation optics. *Opt. Express*, 19:3562–3575, 2011.

[PAPER9] C. García-Meca, R. Ortuño, J. Martí, and A. Martínez. Exciting surface plasmons with transformation media. *Plasmonics (accepted)*, 2012.

[PAPER10] C. García-Meca, A. Martínez, and U. Leonhardt. Engineering antenna radiation patterns via quasi-conformal mappings. *Opt. Express*, 19:23743–23750, 2011.

Other contributions

[PAPERb1] R. Salvador, A. Martínez, C. García-Meca, R. Ortuño, and J. Martí. Analysis of hybrid dielectric-plasmonic waveguides. *J. Sel. Topics Quant. Electr.*, 14:1496–1501, 2008.

[PAPERb2] R. Ortuño, C. García-Meca, F. J. Rodríguez-Fortuño, J. Martí, and A. Martínez. Role of surface plasmon polaritons on optical transmission through double layer metallic hole arrays. *Phys. Rev. B*, 79:75425, 2009.

[PAPERb3] R. Ortuño, C. García-Meca, F. J. Rodríguez-Fortuño, A. Hakansson, A. Griol, J. Hurtado, J. A. Ayúcar, L. Bellieres, P. J. Rodríguez, F. López-Royo, J. Martí, and A. Martínez. Midinfrared filters based on extraordinary optical transmission through subwavelength structured gold films. *J. App. Opt.*, 106:124313, 2009.

[PAPERb4] F. J. Rodríguez-Fortuño, C. García-Meca, R. Ortuño, J. Martí, and A. Martínez. Coaxial plasmonic waveguide array as a negative-index metamaterial. *Opt. Lett.*, 34:3325–3327, 2009.

[PAPERb5] F. J. Rodríguez-Fortuño, C. García-Meca, R. Ortuño, A. Martínez, and J. Martí. Modeling high-order plasmon resonances of a u-shaped nanowire used to build a negative-index metamaterial. *Phys. Rev. B*, 79:75103, 2009.

[PAPERb6] R. Ortuño, C. García-Meca, F. J. Rodríguez-Fortuño, and A. Martínez. Enlarging the negative-index bandwidth of optical metamaterials by hybridized plasmon resonances. *Opt. Lett.*, 35:4205–4207, 2010.

[PAPERb7] F. J. Rodríguez-Fortuño, C. García-Meca, R. Ortuño, J. Martí, and A. Martínez. Zero-bandwidth mode in a split-ring-resonator-loaded one-dimensional photonic crystal. *Phys. Rev. B*, 81: 233101, 2010.

[PAPERb8] R. Ortuño, C. García-Meca, F. J. Rodríguez-Fortuño, J. Martí, and A. Martínez. Multiple extraordinary optical transmission peaks from evanescent coupling in perforated metal plates surrounded by dielectrics. *Opt. Express*, 18:7893–7898, 2010.

[PAPERb9] C. García-Meca and M. M. Tung. The variational principle in transformation optics engineering and some applications. *Mathematical and computer modelling*, 2011.

Conferences

Main contributions

[CONF1] C. García-Meca, R. Ortuño, R. Salvador, A. Martínez, and J. Martí. Low-loss single-layer metamaterial with negative index of refraction at visible frequencies. In *Metamaterials' 2007. 1st International Congress on Advanced Electromagnetic Materials in Microwave and Optics*, Rome, Italy.

[CONF2] C. García-Meca, R. Ortuño, F. J. Rodríguez-Fortuño, J. Martí, and A. Martínez.   Extraordinary optical transmission with negative index of refraction.   In *Metamaterials' 2008. 2nd International Congress on Advanced Electromagnetic Materials in Microwave and Optics*, Pamplona, Spain.

[CONF3] A. Martínez, C. García-Meca, R. Ortuño, and J. Martí. Photonic negative-index metamaterials. In *Conferencia Española de Nanofotónica 2008*, Tarragona, Spain.

[CONF4] C. García-Meca, R. Ortuño, F. J. Rodríguez-Fortuño, J. Martí, and A. Martínez.   Double-negative polarization-independent fishnet metamaterial operating in the visible spectrum. In *IEEE LEOS Winter Topicals 2009*, Innsbruck, Austria.

[CONF5] C. García-Meca, R. Ortuño, F. J. Rodríguez-Fortuño, J. Martí, and A. Martínez. Strong magnetism at visible wavelengths via coupled silver nanohoops. In *Metamaterials' 2009. 3rd International Congress on Advanced Electromagnetic Materials in Microwaves and Optics*, London, UK.

[CONF6] C. García-Meca, M. M. Tung, J.V. Galán, R. Ortuño, F. J. Rodríguez-Fortuño, J. Martí, and A. Martínez. Light compression without reflections. In *SPIE Photonics Europe 2010*, Brussels, Belgium.

[CONF7] C. García-Meca, J. Hurtado, W. Dickson, A.V. Zayats, and A. Martínez. Low-loss two-functional-layer negative-index metamaterial operating in the visible spectrum utilising 2nd order magnetic resonance. In *Metamaterials' 2010. 4th International Congress on Advanced Electromagnetic Materials in Microwaves and Optics*, Karlsruhe, Germany.

[CONF8] C. García-Meca, R. Ortuño, F. J. Rodríguez-Fortuño, J. Martí, and A. Martínez. Flat and reflectionless solid immersion lens based on transformation optics. In *YSMM' 2011. 4th young scientist meeting on metamaterials*, Valencia, Spain.

[CONF9] C. García-Meca; M. Navarro-Cía; M. Beruete; A. Martínez; M. Sorolla. Experimental polarization-independent dual-band metamaterial with a negative refractive index in the millimetre range. In *5th International congress on advanced electromagnetic materials in microwaves and optics - Metamaterials' 2011*, Barcelona, Spain.

[CONF10] C. García-Meca, A. Martínez, and U. Leonhardt. Engineering antenna radiation patterns via quasi-conformal transformations. In *5th International congress on advanced electromagnetic materials in microwaves and optics - Metamaterials' 2011*, Barcelona, Spain.

[CONF11] C. García-Meca, R. Ortuño, F. J. Rodríguez-Fortuño, J. Martí, and A. Martínez. Scaling slabs based on transformation optics for immersion lenses and angular filters. In *5th International congress on advanced electromagnetic materials in microwaves and optics - Metamaterials' 2011*, Barcelona, Spain.

[CONF12] C. García-Meca. Low-loss multilayered metamaterial exhibiting a negative index of refraction at visible wavelengths. In *APS March Meeting 2012*, Boston, USA (INVITED).

Other contributions

[CONFb1] R. Ortuño, C. García-Meca, F. J. Rodríguez-Fortuño, J. Martí, and A. Martínez. Effect of internal and external surface plasmons in the enhanced transmission through double-layer metallic hole arrays. In *Metamaterials' 2008. 2nd International Congress on Advanced Electromagnetic Materials in Microwave and Optics*, Pamplona, Spain.

[CONFb2] F. J. Rodríguez-Fortuño, C. García-Meca, R. Ortuño, J. Martí, and A. Martínez. Negative index metamaterial through high-order plasmon res-

onances on u-shaped nanowires. In *IEEE LEOS Winter Topicals 2009*, Innsbruck, Austria.

[CONFb3] R. Ortuño, C. García-Meca, F. J. Rodríguez-Fortuño, J. Martí, and A. Martínez. Multiple optical extraordinary transmission peaks from evanescent coupling in perforated metal plates surrounded by dielectric. In *Metamaterials' 2009. 3rd International Congress on Advanced Electromagnetic Materials in Microwaves and Optics*, London, UK.

[CONFb4] R. Ortuño, C. García-Meca, F. J. Rodríguez-Fortuño, J. Martí, and A. Martínez. Mir filters based on extraordinary optical transmission through nanostructures gold films. In *Metamaterials' 2009. 3rd International Congress on Advanced Electromagnetic Materials in Microwaves and Optics*, London, UK.

[CONFb5] F. J. Rodríguez-Fortuño, R. Ortuño, C. García-Meca, J. Martí, and A. Martínez. Split-ring resonators achieve transmission trough a photonic crystal bandgap. In *Metamaterials' 2009. 3rd International Congress on Advanced Electromagnetic Materials in Microwaves and Optics*, London, UK.

[CONFb6] R. Ortuño, C. García-Meca, F. J. Rodríguez-Fortuño, J. Martí, and A. Martínez. Enlarged negative effective index bandwidth from fishnet metamaterials. In *SPIE Photonics Europe 2010*, Brussels, Belgium.

[CONFb7] F. J. Rodríguez-Fortuño, B. Tomás-Navarro, C. García-Meca, R. Ortuño, and A. Martínez. Split-ring-resonators inserted in a photonic crystal achieve a zero bandwidth passband. In *Metamaterials' 2010. 4th International Congress on Advanced Electromagnetic Materials in Microwaves and Optics*, Karlsruhe, Germany.

[CONFb8] B. Tomás-Navarro, F. J. Rodríguez-Fortuño, R. Ortuño, C. García-Meca, and A. Martínez. Zero bandwidth mode on a split ring resonator loaded

waveguide at cutoff. In *Conferencia Española de Nanofotónica 2010*, Segovia, Spain.

[CONFb9] R. Ortuño, C. García-Meca, F. J. Rodríguez-Fortuño, J. Martí, and A. Martínez. Extraordinary transmission through metamaterials arrays at thz frequencies. In *YSMM' 2011. 4th young scientist meeting on metamaterials*, Valencia, Spain.

[CONFb10] M. Lorente-Crespo, F. J. Rodríguez-Fortuño, R. Ortuño, C. García-Meca, and A. Martínez. Magnetic metamaterials in the visible range based on nano-hoops and nano-squares. In *YSMM' 2011. 4th young scientist meeting on metamaterials*, Valencia, Spain.

[CONFb11] R. Ortuño, C. García-Meca, F. J. Rodríguez-Fortuño, and A. Martínez. Extraordinary transmission and light confinement in subwavelength metallic films apertures. In *29th progress in electromagnetics research symposium - PIERS 2011*, Marrakesh, Morocco.

[CONFb12] C. García-Meca, A. Martínez, and M. M. Tung. The variational principle in transformation optics engineering and some applications. In *Mathematical Modelling in Engineering & Human Behaviour 2011*, Valencia, Spain.

[CONFb13] M. Navarro-Cía, C. García-Meca, P. Rodríguez-Ulibarri, M. Beruete, A. Martínez, and M. Sorolla. Engineering the diffraction orders of the fishnet metamaterial for subterahertz dual-band backward wave propagation. In *META 2012*, Paris, France.

[CONFb14] M. Lorente-Crespo, R. Ortuño, C. García-Meca, and A. Martínez. Strong magnetic enhancement in the visible range by Al nano-hoops. In *META 2012*, Paris, France.

[CONFb15] M. Lorente-Crespo, R. Ortuño, I. Alepuz-Benaches, C. García-Meca, L. Wang, Y. Ekinci,

P. Scherrer, and A. Martínez. Strong magnetism by closely spaced gold nanohoops. In *SPIE Photonics Europe 2012*, Brussels, Belgium.

[CONFb16] I. Alepuz-Benaches, C. García-Meca, F. J. Rodríguez-Fortuño, R. Ortuño, M. Lorente-Crespo, A. Griol, J. Martí, and A. Martínez. Strong magnetic resonance of coupled aluminum nanodisks on top of a silicon waveguide. In *SPIE Photonics Europe 2012*, Brussels, Belgium.

Patents

[PAT1] A. Martínez, C. García Meca, and J. Martí. *Optical security mark for object, generates magnetic response to incident radiation having wavelength corresponding to specific code formula.* WO2010109036-A1.